Characterisation of the *trans*-influence, and its inverse

Thomas R. Freeman

This dissertation is submitted for the degree of MSc by Research

February 2020

Faculty of Science and Technology

If you think you understand quantum mechanics, you don't understand quantum mechanics.

Richard Feynman

Declaration

This thesis has not been submitted in support of an application for another degree at this or any other university. It is the result of my own work and includes nothing that is the outcome of work done in collaboration except where specifically indicated. Many of the ideas in this thesis were the product of discussion with my supervisors, Dr Andrew Kerridge, and Dr Michael Peach. The total word count of this thesis including the abstract (but excluding references) is 32428 words.

Abstract

The *trans*-influence (TI), whereby the bond directly opposite a strong σ-donor, in certain d-block complexes, is relatively **lengthened**. The inverse *trans*-influence (ITI), whereby the analogous bond in certain f-block complexes, is relatively **shortened**. The purpose of this work is investigate the origin of the TI and its inverse (ITI) in a variety of d- and f-block species of the $[MOX_5]^-$ form (M = U, Mo, W, and halide X = F, Cl, Br). Relative magnitudes of the influences as both a function of the metal species and halide ligand are determined computationally. Several model chemistries are tested, spanning eight basis sets and seven DFT exchange–correlation functionals. Characterisation of the complexes in the ground state considers bond length, QTAIM, and natural bond orbital (NBO) analyses. The results demonstrate that the d-block TIs have generally higher magnitudes than the f-block ITIs, and that regardless of metal centre, the magnitudes of the influences are greatest in the F-ligand complexes, and lowest in the Br-ligand complexes. NBO analysis identifies that the *trans*-bonds, relative to the *cis*-bonds in the ITI-exhibiting $[UOX_5]^-$ species, exhibit reduced f- and s-orbital, and enhanced d-orbital character from the U contributions. A novel examination of the influence of electronic excitation (as studied using TDDFT) on the TI and ITI is considered. The geometries of the ground and of pertinent excited states are compared to identify key excitations that significantly alter the influences. Analysis of three excitations proved particularly insightful; two exclusive to the f-block species, and one common to both the d- and f-block species. For the latter excitations yielded a reduction of the TI in the d-block and a reduction (and reversal) of the ITI in the f-block species. The results hint at a possible common electronic origin for the TI and ITI and demonstrate that these influences can be moderated by electronic excitation.

Acknowledgments

There are undoubtfully a long list of people of which I owe my gratitude for their contributions to this project, supervisors, family, friends, co-workers, the driver of the 1A bus, you have all helped in ways you may never understand.

To my supervisors Michael and Andy, for their innumerable contributions. Michael, your tips on layout and presentation were so welcomed, in fact I often felt your knowledge in this area *almost* outweighed your skills in computational chemistry. Andy, despite being on paternity leave and having perhaps the busiest few of months of your life, you still took the time to explain QTAIM to me for the innumerable time, all with a smile on your face, I thank you for that. To Sapphire, for your guidance and patience, it couldn't have been easy mentoring someone who decisively never checks his emails.

To my parents, you have always supported my education over my financial stability, thank you truly for that and for not telling me to get a job, only thinking it. I hope one day to make you as proud of me as I am of you. To my sister Rebecca, for recommending Lancaster University to me in the first place having previously studied there, I guess I just wanted to see if it was something that *they* had taught you that makes you so exceptional, it wasn't. To my brother Will, for just being you. You embody the best of a generation, and you're fearless enough to do what I never could: carve your own path in life; wherever you end up, you will have my full support always. To my friend Lici, not even the 10,000 miles you flew to Australia stopped you from being a part of my daily life, I'm afraid I'll have no new stories from my time in Lancaster, but I look forward to sharing some from the next chapter.

Finally, to my partner Melanie, I can't say too much here without it sounding like a will reading… Perhaps I can summarise it like this: my life is significantly enhanced when you are around. You pick me up when I am down but are careful to reel me in when my ego flies too high. Thank you for your help in this thesis and in life, the latter of which I can't wait to spend with you.

CONTENTS

Chapter 1

Introduction to the *trans*-influence and its inverse

1.1 The *trans-i*nfluences and its inverse

The ***trans*-influence (TI),** is a ground-state structural deformation that manifests in certain **d-block** square planar, or *pseudo*-octahedral complexes. It is characterised by the bond directly opposite (*trans-*) to a strong σ-donating ligand, being **lengthened** relative to the remaining *cis*-bonds[1] (this is illustratively shown in **figures 1.1a** for the octahedral geometry). A σ-donating ligand in this case, is a species that donates electrons very efficiently to a metal species, forming a strong single bond resultantly. The *trans*-influence is a strictly thermodynamic process, not to be confused (although the two are similar) with the kinetic *trans*-effect,[2] a distinction that we revisit. Note that some authors use different nomenclature to describe the *trans*-influence including terms such as the 'structural *trans*-effect' or the 'thermodynamic *trans*-effect.'[1] The majority of research on the *trans*-influence pertains to complexes with square planar geometries, a recent review attempts to compile research pertaining to the *pseudo*-octahedral geometrires;[1] it is this geometry that will be focused on in this project.

The **inverse *trans*-influence (ITI),** much as its name suggests, is the opposite of the *trans*-influence, where the bond that is directly opposite (*trans-*) to a strong σ-donating ligand, this time, appears **shortened**, relative to the remaining *cis*-bonds[3] (this is illustratively shown in **figure 1.1b** for the octahedral geometry). This influence often occurs in high oxidation state **f-block** complexes,[4–6] and has been demonstrated in several geometries including octahedral,[7,8] trigonal bipyramidal,[9] and linear (in the case of the uranyl UO_2^{2+} molecule[10]). The octahedral geometry will be the focus of this project. Previous characterisation of the ITI has been performed both experimentally[7,11] and theoretically using density functional methods;[6,8] the latter is implemented in this project.
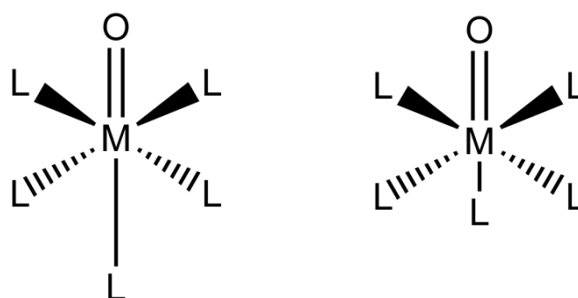
Figures 1.1a + 1.1b. Illustrations of the *trans*-influence (**1.1a**, LHS) and the inverse *trans*-influence (**1.1b**, RHS) for the *pseudo*-octahedral geometry, where M = a d-block cation for the *trans*-influence, and an f-block cation for the inverse *trans*-influence.

Extending beyond the relative shortening/lengthening of the *trans*-bonds, the influences have been shown in certain instances to play a more structurally-defining role. For example, the ITI has been proposed to explain why certain f-block dioxo-cations of the MO_2^{2+} moiety (M = U, Np, Pu) readily prefer a linear O-M-O arrangement,[5] and when assuming this arrangement, the M-O bonds are typically shorter, and more robust than expected.[10] On the other hand, the corresponding d-block dioxo-cations, MO_2^{2+} tend to typically prefer a bent *cis*-MO_2^{2+} arrangement.[12] Gregson *et al* [5] provide an illustrative example (**figure 1.2**) of how this trend can be applied to the octahedral geometries.
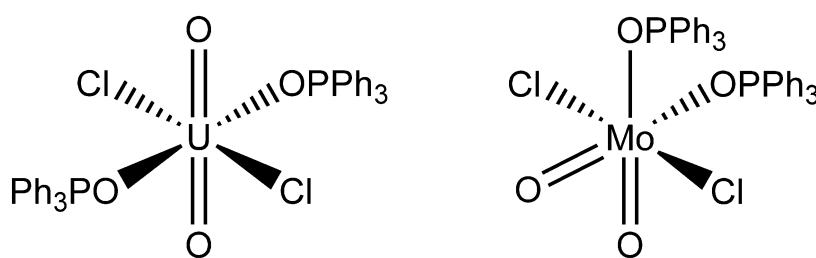
Figure 1.2. Comparing structures $UO_2Cl_2(OPPh_3)_2$ (left) and $MoO_2Cl_2(OPPh_3)_2$ (right). $UO_2Cl_2(OPPh_3)_2$ adopts a linear O-U-O moiety due to the directing effects of the ITI in the UO_2^{2+} moiety. Alternatively, like most other d-bock complexes of this type, $MoO_2Cl_2(OPPh_3)_2$ adopts a bent *cis*-favoured O-U-O geometry on account of the TI. Data were obtained through simulations carried out by Gregson *et al*[5]

The origins of the TI and ITI are generally regarded to be a consequence of the strong σ-donor polarising the core of the central metal species.[7] Denning,[7] prescribes a 'polarisation model' that elucidates this effect, where the polarisation manifests in two ways: dipolar, characterised by charge build-up in the *trans*-bonds (causing a repulsion of the *trans*-ligands, distinctive of the TI), and quadrupolar, characterised by charge build-up in the *cis*-positions (causing a analogous repulsion in the *cis*-bonds, characteristic of the ITI). Denning[7] reasons that these polarisation effects are a result of the different orbital arrangements in the metal species; that typically (although not exclusively, as is the case for thorium, Th[7,13]) can be characterised by existing in the f-block (quadrupolar, ITI) or a d-block (dipolar, TI) groups in the periodic table.

We provide further details of this polarisation model in **section 1.3.4**. Considering the strong σ-donors, Glenwright and Coe[1] detail some of the different types that have been shown to contribute to the TI in d-block species, including oxides, nitrides, sulphides, hydrides, and imido ligands. There are less accounts of the relatively new ITI, compared to the TI, but of the research, strong σ-donors include oxides,[8] imido ligands,[14] and carbenes.[3]

1.2 Overview of the Project

For this project, complexes of the type MOX_5 (M = U, Mo, W and X = F, Cl, Br as illustrated in **figure 1.3**) are simulated using Density Functional Theory (DFT). All of the structures present a *pseudo*-octahedral geometry with C_{4v} symmetry, a metal atom of a formally 6+ oxidation state and no unpaired electrons. In **figure 1.3**, the d-block complexes **IV** – **IX** (rows 2 and 3) exhibit the *trans*-influence, and the f-block complexes **I** – **III** (row 1) exhibit the inverse *trans*-influence. This project is effectively divided into two sections: characterisation of the ITI and TI at the **ground** state, and characterisation of the TI and ITI in **excited** states in UV-vis regions.

The main aims of the **ground state** analysis are to provide elucidation of the structural and energetic magnitudes of the TI and ITI as a function of both the central metal cation, and the coordinating ligand species; furthermore, to assess the similarities and differences between the TI and ITI. Using DFT methods, the ground state analysis proceeds through three main analyses: bond length, topological, and bond-orbital, the latter two are mostly concerned with bond covalency. Additionally, via bond length analysis, the limiting points of the TI and ITI will be explored by varying the length of the strong σ-donor bond (the O-species) to assess how this affects the ITI/TI.

Comparison of the TI and ITI can be achieved simply by taking the ratio of the *trans*- and *cis*-bond distances to give an 'influence magnitude.' This way only the *relative* influence magnitude for a system is shown- irrespective of whether it is ITI- or TI-exhibiting. **Equation 1** gives details of this, where 'I' represents the influence magnitudes, and 'D' represents the distance in picometres pm between the central cation M and the *cis*-ligands L (*cis*), or the central cation and the *trans*-ligands L (*trans*).

$$I = \frac{D_{\text{M-L } (trans)}}{D_{\text{M-L } (cis)}} \tag{1}$$

If the value of the influence magnitude is below 1, it is a result of the *cis*-bond lengths being greater than the *trans*-bond length, characteristic of the inverse *trans*-influence (the **lower** the deviation from 1, the more prominent the influence is). If the influence is **greater** than 1, it is a result of the *trans*-bond length being greater than the *cis*-bond lengths, characteristic of the *trans*-influence (the **higher** the deviation from 1, the more prominent the influence).
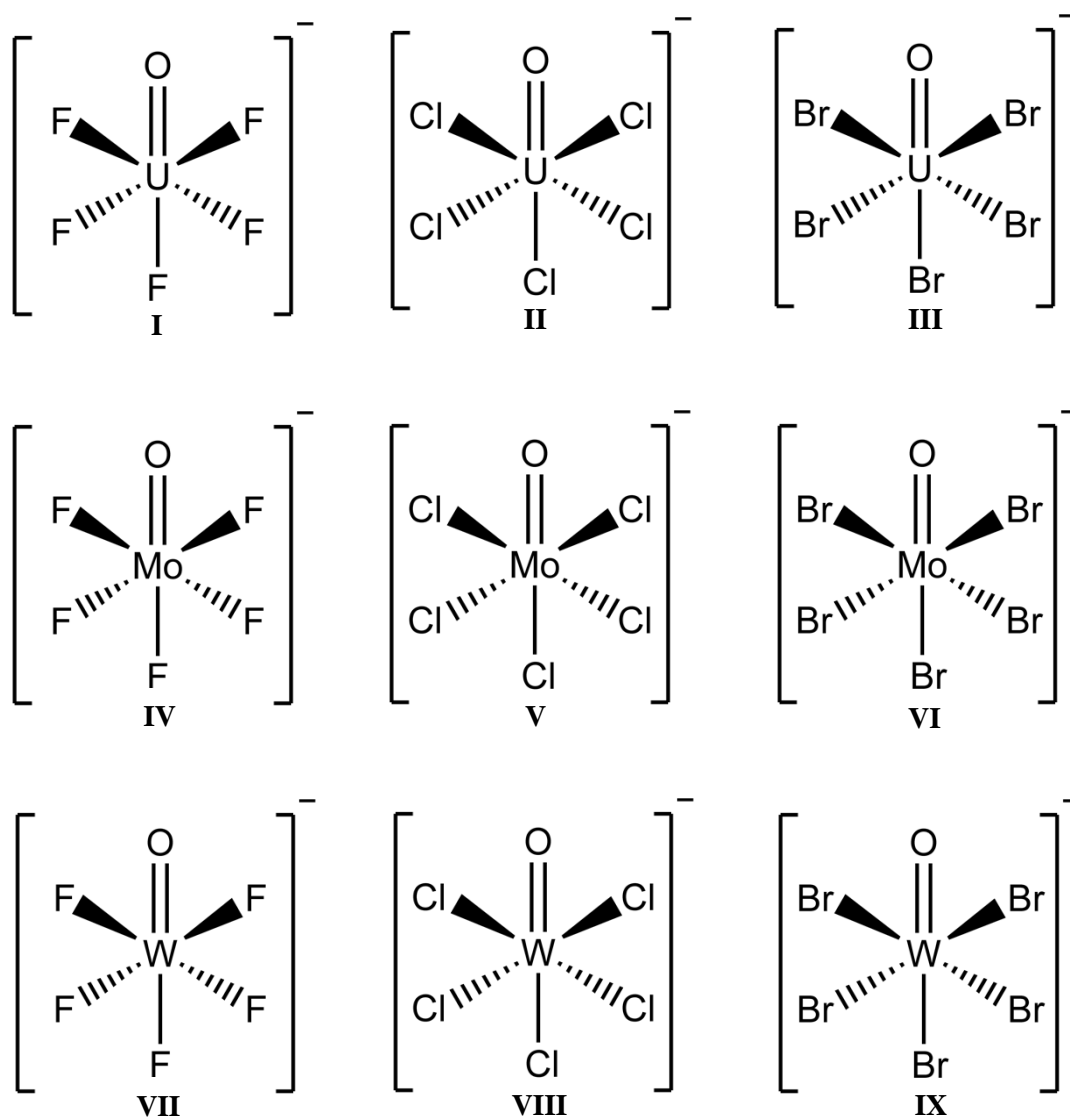
Figure 1.3. Molecules **I** – **III** (top row) all exhibit the ITI, as illustrated by their slightly **shorter** U-X$_{trans}$ bonds relative to the U-X$_{cis}$ bonds. Molecules **IV** – **IX** (bottom two rows) all exhibit the TI, as illustrated by their slightly **longer** M-X$_{trans}$ bonds relative to the M-X$_{cis}$ Bonds. All molecules are modelled using DFT methods, of which the details and model chemistries are presented in **section 2.2**. These complexes were selected due to previous work from Denning[7] and Kaltsoyannis[8] *et al.*

The **excited state** analysis involves identifying occupied molecular orbitals in both the TI and ITI-exhibiting species, that upon excitation, could affect the influences in a characteristic way. Using time-dependant DFT (TD-DFT), we simulate the UV-Vis absorption spectra, identifying excitations that involve transitions pertaining to these molecular orbitals. From here, the structural impact and relevance to the ITI and TI of certain electronic excitations is assessed by geometrically optimising these excited states, then assessing if and how the ITI/TI is affected. The most ideal example is identifying molecular orbital transitions that either remove or reverse the influences.

Prior to both sections, a full methodology is detailed, showing how basis sets, functionals and other simulation factors were chosen (i.e. the model chemistry); discussions for their suitability in the project are provided. In total, eight different basis sets were compared for the main group O, F, Cl, and Br species in **molecules I – IX**, as well as seven different DFT functionals.

1.3 The *trans*-Influence in Detail

As mentioned, the *trans*-influence is a thermodynamic process, it is subtly different to another process called the kinetic *trans*-**effect** (KE), of which it is it is the main contributor; the other contributors being steric effects involving the *cis*-ligands' π-acceptor capabilities.[2,15] The *trans*-influence lengthens the bonds that are *trans*- to a strong sigma donor, the kinetic *trans*-effect (KTE) is a utilisation of this bond lengthening (and further labilization), and results in in the selective **substitution** of this *trans*-ligand, via a kinetic intermediate. As such, the KTE is a thorough and robust method for fine-tuning d-block complexes in various platforms in industry; the fact that the *trans*-influence is a main contributor to the KE immediately provides incentives for its study.

1.3.1 Identification of the *trans*-influence

Various modern spectroscopy methods have been shown to effectively characterise the TI with ease. Techniques include NMR, IR and various diffractive methods such as x-ray crystallography.[1,16] These methods do, however, all have drawbacks to some degree. X-ray diffraction, a more popular quantitative analysis of crystal systems has been used on a multitude of examples.[17–19] Kapoor *et al* however argue that packing and conformational effects within a crystal may influence the metal-ligand bonding.[17] In the case of NMR, sure we can expect two different bond peaks to show up in systems exhibiting the TI, which certainly identifies the occurrence of the TI but does not provide much in terms of qualitative data. Additionally, NMR comes with the stipulation that both the metal and ligand must be 'NMR active.' Ligand species such as the NMR-active phosphorus would be a good option albeit a great limiter in terms of variability. IR is considered a cheap and efficient method of probing the complexes characteristic bond frequencies, but the complexity of certain M-X vibrational modes again limits the variety of ligands this technique is effective for.[20,21]

1.3.2 Origins of the *trans*-influence

The discovery of the *trans*-influence was predated by the kinetic *trans*-effect (KE) due to the relatively easier identification of the latter, simply it was simpler to observe the directed *substitution* of certain of ligands (the KE), rather than observing different bond lengths (the TI). The first suggestion of ligands being able to direct substitution reactions was made by Werner[22] in late 1893 with his coordination theory. In the same year, Kurnakov,[23] whilst investigating the substitution of ligands by thiourea and thioacetamide in square planar complexes, of the variety $M(NH_3)X_2$ (M = Pt, Pd; X = acid radical or halogen), found that in the *cis*-structures, total ligand substitution with thiourea or thioacetamide occurred whereas in the *trans*-structures, only partial substitution of the acid radicals or halide occurred (as detailed in **figure 1.4**). This provided the basis for Chernyaev's major discovery some 33 years later.[23] Chernyaev, was an inorganic chemist who dealt mostly with square planar Pt(II) complexes. For differing ligands (nitro, aquo and hydroxylamine); he observed the differing dissociation rates of certain ligands that were *trans*- to each other. Furthermore, he suggested from his experimental work, that anions are the strongest *trans*-labilising ligands.[1,23]
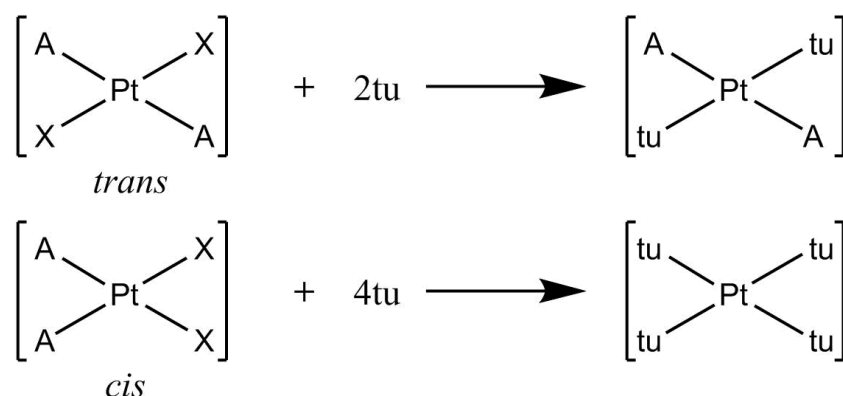
Figure 1.4. Equations detailing the kinetic *trans*-effect. The top equation shows the total substitution of ligands in a *cis*-square planar complex where 'tu' is either thiourea or thioacetamide, 'A' is the strong sigma donor (either N or O in this case), and X is an acid radical or halogen. The bottom equation shows how the anionic substituents (A) stabilise each other in the *trans*-formation, resulting in only partial substitution by tu.

The first attempt at rationalising the *trans*-effect was carried out by the Russian chemist Grinberg.[24] Grinberg[24] suggested that the polarisation from a strong σ-donor would result in a build-up of negative charge on the metal centre of a complex, in turn repelling the ligand *trans*- to the σ-donor.[1,24,25] In 1966, Pidock *et al*,[27] using ^{195}Pt-^{31}P NMR, identified the ground-state deformation of bond lengths (in square planar geometries) that contributed to the kinetic *trans*-effect prior to being substituted, the first indication of the *trans*-influence.[18,27] Mason and Towl[28] then considered the overall *trans*-influences in octahedral geometries.

The *pseudo*-octahedral TI-exhibiting structures took slightly longer to elucidate due to the complex nature of higher coordinated d-block metal species;[1] Coe and Glenwright[1] give an excellent overview of the *trans*-influence (and effect) in this geometry. To give a quantitative impression of the TI, using **equation 1**, influence magnitudes were calculated for several *pseudo*-octahedral d-block crystal complexes obtained from the literature,[1] this is shown in **table 1.1**.

Table 1.1. Crystallographic data for several octahedral d-block complexes exhibiting the TI with the MAnX$_5$ structure. Where 'An' is the strong sigma donor instigating the TI, and 'X' are the remaining bound ligands (4 equatorial and one axial, the latter is in the *trans*-position). All data were obtained from Glenwright and Coe.[1] The influence magnitudes were calculated using **equation 1**.

d-block complex	M-X$_{cis}$ / pm	M-X$_{trans}$ / pm	ITI magnitudes
[CO$^{\text{III}}$(NO)(NH$_3$)$_5$]Cl$_2$	198.1	222.0	1.121
[Co$^{\text{I}}$(CN)$_5$(NO)]·2H$_2$O	203.4	208.1	1.023
(PPh$_4$)$_3$[Re$^{\text{v}}$N(CN)$_5$]·7H$_2$O	212.2	239.1	1.127
(AsPh$_4$)$_2$[Os$^{\text{VI}}$N(CN)$_5$]	202.2	231.1	1.144

1.3.3 Incentives to study the *trans*-influence

There are many incentives for studying the *trans*-influence that go far beyond academic curiosity. The direct implementation of the TI within the kinetic *trans*-effect implies that it would have great use in various industrial[29,30] and biochemical syntheses,[31,32] effectively allowing manufacturers to 'fine-tune' d-block complexes. For example, the *trans*-influence has been utilised in the synthesis of homogenous organic catalysts,[33] and for modelling the function of metal-containing biological molecules such as co-enzymes.[1]

1.4 The Inverse *trans*-Influence in Detail

Much like how the *trans*-influence is found exclusively in d-block complexes, the inverse *trans*-influence is found exclusively in f-block complexes, often with high oxidation states.[34] **Table 1.2** provides some bond length data for several complexes exhibiting the inverse *trans*-influence,[7] the influence magnitudes were calculated using **equation 1**.

Table 1.2. Crystallographic data for some f-block complexes exhibiting the ITI with the $MAnX_5$ structure. Where 'An' is the strong sigma donor instigating the ITI, and 'X' are the remaining bound ligands (4 equatorial and one axial that is in the *trans* position).

f-block complex	$M-Cl_{cis}$ / pm	$M-Cl_{trans}$ / pm	Influence magnitude
$(PPh_4)U^{VI}OCl_5$	253.6	243.3	0.959
$(Et_4N)_2Pa^{V}OCl_5$	264.0	242.0	0.917

As shown in **table 1.2**, clearly the *trans*-bonds (opposite the O ligand, in the axial plane) are longer than the *cis*-bonds (equatorial plane); this results in an influence magnitude value less than 1. In this case, the second species, $(Et_4N)_2Pa^{V}OCl_5$, exhibits a 'higher ITI' on account of its greater deviation from 1 (or lower value).

1.4.1 The f-block Elements

The f-block elements comprise two rows of metals on the periodic table, whose behaviours are dominated by the filling of f-orbitals. They are sometimes considered as inner-transition metals and range from lanthanum to lawrencium. They are further divided into two groups, the lanthanides (cerium to lutetium) and the actinides (thorium to lawrencium).

The actinide series are the interest of this project, specifically complexes of uranium in its 6+ oxidation state with no unpaired electrons.

Different to lanthanide bonding (which is often characterised as ionic in nature),[35] actinide bonding is less clear cut.[36] In the actinides, the greater atomic sizes result in strong relativistic effects, coupled with their weak crystal fields and their large electron correlation potentials all result in a poorly defined valence region for bonding.[36] Typically, their valence region is thought to have contributions from the 5f, 6d and 7s shells.[36] Interestingly, the filled 6p-orbital, that would ordinarily be considered core-like can also play a role in bonding and has been detailed in previous literature.[3,7,8] A generally accepted bonding model is FEUDAL[37,38] (f's essentially unaffected, d's accommodate ligands), which ultimately suggests the d-orbitals in actinide complexes play the structure-determining role, whilst the f-orbitals remain mostly non-bonded. However, ITI-exhibiting species, have been shown to be an exception,[37] where the f-orbitals assume a more prominent and structurally-dictating role.

The most advantageous feature of the actinide elements is their nuclear instability, manifesting as radioactivity. Every known element of the actinide series is radioactive, the half-lives are such that only isotopes of thorium (^{232}Th), uranium (^{235}U) could have survived since the origins of the solar system.[35] Their potential to undergo nuclear fission associates them as sources of nuclear fuel. Due to this, experimental probing of the actinides can be difficult; therefore research naturally turns to theoretical practices,[3,8,36,39] much like in this project.

Actinides play a surprising variety of roles in society, for example, americium is used in certain smoke detectors, by periodically releasing α-particles and/or low energy γ-radiation, that are sequentially and continuously detected. If smoke is present the emitted radiation is intercepted, causing the alarm to sound. Presuming the average house has a negligible background radioactivity, this is a novel application.[40] Other uses for actinides include contrasting agents in nuclear magnetic resonance imaging. Gadolinium, and to lesser extents europium, terbium, dysprosium, thulium and ytterbium are all used. Gadolinium (III) is particularly suitable due to its high paramagnetic (7 unpaired electrons) nature and long electronic relaxation times.[41] The

contrasting agents shorten the relaxation time of nearby water molecules, enhancing the contrast with background tissues.[42]

1.4.2 Uranium and its use in the Nuclear Industry

As uranium is prevalent in this project, we present a very brief discussion concerning its radioactivity, history, and the current climate for uranium mining. Nuclear fission is an energy-releasing process where large nuclei are split into two highly energetic, smaller nuclei, as well as a variable number of neutrons. If there are enough neutrons (and they have the correct energy), they can induce further nuclear fission in neighbouring nuclei, forming a self-propagating chain reaction (a brief depiction of this is shown in **figure 1.5** for a ^{235}U isotope). The kinetic energy of the main colliding fragments is rapidly converted to heat[35] and is subsequently used large scale to generate electricity, although it finds small scale uses such as medicine, space missions, nuclear weapons or desalination.[43] Almost all commercial nuclear reactors use uranium or plutonium (plutonium is produced through neutron bombardment of uranium via two β-decays) due to their readiness to undergo nuclear fission.[35] Thorium fuel cycles do also exist, but are typically not considered as efficient as uranium or plutonium.[44]

$$^{235}_{92}U + ^{1}_{0}n \longrightarrow 2 \times \text{fragments} + x^{1}_{0}n \quad (x = 2\text{-}3)$$
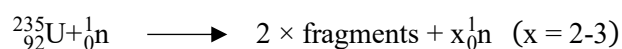
Figure 1.5. a simplified equation showing how the ^{235}U isotope, upon bombardment by neutrons (n), undergoes nuclear fission and splits into two fragment ions and releases more neutrons.

Uranium is one of the more plentiful of the actinide elements, second to thorium with natural abundancies in the earth's crust of 2.8 ppm[43] (thorium at 8.1 ppm).[35] Mined uranium typically exists in a mixture of its various oxidised states, the most common being the uraninite mineral form (also known as pitchblende). Other uranium minerals include carnotite ($KUO_2VO_4 \cdot 3H_2O$) and autunite ($Ca(UO_2)_2(PO_4)_2 \cdot nH_2O$). Extraction of uranium from its ores is dependent on the type of ore, the regional location of the production plant (different countries use different treatments) and the desired product (UO_3, UO_2 or U-metal are often the outcomes). As a general overview, the ore is

crushed, roasted and then leached with sulphuric acid in the presence of an oxidising agent such as MnO_2 or $NaClO_3$ to convert the uranium to the UO_2^{2+} cation.[35]

In 2017, globally, 6,142,600 tonnes of uranium was mined; the top five contributors were Australia (1,818,300 tonnes, 30% of global total), Kazakhstan (842,200 tonnes, 14%), Canada (514,400 tonnes, 8%), Russia (485,600 tonnes, 8%) and Namibia (442,100 tonnes, 7%).[43] Known isotopic proportions of natural uranium exist as ^{238}U (99.27% abundance), ^{235}U (0.72% abundance) and ^{234}U (0.005% abundance).[35] Of which, ^{235}U is the only naturally occurring fissile nucleus; the mechanism for this fission is outlined in **figure 1.5**. The neutrons produced in the fission reaction in **figure 1.5** are considered 'fast neutrons' and typically have around 2 MeV of energy.[35] Problematically, this energy is unsuited to propagate further fission in neighbouring ^{235}U ('slow neutrons' with an energy of around 0.025 eV are preferred). There are two options to counteract this: moderating the 'fast neutrons' with large bulk materials such as graphite or enriching the uranium deposit to increase the proportion of ^{235}U isotope. The early nuclear reactors used metallic uranium, nowadays UO_2 (in the form of pellets or tablets) are used in instead due to their chemical inertness and increased melting point. Uranium carbide (UC_2) is sometimes used also, but ultimately less ideal due to its reactiveness with O_2.[35]

The first manmade self-sustaining chain reaction took place on the 2nd of December 1942 in a deserted squash court at the University of Chicago. This was before nuclear enrichment and so the set-up consisted of 6 tonnes of uranium metal, 50 tonnes of uranium oxide and around 400 tonnes of graphite (acting as a moderator) piled on top of each other. This experiment, carried out by Fermi and his team, ushered in the nuclear age whilst inadvertently inventing the term 'nuclear pile-up.'[35] Following this, the first nuclear reactor was commissioned in 1956 at Calder Hall in Cumberland, UK.

It is interesting to note that the use of uranium in nuclear reactions long predated the squash court in 1942.[45] In May 1972, routine mass spectrometry of UF_6 samples from the Oklo mine in Gabon, central west Africa carried out at the Pierrelatte uranium enrichment facility yielded peculiar results.[45] It was shown that these samples consistently had a low natural ^{235}U isotopic abundance of 0.60% compared to the

expected 0.72%; subsequent investigations into the Oklo deposit gave readings as low as 0.296% abundance.[35] The only known way this could occur to this degree was through a self-propagation nuclear chain reaction, which was predicted to have occurred over two billion years ago. An interesting paper[46] released in 2010 proposes that a historic explosion from a natural nuclear reactor lead to the formation of the moon, as opposed to the generally accepted giant impact hypothesis.

1.4.3 Origins of the inverse *trans*-influence

Looking more closely at the $[UOCl_5]^-$ complex (**complex II** in **figure 1.3**), a crystal centred around the $[UOCl_5]^-$ species was first synthesised experimentally by Bagnell *et al.*[11] Through spectroscopic methods, they showed the *trans*-Cl ligand was shorter in length than the axial *cis*-Cl ligands, and further documented how the $[UOClBr_4]^-$ salt (where the remaining chlorine ligand is *trans*- to the oxygen) could be isolated when reacting a $[UOCl_5]^-$ species with HBr.[11] This stubbornness for the *trans*-ligand to be substituted conclusively implied a superior stability of that *trans*-ligand compared to the equatorial ligands.

The term 'inverse *trans*-influence was coined for the first time in 1992 by Denning.[7] His paper makes a comparison of this relatively unexplored ITI to the much more well-known TI, similar to the focus of this project. Since Denning, the ITI has been demonstrated in a variety of complex molecules with different oxidation states, and varying ligand types. Lewis *et al* consider the ITI in pentavalent uranium(V) complexes with an N-species as the anion.[9] Kovacs and Konings[6] simulated tetravalent $U(VI)OX_4$ (X = F, Cl, Br) structures, of which further highlighted the importance of the *trans*-linear moiety and the effect the ITI can have on molecular stability (their results showed that C_{3v} symmetry with the *trans*-linear X-U-O moiety is preferred[6]). Fryer-Kanssen[3] demonstrate the ITI in a series of imido and carbene analogous to the uranyl species, and Lam *et al*[14] present the ITI in a series of uranium-imide complexes.

In addition to coining the term, Denning[7] also offered an explanation as to the electrostatic origin of the influence, showing its dependence upon the σ-donor's polarisation of the cation,[4,47] as well as comparing this electronic consideration to the *trans*-influence in certain d-block complexes.[7]

1.4.4 The Polarisation Model and the *pseudo*-core 6p-orbital

Denning provides, in his words a "naïve but pleasingly simple" electronic interpretation that provides a framework to fit the TI and ITI, as well as providing elucidation to uranyl's linearity, and ThO_2^{2+} non-linearity (or bent *cis*-geometry). The model describes the anionic σ-donor ligand (O in our case) electrostatically perturbating the metal's core electrons;[7] this perturbation causes a polarisation effect that can be expressed in terms of a dipolar or quadrupolar moment. If the highest filled core orbital of the complex has **opposite parity** compared to the lowest valence orbital, then the moment would be **dipolar**; the resultant effect would be a destabilisation in the *trans*-formation (manifesting in a lengthened *trans*-bond). If the opposite is the case (highest filled core orbital has the **same parity** compared to the lowest valence orbital), then the moment would be **quadrupolar**, and the resultant effect here would be a favouring in the bent *cis*-formation (manifesting as the *cis*-bonds being more contracted relative to the *trans*-bonds)

Considering the octahedral species (**complexes I - IX**) in this project, for the d-block **complexes IV - IX**, the HOMO is the 4p- and 5p-orbitals (for M= Mo(VI) and W(VI) respectively); the LUMO is the partially filled 4d- and 5d-orbitals (again, for Mo(VI) and W(VI) respectively), both of which have opposite parity (the p-orbital being ungerade; the d-orbitals being gerade). Therefore, this causes a **dipolar** effect, resulting in a build-up of negative charge in the *trans*-position (opposite to the O ligand), destabilising and elongating the *trans*-bond exclusively. Inversely, in the case of f-block complexes **I – III**, the HOMO is the filled 6p-orbital (in the U(VI) species) and the LUMO is the unfilled 5f-orbital, of which both have the same parity (ungerade). This manifests as a **quadrupolar** effect, characterised by a build-up of negative charge in the *cis*-positions (relative to the O ligand); correspondingly results in the *trans*-position being the most stable.

However, this is not exclusive to the position of the cation in the periodic table, but more on account of the relative orbital positionings of the metal species. For example, applying this model to the f-block UO_2^{2+} and the ThO_2^{2+} systems, as shown in **figure 1.6**, the former species adopts a linear *trans*-UO_2^{2+} geometry; the latter a bent *cis*-

MoO_2^{2+} geometry expected for d-block complexes. Considering the polarisation model, for the UO_2^{2+} species, the LUMO is the core-like 6p-orbital (ungerade in polarity); the HOMO is the unoccupied 5f-orbital (also ungerade). The HOMO and LUMO, both possessing the **same parity** establishes a quadrupolar character, which resultantly ensures the *trans*-UO_2^{2+} geometry is most favoured. Differently in the ThO_2^{2+} species, the LUMO is still the core-like 6p-orbital (ungerade), but the HOMO in this case is the 6d-orbital (gerade), on account of the thorium's lower charge.[7] The HOMO and the LUMO having **opposite parity** establishes a dipolar character, resulting in the *cis*-ThO_2^{2+} geometry being favoured.[7,13]

Figure 1.6. A comparison of the linear *trans*-UO_2^{2+} species to the bent *cis*-ThO_2^{2+} species ($\theta = 122.2$)[13]

In an additional publication,[48] Denning provides an alternate reasoning that implements the *pseudo*-core 6p-orbital further in the ITI, this time showing how it can relatively **strengthen** the *trans*-bond. They state that the 6p-orbital's involvement in the σ-bond, between the metal centres and the strong σ-donor, leads to a hybridisation with, and a transfer of charge to, the f-orbitals, resultantly leaving a partial core-hole in the 6p-orbital directed in the *trans*-position. This core-hole effectively removes charge from the anti-bonding 6p-orbital; consequently enhancing the overlap between the U-5f orbital and the *trans*-ligand orbitals, strengthening the bonding interaction.[8,48]

Further quantification of the ITI and the 6p-orbital contribution in uranyl and similar complexes ($U(NH_2)_2^{2+}$ and $U(CH_2)^{2+}$) is provided by Fryer-Kanssen and Kerridge through QTAIM simulatiuons.[3] Pierre and Meyer[34] also confirm the role of the *pseudo*-core 6p-orbital in producing the ITI in high oxidation uranium,[34] they describe the bonding in the ITI-exhibiting complexes as a 'synergistic interplay between ionic and

covalent bonding'[34] Suggesting that the charge separation between the U-species and the ligands leads to the inevitable 6p-orbital polarisation, and further 5f-orbital mixing. However, Berryman[37] suggests that the ionic and covalent bonding in the ITI is not synergistic but in fact works against eachother.[37] In an example that is reminiscent of the thorium/uranyl previously described, they show how the presence of a strong σ-donor generates an electrostatic potential at the metal centre, that in terms of ligand coordinating, is *cis*-directing (such as the case of thorium as described). However, when f-orbitals participate more readily (in instances of more efficient orbital-driven covalency), then this ionic effect is overcome; consequently, the *trans*-position is favoured.[37]

Kaltsoyannis *et al*, through DFT methods have quantified the ITI for the MOX_5 complexes that are analysed in this project (**figure 1.3**). Furthermore, they have determined key molecular orbitals influenced by the *pseudo*-core 6p-orbital that contribute to the inverse *trans*-influenece.[8] Interestingly, they also showed that by freezing the 6p-orbital of the f-block species, the ITI was lessened but not fully eradicated.

The excited state section of this project very much builds upon Denning's[7] polarisation model, where we attempt to remove these dipolar and quadrupolar effects (in the TI and ITI respectively) via excitation, in an attempt to effectively remove or reverse the influences.

1.4.5 Incentives to study the inverse *trans*-influence

The implications of the ITI, much like the TI also extends beyond scientific curiosity. The immediate area that would benefit from further actinide research would be the nuclear industry, due to unavoidable participation of the f-block elements in such chemistry. Pierre and Meyer[34] discuss two ways in which this ITI research could benefit the nuclear enterprise: the selective design of actinide extractants, and the development of uranyl sequestration or other chemical remedial technologies.[49] Development of chemical remedial or sequestrating technologies has been hugely successful, most notably via the functionalisation of the U-O bonds that was previously believed to be

chemically inert.[34,50,51] The detailed study of uranium-ligand multiple bonding has also offered new insights into the study of multiple ligand bonding in d-block complexes, which in turn has opened new areas of biologically and industrially relevant reactions of d-block complexes. [34,52]

Chapter 2

Computationally Modelling Chemistry

2.1 Overview of Computational Chemistry

In this project to assesses the $[MOX_5]^-$ complexes (**figure 1.1**), we use a variety of computational chemistry methods including Density Functional Theory (DFT) and its time-dependant derivative (TD-DFT), Quantum Theory of Atoms in Molecules (QTAIM), and Natural Bonding Orbital (NBO) analysis.

Computational chemistry is a powerful tool that is used to predict new and unexplored chemical systems, or used to provide further insights to currently established chemical systems.[53] It is an encompassing discipline that uses mathematical and computer practices, implemented with theoretical and quantum chemical reasonings to model molecular systems. The highly intricate modelling of molecular systems in this way provides a quantitative and qualitative description of that system's electronic behaviour; it is by an understanding of this electronic behaviour in a molecule, that various fundamental principles including chemical bonding, valence regions, and molecular orbitals can be elucidated. Some immediate benefits of computational chemistry include reducing the time and the cost of 'real-world' experiments, as well as improving the safety of certain experiments (considering chemicals that are notoriously hazardous); therefore, computational chemistry is a valuable asset in both chemical industry and research.

2.1.1 Quantum theory and the Schrödinger equation

The heart of both theoretical and quantum chemistry (and then by extension, computational chemistry) really lies with the Schrödinger equation, the most fundamental concept on which non-relativistic quantum theory is based, it is a linear partial differential equation that describes the complex wavefunction Ψ and the total energy E of a quantum system. The wavefunction Ψ is an effective descriptor of the

quantum systems' unique wave-like propagation through space. Considering Born's statistical interpretation of non-relativistic quantum mechanics,[54] the square of the wavefunction gives the real-world probability distribution of that quantum system. In the case of a molecular wavefunction, its squared value will yield the electron distribution of that molecule. In quantum theory we strive for probabilistic knowledge, provided by this statistical interpretation of the wavefunction, as oppose to the more conventional deterministic knowledge.

Equation 2 shows the Schrödinger equation in its reduced, time-independent form, where $\hat{H}$ is the Hamiltonian operator. Applied to a molecular system, solving the Schrödinger equation and finding exact solutions to both the total energy E and the wavefunction Ψ would give all observable information about that molecular system.

$$\hat{H}\Psi = E\Psi \tag{2}$$

The Hamiltonian operator $\hat{H}$ is a sum of the kinetic $\hat{T}$ and potential $\hat{V}$ energy operators. **Equation 3** shows this summation as well as its expansion when applied to a hydrogen atom (or in extension, one-electron systems in general), assuming a fixed nucleus. **Equation 3** and all equations throughout (unless stated) are in atomic units au.

$$\begin{aligned} \hat{H} &= \hat{T} + \hat{V} \\ &= -\frac{1}{2}\nabla_1^2 - \frac{1}{r_{1H}} \end{aligned} \tag{3}$$

For a series of one-electron-like systems, the Schrödinger equation is exactly solvable. In many-body molecular systems however, the Hamiltonian $\hat{H}$ becomes lamentably complicated as shown in **equation 4**.

$$\hat{H} = -\sum_{i=1}^{N}\frac{1}{2}\nabla_i^2 - -\sum_{A=1}^{P}\frac{1}{2m_A}\nabla_A^2 - \sum_{A=1}^{P}\sum_{i=1}^{N}\frac{Z_A}{r_{iA}} + \sum_{j>i}^{N}\sum_{i=1}^{N}\frac{1}{r_{ij}} + \sum_{B>A}^{P}\sum_{A=1}^{P}\frac{Z_AZ_B}{r_{AB}} \tag{4}$$

As the number of bodies in a system increases, the variables to be solved in the potential energy terms (**equation 4** - terms 3, 4 and 5) increase massively; therefore, an exact solution of the Schrödinger equation applied to a many-body system is almost completely intractable.

The central role and yet unavoidable complexity the Schrödinger equation plays in quantum chemistry has been an arduous struggle throughout the years. Resultantly, various approximations categorised as *ab initio* or semiempirical methods have been considered to try and alleviate the many-body problem, the most fundamental being the Born-Oppenheimer approximation (BO). First proposed in 1927, the Born-Oppenheimer approximation proposes that the total molecular wavefunction can be written as a product of the electron and nuclear wavefunctions. This is allowed due to the significant difference in mass (and therefore motion) between the nuclei and electrons. A demonstrative example is shown in **equation 5.** Where the total molecular wavefunction, $\psi(r)$ (LHS) is a function of every nuclear R_i and electron r_i degree of freedom; on the RHS, the Born-Oppenheimer approximation allows for separation of the molecular wavefunction into electronic $\phi(r)$ and nuclear $\Omega(r)$ components.

$$\psi(r_1, r_2, \ldots, r_n, R_1, R_2, \ldots, R_n) \rightarrow \phi(r_1, r_2, \ldots, r_n)\Omega(R_1, R_2, \ldots, R_n) \tag{5}$$

Revaluating **equation 4** with the BO-approximation would see the kinetic energy of the nuclei removed (second term); the nuclei would become 'fixed' and so the nuclear-nuclear interaction energy can be treated as a constant when solving with the remaining potential energy terms.

2.1.2 The Wavefunction Approach

Solving the Schrödinger equation becomes manageable by a series of approximations, like the BO approximation; different methods take different approximations. For the sake of this project, these approximations can be classified into wavefunction and density-based approaches, the former, deals directly with the wavefunction, and includes Hartree-Fock (HF), post-HF and multi-reference methods; the latter is concerned with the observable of the wavefunction (the squared value that gives the electron density) and includes density functional theory (DFT).

The Hartree-Fock (HF) or self-consistent field method (SCF) method is perhaps the most fundamental wavefunction approach, of which nearly all other approaches are based on to some degree. The HF or SCF method makes the intrepid assumption that an n-body wavefunction can be characterised as n-one-electron wavefunctions; that, furthermore, can be represented by a single slater determinant of n-spin orbitals. Approximating an n-electron wavefunction in this way gives a Hartree-product, detailed in **equation 6**. Where $\varphi_0(x)$ represent electronic (atomic or molecular) orbitals. Orbitals are defined and discussed further in **section 2.2.1**.

$$\psi_0 = \varphi_0(1)\varphi_0(2)\varphi_0(3)\dots,\varphi_0(n) \tag{6}$$

The Hartree product effectively takes the assumption that each particle is independent; following this, solving proceeds though the self-consistent-field procedure in which each one-electron wavefunction is singled-out and solved in turn using the remainder wavefunctions as a 'smeared out' and averaged electrostatic field. The cycle is repeated in this way k times, where the energy of ψ_k is essentially the same or *consistent with* the energy of the ψ_{k-1} state.

2.2 Evaluating the Model Chemistry

Modern techniques to computational modelling involve implementing adaptable 'model chemistries' to describe the systems in question. A model chemistry is a term that defines the details of a non-empirical electronic structure calculation that would be required to reproduce the results again. Model chemistries can be fine-tuned to suit certain chemical environments, and often selecting suitable model chemistries becomes a rationale between modeling accuracy (typically compared to like-experimental data) and computational efficiency. A robust model chemistry must be defined as it effectively forms the backbone of any simulation and is carried forward if performing subsequent calculations and obtaining results. The model chemistry in this project include; include basis sets, solvation models, exchange-correlation functionals (for DFT) and dispersion parameters, all of which will be discussed individually in the proceeding sections.

2.2.1 Orbitals and basis sets

The so-called *ab initio* approach, fundamentally, involves likening the real-world many-electron wavefunction to vectors that can be represented in terms of a mathematical basis, a one-electron virtual 'wavefunction' called orbitals.[55,56] This effectively reduces the theoretical wavefunction from its 4N degrees of freedom to a more manageable (and computational) function. Analogous to the conventional statistical interpretation of the wavefunction,[54] orbitals can be used to calculate the probability distribution of an electron at a specific region around the nucleus (by similarly taking the square of the orbital).

Orbitals can come in a variety of flavours including atomic orbitals, planes waves, geminal and numerical functions. Regarding atomic orbitals (AO), for simple atomic species, each orbital can hold a maximum of two electrons and they can be totally described by three of the four quantum numbers: principle quantum number (n - describing the orbitals energy ranging from 1 to infinity, typical systems stay in the 1-8 range however), azimuthal quantum number (ℓ - describing the angular momentum: typically either s, p, d or f orbitals. In certain theoretical cases virtual g orbitals are

considered), and the magnetic quantum number (m_ℓ - of which distinguishes the orbitals available in a subshell and can be used to calculate the azimuthal component of the orbital's orientation in space). The fourth quantum number is the spin quantum number (m_s) describing the occupying electrons spin value. Although not necessary for describing the orbital, the spin quantum number is essential to describing both of the electrons occupying the orbital in order to differentiate between them, concurrently adhering to the Pauli exclusion principle.[55] These AOs are computationally modelled in atomic systems, two particularly common atomic orbital-types used in computational chemistry are the Slater-type orbitals (STO) and Gaussian-type orbitals (GTO), the latter being used throughout this project. Furthermore, in molecular systems where the electron distributions are more complicated, the modelled AOs are utilised in a linear combination of atomic orbitals (LCAO) approach to form molecular orbitals, or their formal computational definitions: basis sets.

Going back to STOs and GTOs, **equations 7** and **8** show the atom-centred radial functions of STO and GTOs (respectively) at a distance 'r' from the nucleus, where 'α' is a nucleus- and state-dependant constant, and 'A' is a normalisation factor used to determine functions 'height' at the nucleus. **Figure 2.1** shows a plot of both orbital types as a function of r,[55] where we see the orbital decays further away from the nucleus.

$$\varphi(r) = Ae^{-\alpha r} \tag{7}$$

$$\varphi(r) = Ae^{-\alpha r^2} \tag{8}$$
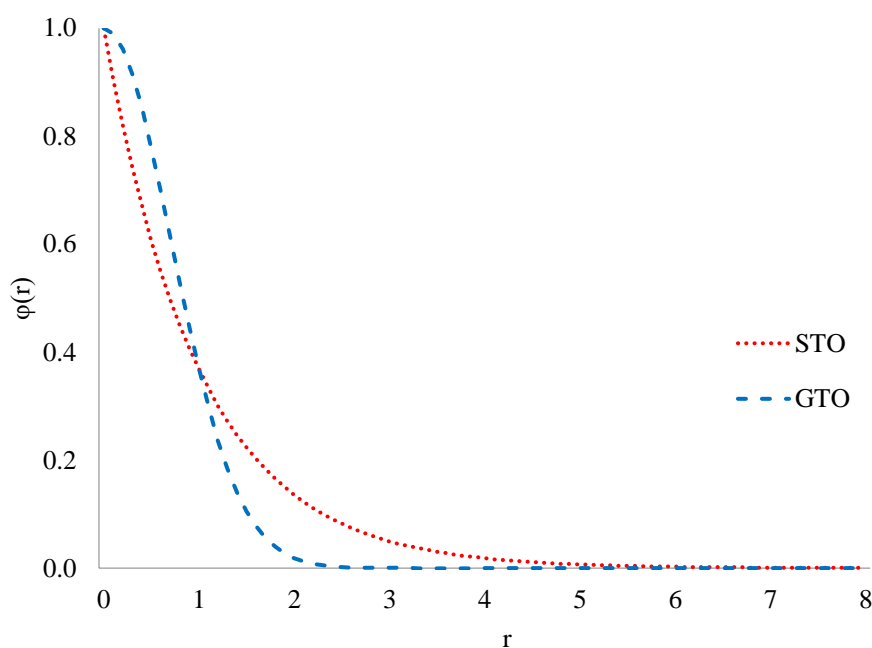
Figure 2.1. radial plot of a typical STO and a GTO (equations 7 + 8 respectively) with increasing distance from the nucleus (r).

STOs are generally accepted to be most efficient at modelling the cusp conditions close to the nucleus ($r \rightarrow 0$), as well as the exponential decay of the wavefunction at distances much further away the nucleus ($r \rightarrow \infty$).[55,57,58] However, STOs are computationally less efficient when modelling molecular systems with more than one atomic centre (as generally their mathematical complexity increases with the number of bodies involved). GTOs, although considered poor when evaluating the cusp and decay conditions,[57] on account of the Gaussian Product Theorem,[59] are effective at handling 8u

systems with multiatomic centres, and exhibit a far greater computational efficiency than STOs.[55] It is therefore customary to linearly combine multiple GTOs to allow the behaviour of STOs to be replicated using the expansion coefficients c_k as 'fine-tuneable' parameters. Overall this achieves a high degree of modelling accuracy for a fraction of the computational cost. The linear combination of 'gaussian primitives' to form contracted basis functions is shown in **equation 9**, Hehre, Stewart and Pople,[60] were the first to qualitatively determine optimal expansion coefficients c_k that would effectively mimic STO's with contracted GTO's.[60]

$$\varphi_p(r, \theta, \phi) = \sum_k c_k \, \eta_i^{\text{Gaussian}} \tag{9}$$

As mentioned, linearly combining GTOs (or any contracted basis function set) form basis sets a set of functions used to model the electronic behavior of an entire molecular system (in the case of atomic orbitals as basis functions, they form molecular orbitals).[3] Basis sets can be fine-tuned with either the adaptable expansion coefficients, or by manipulating the amount of basic functions used, allowing the model chemistry to account for certain unique molecular environments.

It is good practice to use different basis sets for different atoms, as well as different split-basis sets for inner and core regions of those atom.[55] Typically, each basis set is 'fitted' to the expected behaviour of that atom, an O-atom for example would behave more diffusely than a F-atom despite possessing a similar valance description. Additionally, valence regions as a whole are more susceptible to electron delocalisation than the relatively inert core regions, due to actively taking part in bonding interactions. Higher-order spilt-valence basis sets are signified by a $n\zeta$-parameter ($n\zeta = 1$, single, $n\zeta = 2$, double, $n\zeta = 3$, triple etc), where n is the number of basis functions used to define each atomic-species' valence region. For example, a second-row element such as carbon has the electronic configuration: $1s^2 2s^2 2p^2$ where the first core shell can be represented by a 1s basis function; the valence shell represented by the 2s and 2p functions. When characterised by a valence double-ζ basis set, each valence function would be doubled (1 x 1s, 2 x 2s, 6 x 2p)- resulting in 9 basis functions altogether including the core function. If the same element was model by a triple-ζ, each valence function would be tripled (1 x 1s, 3 x 2s, 9 x 2p), resulting in 13 functions altogether, this is shown in **table 2.1**. Typically, a higher value of n (higher ζ value) would imply a higher order of accuracy to the system, this is important for larger systems or systems that contain heavier atoms.

However, the downside to using a larger basis set, is that it usually incurs a greater computational cost. Furthermore, increasing the number of basis functions will move the basis set subsequently closer to the basis set limit; i.e. the point beyond which the addition of extra basis functions has negligible influence on the system. Therefore, it is not always be necessary or feasible to use the largest basis set available. As illustrated in **table 2.1**, the CPU (central processing unit) time generally scales for DFT

calculations (the main method used in this project) formally at m^4 where m is equal to the number of basis functions.

Table 2.1. The effect of CPU scaling (at m^4 where m is equal to the number of basis functions) for a DFT single-point energy calculation is shown for different basis sets. For the first CPU scaling factor, in the cc-pVDZ row, the arbitrary value of α is assigned to represent a CPU time value, the preceding values are scaled according to this value. The basis sets here are part of the correlation-consistent polarised valence family of basis sets.

Basis set	Valence functions	no. of functions	CPU scaling factor
cc-pVDZ	[2 x s], [2 x p], [1 x 3d]	18	1α
cc-pVTZ	[3 x s], [3 x p], [2 x d], [1 x f]	34	12.7α
cc-pVQZ	[4 x s], [4 x p], [3 x d], [2 x f], [1 x g]	59	115.4α
cc-pVPZ	[5 x s], [5 x p], [4 x d], [3 x f], [2 x g], [1 x h]	95	775.9 α

Polarised basis sets involve basis sets with additional basis functions that possess a higher azimuthal number than the basis functions of a minimal basis set.[55] For example, a polarised basis set for a molecular system with a valence region comprised of p-orbital functions would also include a set of additional d-orbital functions. The benefit is that polarisation functions provide additional flexibility to the basis set when modelling systems with more distorted electron density, particularly in environments where high levels of polarisation occurs such as bonding regions.

Augmented basis sets or diffuse basis sets involve the addition of more diffuse basis functions to the basis set. They are often considered in systems with a greater spatial diffuseness; i.e. systems where the electrons are more likely to be found at greater distances from the nucleus.[55,57] This is particularly useful when describing anionic systems or systems with a non-ground state configuration.

To find the most efficient basis sets in the model chemistry to describe the molecular systems (**I – IX, figure 1.1**) went as follows. It was decided that the central elements (uranium, molybdenum, tungsten) and the main group elements (oxygen, chlorine, fluorine, bromine) would be described using different basis sets. Instinctively this was due to the uranium species (molecules **I – III**) being relatively heavier and additional relativistic parameters would need to be considered when modelling with a basis set.

To keep consistency, the central d-block species in molecules (**IV** – **IX**) were assigned the same basis sets (minus the relativistic parameters) as the uranium, it should be noted that there are not as many basis sets available for actinide elements such as uranium, relative to other elements in the periodic table.

To decide on a suitable basis set for the main group elements, eight different basis sets were compared: def2-SVP, def2-TZVP, cc-pVDZ, cc-pVTZ, cc-pVQZ, aug-cc-pVDZ, aug-cc-pVTZ, aug-cc-pVQZ (obtained from the TURBOMOLE[61] library, references and details are provided in **section 2.2.5**). DFT geometry optimisation calculations (using B3LYP exchange-correlation functional throughout) were performed on the same control molecule using different basis sets, **table 2.2** shows the results in terms of bond lengths as well as the CPU time.

Table 2.2. DFT geometry optimisation of the $[UOCl_5]^-$ molecular system using a B3LYP functional, different basis sets have been taken from the TURBOMOLE[61] basis set library, and have been used to model the main group elements (Cl, O), references and further definitions are provided in **section 2.2.5**. The central uranium atom's basis set is kept constant. In a similar fashion to **table 2.1**, we opt to present the CPU times scaled from the lowest CPU time β, for the def2-SVP basis set

	D_{U-Cl} (*cis*) / pm	D_{U-Cl} (*trans*) / pm	Influence magnitude	CPU scaling factor
Experimental:	*253.6*	*243.3*	*0.959*	*-*
Basis set				
def2-SVP	257.0	251.6	0.978	β
def2-TZVP	257.5	251.5	0.977	2.5 β
cc-pVDZ	257.3	251.6	0.978	2.2β
cc-pVTZ	257.7	251.6	0.977	2.4β
cc-pVQZ	257.8	251.7	0.976	6.5β
aug-cc-pVDZ	257.7	251.6	0.976	2.2β
aug-cc-pVTZ	257.8	251.7	0.976	6.1β
aug-cc-pVQZ	257.9	251.7	0.976	16.6β

Table 2.2 shows that in terms of bond distances, the basis set does not have much of an impact, suggesting the model chemistry is approaching the basis set limit. Literature shows the full capability and flexibility of Dunning's correlation-consistent basis sets when modelling high valence molecular environments.[55] Additionally, the anionic nature, excited state calculations (see section: excited states) and QTAIM analysis (see section: QTAIM) of molecules (**I** – **IX**) imply that using augmented

basis sets would be advisable.[55] This effectively narrows the basis set choice down to three: aug-cc-pVDZ, aug-cc-pVTZ, aug-cc-pVQZ, the correlation-consistent Dunning types.[62] **Table 2.2** shows that CPU time scale massively, tripling from 2.2β to 6.1β for the aug-cc-pVDZ to aug-cc-pVTZ; then nearly tripling again to 16.6β for the aug-cc-pVQZ. Recent literature[63] states the ineptness of the double-ζ for quantum theory of atoms (QTAIM) approach, one of the forms of characterisation at the ground state we employ in this project; further recommend using a higher-order Dunning type. Considering these factors, using a triple-ζ seems like a good compromise of chemical accuracy and computational costs.

In summary, the aug-cc-pVTZ basis set was decided to be best suited to model the main group elements (oxygen, fluorine, bromine, chlorine) in the molecular systems (**I – IX**). Details of the basis sets used for the f-block and d-block species (U, Mo, and W) are provided in the computational details section (**section 2.3**).

2.2.2 Density Functional Theory (DFT)

Density Functional Theory (DFT) is a computational method used widely in various disciplines including physics, chemistry and materials science. It is used to investigate the electronic structure of many-body systems, the majority of which include atoms, molecules and condensed phase systems. Between the years of 1980 and 2010, DFT is credited as the most active field (in terms of recognised citations) in physics.[64,65] Its true heritage lies with Hohenberg, Kohn and Sham,[66,67] these seminal works were published in 1964 and 1965. But its central ideas can be traced back to Hartree-Fock theory and the Thomas-Fermi method.[68,69]

The uniqueness of DFT compared to other *ab initio* approaches is that it sets out determining the electronic energy exclusively from the electron density, as opposed to the wavefunction that most other approaches take. Modern DFT calculations are reliant upon the Kohn-Sham approach, a methodology predated by two theorems by Hohenberg and Kohn in 1964. The first theorem states that the ground state electronic energy can be determined completely by the electron density ρ.[66,70] This is remarkably

convenient as it effectively bypasses having to directly deal with the complex wavefunction (complex in both the mathematical and difficult sense). Instead of relying on the traditional 4N-variable (3 spatial and 1 spin for each electron) wavefunction, DFT is only concerned with the three spatial coordinates (+1 spin) which constitute the electron density.

Connecting the electron density ρ to the total energy of the ground state is achieved with a functional- a function of a function. A function is a set of instructions to transform a number to another number. A functional would be a function of which its input is another function, but which still returns a number. The first function would have spatial coordinates r as an input, and electron density ρ at point r as the output. The second function(al) would then use the electron density function as input and give the total ground state energy E_0 as an output, **equation 10** shows this, where F is the unknown functional term that relates the E_0 and ρ_0. **Equation 11** shows a 'normalisation' condition where the integral of the electron density would have to equal the number of electrons, n.

$$E_0 = F[\rho_0(\boldsymbol{r})] = E[\rho_0(\boldsymbol{r})] \tag{10}$$

$$n = \int \rho(\boldsymbol{r}) d\boldsymbol{r} \tag{11}$$

Considering the first theorem (mathematically defined in **equation 10**), it indicates that the only indefinite parameter between linking the electronic density ρ to the actual energy of the ground state would be the functional F used (i.e. what the set of instructions are to link the two factors). That is why this theorem is more appropriately titled an 'existence theorem…' it tells us there is in principle a way of calculating the energy from the density (using a functional) but it doesn't tell us how or what the functional is.[57] The second theorem states that any trial electron density ρ will always give energy higher (or equal if the ρ were the exact true electron density) to the ground state energy. Moreover, by varying the trial electron density ρ_t, the value that minimises the total energy will be the exact ground state energy.[57] This is called the variational theorem, **equation 12** gives an overview.

$$F[\rho_t] \geq E_0[\rho_0] \tag{12}$$

Equation 13 shows the expansion of the Hamiltonian (from **equation 4**) in terms of energy functionals of the electron densities, showing the kinetic energy functional, $T[\rho(\boldsymbol{r})]$, the nucleus-electron interaction functional $V_{ne}[\rho(\boldsymbol{r})]$ and the electron-electron interaction energy functional $V_{ee}[\rho(\boldsymbol{r})]$.

$$E[\rho(\boldsymbol{r})] = T[\rho(\boldsymbol{r})] + V_{ne}[\rho(\boldsymbol{r})] + V_{ee}[\rho(\boldsymbol{r})] \tag{13}$$

The main difficulty in solving the Schrödinger equation for a many-electron system lies in the final potential energy terms in the Hamiltonian. To elucidate this in DFT methodologies, Kohn and Sham proposed a fictitious system in which there were no interactions between electrons in which the system's electron density ρ is identical to the ground state density of a real electron-interacting system, this is shown in **equation 14**.

$$\rho^{KS}(\boldsymbol{r}) = \rho_0(\boldsymbol{r}) \tag{14}$$

Equation 15 shows the total electron density ρ of a non-interacting system expressed as a sum of the eigenfunctions of one-electron operators called Kohn-Sham orbitals. Solving this type of system is analogous to the HF/SCF approach, except in this case a new functional term is included to account for the electron interactions.

$$\rho^{KS}(\boldsymbol{r}) = \sum_i^m \left| \varphi_i^{KS}(\boldsymbol{r}) \right|^2 \tag{15}$$

From this, an expansion of the total 'real' energy functional $E^{KS}[\rho(\boldsymbol{r})]$ can be expressed as a sum of the non-interacting independent energies as well as an exchange-correlation functional term that accounts for all differences between an interacting and non-interacting system. This expression is shown in **equation 16**, terms include the non-interacting kinetic energy $T_{ni}[\rho(\boldsymbol{r})]$, nuclear-electron interaction $V_{ne}[\rho(\boldsymbol{r})]$, coulomb repulsion between electrons $J[\rho(\boldsymbol{r})]$, and the unknown exchange-correlation functional $E_{XC}[\rho(\boldsymbol{r})]$.

$$E[\rho(\boldsymbol{r})] = T_{\text{ni}}[\rho(\boldsymbol{r})] + V_{\text{ne}}[\rho(\boldsymbol{r})] + J[\rho(\boldsymbol{r})] + E_{\text{XC}}[\rho(\boldsymbol{r})] \tag{16}$$

The first three components in **equation 16** (functionals of a non-interacting system) can be calculated in a similar fashion to the HF method, it is the exchange-correlation functional that is of the concern of DFT methodology. As shown in **equation 17**, the exchange-correlation functional, can be further expanded in terms of the kinetic energy contribution (the difference between the interacting and non-interacting), $\Delta T^{\text{I}}[\rho(\boldsymbol{r})]$, the exchange contribution from electron-electron interactions $V_{\text{ee}}^{\text{X}}[\rho(\boldsymbol{r})]$, and the correlation energy from electron-electron interactions $V_{\text{ee}}^{\text{C}}[\rho(\boldsymbol{r})]$.

$$E^{\text{XC}}[\rho(\boldsymbol{r})] = \Delta T^{\text{I}}[\rho(\boldsymbol{r})] + V_{\text{ee}}^{\text{X}}[\rho(\boldsymbol{r})] + V_{\text{ee}}^{\text{C}}[\rho(\boldsymbol{r})] \tag{17}$$

From here, it is convenient to adopt the typical DFT notation for the exchange-correlation functionals;[55] this is shown in **equation 18**, where the relationship between energy density ε^{XC} and electron density ρ[55] can clearly be seen.

$$E^{\text{XC}}[\rho(\boldsymbol{r})] = \int \rho(\boldsymbol{r})\varepsilon^{\text{XC}}[\rho(\boldsymbol{r})]d\boldsymbol{r} \tag{18}$$

The exchange-correlation functional is very much where the variation part of DFT resides, where if the exact functional is known, then the DFT calculations are exact. Through the years, multiple different approaches to calculating this XC-functional effectively have been thoughtfully considered. These programmed 'exchange-correlation functionals' (XC-functionals) such as LDA's, GGA's and hybrid-GGA's have become a sporting debate amongst computational scientists about which functionals give the most accurate depiction. **Section 2.2.3** details how different XC-functionals handle the exchange-correlation energy as well as how we specifically decided on which functional to use for this project.

2.2.3 Exchange-correlation Functionals

Table 2.3 shows the results in terms of bond lengths of a DFT geometry optimisation (of the $[UOCl_5]^-$ system), using seven different XC-functionals, as well as showing the different functional types. The different functional *types* all offer a different methodology for estimating the exchange-correlation energy, and the different functionals themselves have a unique implementation of their functional-types methodology. For example, the hybrid-GGA's (hybridised General Gradient Approximation) BHHLYP and PBE0 both use the general approach to incorporate the exact HF-exchange energy in their approximations, but individually do so in their own characteristic ratios (we provide further details of this later on). This inevitably raises the challenge as to what functional would be best to use; unfortunately, there is no easy answer to this. Although, there is a generally accepted hierarchal approach to the functional type's performance, and typically different systems may respond better do different XC-functionals, and so it is customary to compare the performance of different functionals.

Table 2.3. the results of a geometry optimisation on a $[UOCl_5]^-$ system using different functionals. Experimental values were obtained from Denning's 1992 paper.[7] References for XC-functionals are provided in **section 2.3**.

Functional	Functional type	D_{U-O} / pm	D_{U-Cl} (*cis*) / pm	D_{U-Cl} (*trans*) / pm	Influence magnitude
Experimental:			*253.6*	*243.3*	*0.959*
Functional	Functional type				
PBE0	Hybrid-GGA	175.69	254.66	247.73	0.973
PBE	GGA	180.06	256.49	252.14	0.983
B3LYP	Hybrid-GGA	177.8	257.53	251.46	0.976
BHHLYP	Hybrid-GGA	173.35	256.56	246.97	0.963
TPSS	Meta-GGA	179.8	256.60	252.19	0.983
TPSSh	Meta-Hybrid-GGA	177.99	255.75	250.36	0.979
BLYP	GGA	181.83	259.92	255.88	0.984

First quantified by Perdew *et al*,[71] the 'Jacob's Ladder of DFT approximations' gives an insightful comparison of XC-functional types. The ladders 'rungs' go as follows, from least chemically accurate to most: LDA, GGA, meta-GGA, hybrid, random phase approximation (RDA).[71] It is largely accepted that Local Density Approximation

functionals (LDA's) are now outdated by the more universally accurate Generalised Gradient Approximations (GGAs), and their derivatives (meta-GGAs and hybrids. LDAs however really should be given credit for providing the foundations of which higher approximation functionals (GGA, meta-GGA) are all formulated upon.

The LDA approach gives the exchange-correlation energy E^{XC} by simply assuming the energy density ε^{XC} at every point in the molecule is solely dependent upon the electronic density ρ at that point.[57] The LDA expansion for exchange-correlation energy E^{XC} is shown in e**quation 19**. Typically, they are known to over-estimate the correlation energy whilst underestimating the exchange energy. And as such they are best suited for more homogenous systems, as opposed to molecular systems, but nonetheless find their place on the bottom rung Jacobs's ladder of computational chemsitry.[65]

$$E_{\text{LDA}}^{\text{XC}}[\rho(\boldsymbol{r})] = \int \rho(r)\varepsilon^{\text{XC}}[\rho(\boldsymbol{r})]\,d\boldsymbol{r} \tag{19}$$

GGA functionals (PBE[72] and BLYP[73–75] in this case) offer an improvement to the LDA approach by including a third term in the exchange-correlation energy: the gradient of the electron density $\nabla\rho$. The inclusion of this first-order differential means that the exchange-correlation functional will additionally consider how the electron density ρ at every point is locally changing (gradient).[55] Resultantly, the GGA functionals' overestimation of the correlation energy (over binding energy) is far less significant than that of the LDA functionals.[65] However there is still a self-interaction parameter that results in a higher degree of binding energy than expected.[76] The GGA functionals in this project include the PBE and BLYP functionals. The general expansion for a GGA functional is shown in **equation 20**.

$$E_{GGA}^{\text{XC}}[\rho(\boldsymbol{r})] = \int \rho(r)\varepsilon^{\text{XC}}[\rho(\boldsymbol{r}),\nabla(\boldsymbol{r})]\,d\boldsymbol{r} \tag{20}$$

Staroverov and Scuseria). Such functionals follow from the GGAs first-order gradient corrections by introducing a second-order gradient correction parameter- the Laplacian of the electron density via the kinetic energy gradient τ.[77] The expansion for a general meta-GGA is shown in **equation 21.**

$$E_{\text{mGGA}}^{\text{XC}}[\rho(\boldsymbol{r})] = \int \rho(\boldsymbol{r})\varepsilon^{\text{XC}}[\rho(\boldsymbol{r}), \nabla(\boldsymbol{r}), \nabla^2(\boldsymbol{\tau})]\, d\boldsymbol{r} \qquad (21)$$

Meta-GGA functionals provide a convincing approach to further reduce the over binding energy of the GGA functionals. Specifically, it does so by correcting the self-interaction parameter that the GGA correlation functionals still exhibit.[78] Although an improvement over most GGA functionals, meta-GGAs are typically considered not as effective as hybrid-GGA functionals.[76,79]

Hybrid functionals (e.g. PBE0,[80] B3LYP,[73–75,81–83] BHHLYP,[73–75,81] TPSSh[84,85]) were first proposed by Becke in 1993 as a new and improve method to calculate the exchange-correlation energy.[65,86] The intuition lies in 'hybridising' the GGA exchange with exact orbital exchange that is calculated using the Hartree-Fock exchange energy expression. With hybrid-GGAs, the exchange-correlation energy E^{XC} is now a sum of the DFT exchange energy E_{DFT}^{XC} and the Hartree-Fock exchange energy E_{HF}^{X}, still with full DFT correlation. **Equation 22** shows a generalised expansion of the exchange-correlation energy for a conventional hybrid functional, where the value of α determines the ratio of DFT/HF exchange energy.

$$E_{\text{hybrid}}^{\text{XC}}[\rho(\boldsymbol{r})] = \alpha E_{\text{HF}}^{\text{X}}[\rho(\boldsymbol{r})] + (1 - \alpha)E_{\text{DFT}}^{\text{X}}[\rho(\boldsymbol{r})] + E_{\text{DFT}}^{\text{C}}[\rho(\boldsymbol{r})] \qquad (22)$$

The exact ratios of HF-exchange and DFT-exchange used in a hybrid functional are characteristic of that specific XC-functional.[57,70] For example, the PBE0 functional combines the standard Perdew-Burke-Ernzerhof (PBE) GGA exchange to Hartree-Fock exchange in a 3:1 ratio; additionally it includes the PBE correlation, this is shown in **equation 23**.[80]

$$E_{\text{XC}}^{\text{PBE0}}[\rho(\boldsymbol{r})] = \frac{1}{4}E_{\text{HF}}^{\text{X}}[\rho(\boldsymbol{r})] + \frac{3}{4}E_{\text{PBE}}^{\text{X}}[\rho(\boldsymbol{r})] + E_{\text{PBE}}^{\text{C}}[\rho(\boldsymbol{r})] \qquad (23)$$

The hybridisation of GGAs with exact orbital exchange typically improves the simulation of various molecular properties including bond lengths, atomisation energies and vibrational frequencies.[86] B3LYP is another common hybrid functional. Characteristically, for the exchange parameter, B3LYP blends the Becke88[73] (B88X)

gradient correction local spin density functional (LSD) exchange and exact orbital exchange; then for the correlation parameter it uses the 'LYP' correlation functional proposed by Lee, Yang and Parr.[73,74] **Equation 24** shows the expansion of the B3LYP functional, where E_{HF}^{X} is the exact HF-exchange functional, E_{B88X}^{X} is the exchange term from the becke88 functional, E_{LSDA}^{X} is the LSDA exchange and correlation functionals, E_{LYP}^{C} is the correlation functional proposed by Lee, Yang and Parr. B3LYP's credibility and popularity has been outstandingly cemented through the years, proving to be one of the more robust and reliable functionals. Evidenced by it being the most cited functional in DFT methodology. [87,88]

$$E_{XC}^{B3LYP} = 0.2E_{HF}^{X} + 0.8\left(E_{LSDA}^{X} + 0.9E_{B88X}^{X}\right) + 0.81E_{LYP}^{C} + 0.19E_{LSDA}^{C} \qquad (24)$$

Meta-GGA hybrid functionals, much as the name suggests are hybridised versions of meta-GGAs. The TPSSh functional is the only meta-hybrid considered in this project.

Returning to **table 2.3**, the influence magnitudes are consistently overestimated compared to the experimental data. The **BHHLYP** functional gives the closest results to the experimental influence magnitude (only overestimating by 0.4%). Additionally, the **BHHLYP** *trans*-bond distance is also the closest to the experimental value compared to the other functionals (differing by around +1.5%). The *cis*-bond distance however is most accurately predicted by **PBE0**. A plot of the data from **table 2.3** is shown in **figure 2.2**, where the values for each functional are plotted as deviations from the experimental idealised bond distances that would give the correct influence magnitude. **Figure 2.2** further clarifies the ability of the **BHHLYP** functional to most accurately predict the *trans*-bond distance; the **PBE0** functionals ability to most closely predict the *cis*-bond length compared to experimental data. Comparing to the previously simulated data from Kaltsoyannis *et al,*[8] differently to the experimental data, all functionals under-predict the ITI. The **PBE0** functional appears to reside in a desirable middle ground between the simulated and experimental data, as does the **B3LYP** in terms of just the ITI magnitude.
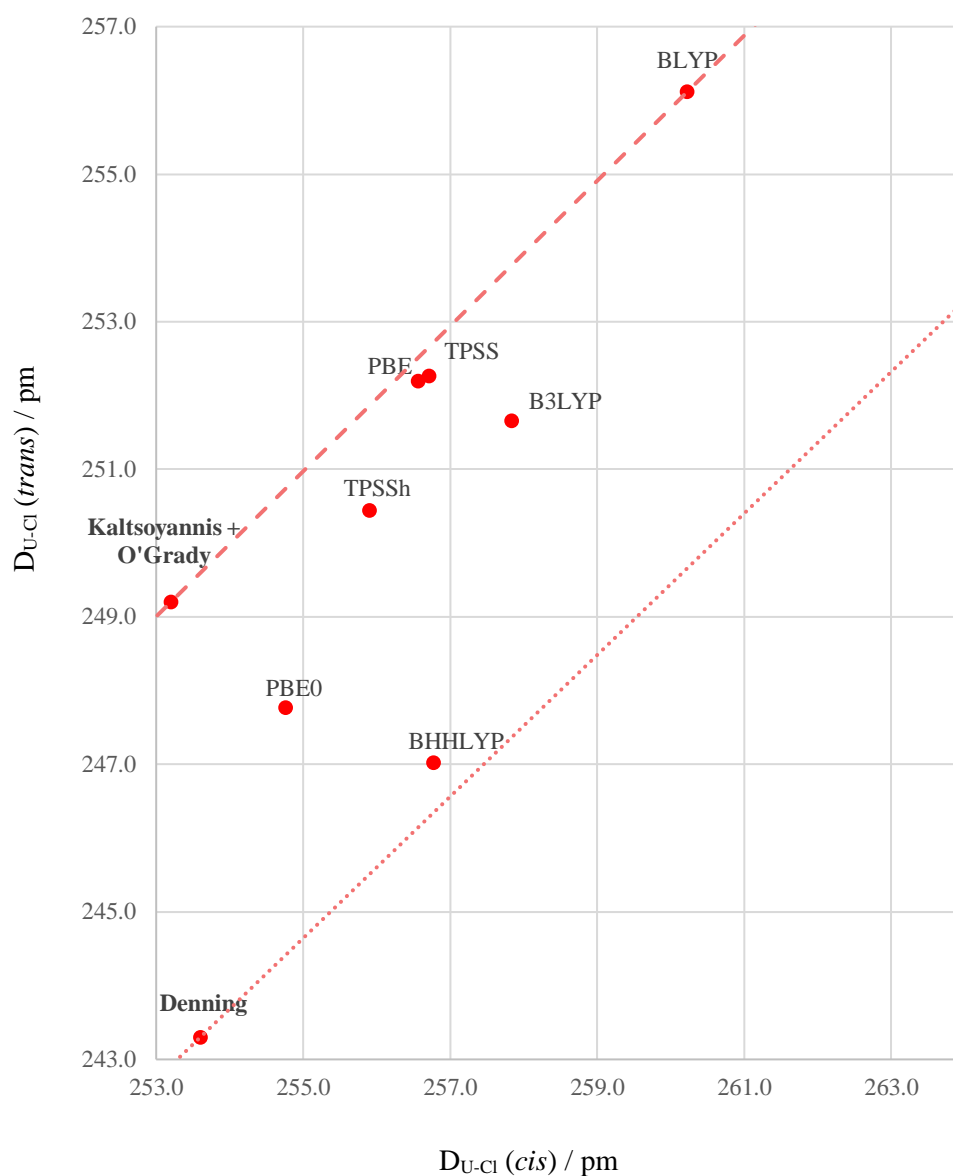
Figure 2.2. plot of the optimised bond length data for the $[UOCl_5]^-$ system using different XC-functionals. The dotted line denotes the 'idealised' cis/trans lengths to obtain the ITI magnitude value of 0.959, taken from experimental data (Denning, 1992), the dashed line shows the same but for simulated data (Kalsoyannis and O'grady, 2002).

In total, we acknowledge that the XC-functionals tested all perform fairly similarly, with little incentive to choose one over the other. In addition, we consider that more applied levels of computational chemistry would be assessed beyond just geometry optimisations at the ground state (excited state chemistry, topological approaches in the ground state). Therefore, it was decided that the **B3LYP** XC-functional would offer the most robust and reliable DFT-implementation. Its high regard in various

cited molecular systems[6,88–90] provides an assurance that our results will be consistently well-modelled.

2.2.4 Further Modelling Parameters

In chemistry, inter- and intra van der Waal forces (London dispersion forces + dipole-diploe forces) play a large role in the majority of chemical systems.[2] The TURBOMOLE[61] program (of which the DFT-calculations are performed on in this project) has factored in these parameters by using a general empirical dispersion correction parameter for DFT calculations (DFT-D),first proposed in 2004[64] followed by two subsequent refinements:DFT-D2 and DFT-D3.[64] The most recent model (DFT-D3, proposed in 2010) boasted a higher specification and lower empiricism computed from more first-principle approaches, it was also suggested that this would probably be the limit of the DFT-D method.[91] Although the systems in this project exist as isolated molecules with zero intermolecular interactions, their highly ionic nature would exhibit different intramolecular interactions. Grimme *et al*[91] cites the DFT-D3 approach an easily-programable, robust method for force calculation that has been shown to accurately model the entire periodic table as well as several different types of systems (including heavier systems). Considering this, the DFT-D3 correction parameter was also used throughout this project.

When a solute is immersed in a solvent, its charge distributions can interact with that solvent. The computational answer to this phenomenon, is to represent the solvent as continuous medium that is characteristic of its dielectric constant (ε); different media will have different values of ε. The continuum involves averaging the theoretical solvent's charge distribution, at its thermal equilibrium, and modelling it as a continuous electric field over all degrees of freedom.[1] The region of this continuum occupied by the molecule is called the reaction field. Using a continuum model naturally allows more specificity to likening computer simulations to the real-world physical processes taking place; typically, they are used extensively in the computational sectors of biochemistry, biophysics and medicinal chemistry, amongst other key areas in industry.[92] In the case of this project, a conductor-like screening model (COSMO) was attempted. Here, the dielectric constant of the medium is given the value of infinity, essentially reducing any electric potential at the reaction field to zero.[93] Details of the

molecular cavities are given in the computational details section. The COSMO model was carried forward through the QTAIM and NBO sections but was found to be a limiting factor in the excited state TD-DFT sections; therefore, the COSMO parameter was removed (and the NBO and QTAIM analysis was rerun). Conveniently, a paper[94] was recently published suggesting that for certain actinide complexes, the inclusion of COSMO in simulations (specifically pertaining to QTAIM analysis), is unnecessary; that overall, the environmental effects of including this parameter are in fact minor and do not account for the differences between computational and experimental values.[94] **Table 2.4** presents the bond lengths of some trial simulations of the $[UOCl_5]^-$ complex with and without the parameters outlined above.

Table 2.4. Trial simulations of the $[UOCl_5]^-$ complex (functional: B3LYP) showing the effects different additional parameters (solvation and dispersion) has on bond lengths pm, as well as the ITI magnitude, the experimental values for the complex are also presented from Denning.[7] The final model chemistry used involved just the dispersion parameters, and is presented in bold.

	$D_{U\text{-}Cl\,(cis)}$ / pm	$D_{U\text{-}Cl\,(trans)}$ / pm	Influence magnitude
Experimental	*253.6*	*243.3*	*0.959*
Standard	257.8	251.7	0.976
Solvation	257.4	250.0	0.971
Dispersion	**257.5**	**251.5**	**0.976**
Solvation + dispersion	257.2	249.8	0.971

As shown in **Table 2.4**, the effects on the bond distances are minimal; the low programmability of the dispersion parameter convinces us that it is a worthwhile addition, as for the COSMO model, efforts to include the solvation parameter in the excited state optimisations are suggested as further work in the conclusion section.

2.3 Computational Details

We present here an overview of the model chemistry, and details of the computational software used in this project. All DFT calculations (including escf[95] and egrad[96,97]) were performed using version 6.6 of the TURBOMOLE software package.[61] Several exchange-correlation functionals were considered including PBE,[72] PBE0,[80] BLYP,[73–75] BHHLYP,[73–75,81] B3LYP,[73–75,81–83] TPSS,[98] and TPSSh,[84,85] of which the hybrid-GGA B3LYP[73–75,81–83] functional was selected on account of its versatility and suitability to these systems. A DFT-D3 dispersion correction was also used.[91]

Several basis sets were tested, including the cc-pVDZ through to cc-pVQZ (plus their augmented versions) for the for the main group (O + F),[62,99] Cl,[100] and Br[101] species, as well as the def2-SVP[102] and def2-TZVP[103] basis sets from the TURBOMOLE library. It was decided that Dunning + co-workers' augmented triple-ζ polarised correlation consistent basis set, aug-cc-pVTZ[99–101] would be the best suited. For the U species, sixty core-electrons were replaced with the small-core pseudo-potentials of Dolg and co-workers,[104,105] employed alongside the corresponding electron basis set of polarised triple-ζ quality.[106] For the Mo and W species, twenty-eight and sixty core-electrons (respectively) were replaced with small-core pseudo-potentials,[107] employed with the corresponding electron basis set of quadruple-ζ quality.[108]

The bond orbitals in the $[MOX_5]^-$ species were assessed via a Natural Bond Orbital analysis (NBO), computed with the software package of the same name.[109] The topological analysis of the $[MOX_5]^-$ bonding was evaluated using the Quantum Theory of Atoms in Molecules (QTAIM) approach,[110] via the AIMAll software package.[111] Any details relating to molecular orbital information, as well as any diagrams of molecular orbitals presented in this project were obtained using version 3.6 of Multiwfn.[112]

2.4 Theory behind the Ground State Analyses

The ground state characterisation of **complexes I – IX** (from **figure 1.3**) proceeds through three analyses: bond length, topological, and bonding-orbital NBO. We present in this section a brief overview of the theory behind the latter two metrics, Quantum Theory of Atoms in Molecules (QTAIM), and Natural Bond Orbitals (NBO).

2.4.1 Quantum Theory of Atoms in Molecules

QTAIM is a unique form of molecular modelling that relies on the topological expressions of the electron density, $\rho(r)$, to be indicative of the electronic and molecular structure. QTAIM is not the only density-based approach to exist, other examples include electron localisation function analysis (ELF),[113,114] Hirshfeld[115] and natural bond order (NBO),[116] the latter of which is also used in this project (**section 3.4**). However, in recent years QTAIMs ability to deliver numerous different methods for bonding characterisations in a coherent and rigorous context has earned itself a formidable reputation.[3,36,94] Some of these methods include analysis of bond critical points (BCP), delocalisation indices (DI), natural atomic charges and atomic volumes. Due to the unique valence regions pertaining to the bonding in f-block chemistry, the different analysis methods of QTAIM are ideal as they provide a multitude of qualitative information to compare to other QTAIM structures, there are various literature pertaining to QTAIM analysis and f-block chemistry.[3,36,41,94,117–119]

In this project, the software AIMAll[111] was used to perform qualitative and visual QTAIM calculations (the latter using the accompanying AIMStudio package). A QTAIM approach to the ITI and the TI is intuitive as ideally, it would give quantitative data relating to the different intrinsic properties of the *cis-* and *trans-*bonds respectively. ITI-exhibiting f-block molecules have previously been evaluated using QTAIM analysis, including molecules of the UAn_2^{2+} (An = O, N, CH_2)[3,34] and the tetravalent analogous to molecules (**I-III**): UOX_4 (X = F, Cl, Br).[6]

The QTAIM analytical approach was chiefly developed by Bader and his research group at McMaster University.[110,120] Fundamentally, QTAIM partitions a molecular

system into chemically distinguishable, contiguous, space-filling atomic basins. Each atomic basin can be defined by a zero-flux condition presented in **equation 25**, where $\rho(r)$ is the electron density and n(r) is a unit vector normal to the surface at point r.[36]

$$\nabla\rho(\boldsymbol{r}) \cdot n(\boldsymbol{r}) = 0 \tag{25}$$

Figure 2.3 illustratively shows the topological partitioning of the $[UOCl_5]^-$ complex (**molecule II** in **figure 1.3**) into atomic basins, disseminated from its electron density.
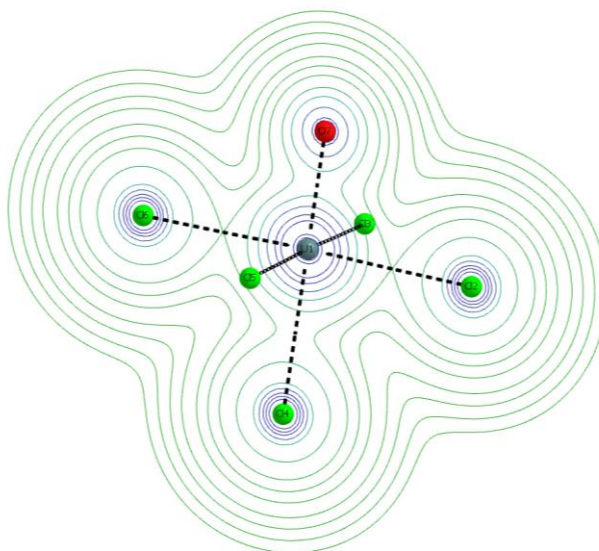
Figure 2.3: a 2-dimensional GradRho $\nabla\rho(\boldsymbol{r})$ contour map of the $[UOCl_5]^-$ species (where the plane lies in the z-plane encompassing the O-U-Cl*trans* moiety), showing the topological partitioning of a QTAIM molecule into its atomic basins.

Partitioning a molecular system into these 'topological atoms'[120] allows properties such as atomic sizes, atomic density, and nuclei positioning to be described by comparable quantum expectation values.[121] Considering an interatomic region between two nuclei in a molecule (in QTAIM, what is typically considered a 'bond' is called a **bond path**), the bond path follows a gradient path of steepest ascent that terminates at $\nabla\rho(\boldsymbol{r}) = 0$, signifying a nucleus; this nucleic terminus is called an nuclear **critical point** (NCP).[110,120] Considering a bond path between two nuclei, following a gradient path of $\rho(\boldsymbol{r})$ with the steepest descent will yield a point of minimal $\rho(\boldsymbol{r})$ before reaching the adjacent nuclei,[122] this is called a **bond critical point** (BCP). Essentially, the BCP is a

saddle-point region of minimal electron density,[120] where direction of the 'saddle' follows a gradient path of increasing $\rho(r)$ towards two different NCP. In accordance to this, there are two other types of critical points: ring critical points (RCP) and cage critical points (CCP). A simple overview to critical points can be mathematically illustrated by **equation 26**, where The Laplacian of the electron density (gradient path along a bond path) goes to the zero vector only at a critical point.[123]

$$\nabla\rho = \mathbf{i}\frac{d\rho}{dx} + \mathbf{j}\frac{d\rho}{dy} + \mathbf{k}\frac{d\rho}{dz} \rightarrow \begin{cases} = \vec{0} & \text{(At critical points)} \\ \text{Generally} \neq \vec{0} & \text{(At all other points)} \end{cases} \tag{26}$$

The difference between the four critical points can be inferred by finding the second derivatives or the Laplacian of the electron density, $\nabla^2\rho(r)$; then verifying if the $\rho(r)$ either rises or falls in each of the three spatial dimensions, **equation 27** provides an overview of this,[124] where λ_i represents the curvatures of all three spatial dimensions.[124]

$$\nabla^2\rho(r) \text{ at BCP} = \lambda_1 + \lambda_2 + \lambda_3 \tag{27}$$

The critical points are then defined with the following characteristics: NCP - where $\rho(r)$ decreases in all three perpendicular directions (3, -3), BCP, ρ(*r*) decreases in two perpendicular directions (3, -1), RCP, $\rho(r)$ decreases in one direction of space; increasing in the remaining two perpendicular to each other (3, +1), $\rho(r)$ is a local minimum and increases in all spatial directions (3, 3+).[3,11] BCPs are of most relevance in this project; they are used to analyse and further quantify the differences in the *cis*- and *trans*-bonding regions in complexes exhibiting the TI and ITI. In this project, two conventional approaches are used to probe the BCPs: assessing the electron density, $\rho(r)$, at the BCP, and assessing the Laplacian of the electron density, $\nabla^2\rho(r)$, at the BCP. We quantify these metrics numerically in the QTAIM analysis (**section 3.3.1**).

The **delocalisation indices**, $\delta(A, B)$, in non-polarised bonds are considered analogous to the classical idea of bond order.[123] It provides a quantitative account of the number of electrons shared between two atoms (A, B) by integrating the electron exchange density of all occupied orbitals within the atomic basins. For a closed-shell system this

can be defined in **equation 28**, where $S_{ij}(\Omega) = S_{ji}(\Omega)$ represent two atomic basins.[123] Similarly, a localisation index $\lambda(A)$, can also be evaluated.[123]

$$\delta(A, B) = -\sum_i \sum_j S_{ij}(A)S_{ji}(B) \tag{28}$$

With *N* being the total number of electrons in the system, QTAIM methodically partitions the molecular space as a sum of the localisation $\lambda(A)$, delocalisation indices, $\delta(A, B)$ to equate to *N*, as shown in **equation 29**.[123]

$$N(A) = \frac{1}{2}\sum_{A \neq B} \delta(A, B) + \lambda(A) \tag{29}$$

BCP and $\delta(A, B)$ metrics both provide detailed information on the bonding between two atomic basins in a QTAIM molecule. Considering a molecular orbital description of the bonding between a metal M and a ligand L, the degree of covalency between two species in a bond can be considered to be proportional to the spatial overlap of the species orbitals, and inversely proportional to their differences in energy.[125–127] Considering this, Kerridge[36] shows that the mixing of a metal-based orbital $\phi_M(\boldsymbol{r})$ and a ligand-based orbital $\phi_L(\boldsymbol{r})$ in a bonding region can be described in terms of a mixing parameter γ, where a large value signifies pronounced covalency.[36] **Equation 30** shows the mixing parameter γ, where H_{ML} is the Hamiltonian matrix element between the two orbitals, and ΔE_{ML} is the energy difference between them.[36]

$$\gamma = \frac{H_{ML}}{\Delta E_{ML}} \tag{30}$$

Equation 30 implies that there are two mechanisms of which the γ value can be large (representing significant bond covalency): energy-driven (small values of ΔE_{ML}), and overlap-driven (large values of H_{ML}); where we would expect only the latter of these types to contribute to the thermodynamic stability of the bonds. Kerridge[36] gives an excellent account of the differences between these covalency types. In terms of QTAIM analysis, only the BCP metrics provide insights to the overlap-driven covalency mechanism, whereas the $\delta(A, B)$ metrics in general characterise *both* overlap-driven and energy-driven covalency.

Describing a molecular system in terms of topological atomic-like regions as a function of the electronic density, $\rho(\boldsymbol{r})$, implies a level of 'fluidity' to the electronic structure. Considering a polarised covalent bonding interaction, typically, involves two atomic regions sharing electron density. In the case of being polar, one of the atomic regions (the more electronegative region) would dominate the shared regions, 'pulling' electronic energy relatively closer to it. As such, ionic species in a molecule will have different formal charges to the same ionic species but in an isolated system. QTAIM skilfully present the atomic charge as a quantum expectation value of an open system.[121] These values are susceptible to change under conditions such as permanent molecular moments or external field polarisation.[121] In a molecular system, the individual QTAIM charges on each atomic partition of the offers an insightful assessment of the overall charge distribution. In conjunction with quantum expectation values for atomic charge, QTAIM also offers similar considerations for atomic volume.[128] Typically, removing electronic energy from an ionic species in a molecule would result in a contraction of the overall atomic basis volume (greater overall nuclear attraction on the valence electrons); ionic partitions gaining electronic energy would result in an increase of atomic volume.[129] Atomic volumes and atomic charges calculated via QTAIM should typically agree.

2.4.2 Natural Bond Orbitals

The natural bond orbital (NBO) approach presents a molecular species as a set of NBOs, completely orthonormal sets of localised, computed bonding-orbitals that can effectively describe any feature of their likened wavefunction, ϕ. NBO starts by assigning a Lewis-like structure to the atomic components in a molecule, and then prescribes integer-restricted bonding-orbitals that typically, are more localised than the canonical s, p, d, and f orbitals.[125] With this, we are able to characterise what type of bonding is present (low s-orbital and highly dominant p-orbital contributions implies π-bonding for example), and of that bonding, what the significant orbital contributions are. In the case of two Lewis structures bonding with each other, NBO provides the percentage that each species contributions into the bond; these are interpretable as degrees of covalency.[125]

Chapter 3

Results & Discussion at the Ground State

3.1 Geometries of the [MOX$_5$]$^-$ Complexes

After defining the model chemistry (basis sets, functionals, dispersion forces), DFT geometry optimisations were conducted for remaining complexes (**II − IX**). **Table 3.1** presents the optimised bond distances for complexes (**I − IX**) as well as crystallographic data bond distances for complexes **II**, **V**, (**VII – IX**). The influence magnitudes in **table 3.1** are calculated using **equation 1**. A reminder that this equation provides a deviation value from an 'idealised' value of 1, (where a value of 1 signifies the *cis-* and *trans-* bond distances are equal). A value **above** 1, shown in TI-exhibiting species, is representative of the *trans*-bond lengths being **greater** than the *cis*-bond lengths (the higher the value, the more significant the length differences are). A value **below** 1, shown in ITI-exhibiting complexes is representative of the *trans*-bond lengths being **shorter** than the *cis*-bond lengths. Applying **equation 1a** to all f-block systems in this project exhibiting an inverse *trans*-influence, molecules **I – III**, as well literary-obtained crystallographic data,[7] the ITI magnitudes typically fall between 0.95 and 0.98. Similarly, applying **equation 1a** to the d-block complexes exhibiting the *trans*-influence, molecules **IV – IX**, as well as their corresponding crystal data,[130–134] yields TI-magnitudes between 1.01 and 1.10.

Table 3.1. DFT- optimised bond distances in the gas-phase are presented in bold. Crystallographic data is presented below the simulated bond distances in italics; previously simulated data is presented in parentheses (for the f-block species, the previously simulated data was obtained from Kaltsoyannis *et al*,[8] using the following model chemistry: 'an uncontracted double-ζ Slater-type orbital valence basis set supplemented with a d-polarisation function- ADF Type III for the halogen and oxygen atoms, as well as a triple-zeta without polarisation- ADF Type IV for the actinide species'[8] + an LDA XC-functional for the DFT calculations[8]).

Complex	$D_{U\text{-}Cl}$ (*cis*) / pm	$D_{U\text{-}Cl}$ (*trans*) / pm	$D_{U\text{-}O}$ / pm	Influence Magnitude
[UOF₅]⁻	**210.45**	**204.07**	**180.97**	**0.970**
	-	-	-	-
	(208.7)	(204.0)	(183.0)	0.977
[UOCl₅]⁻	**257.53**	**251.46**	**177.8**	**0.976**
	253.60	*243.30*	*176.1*	*0.959*
	(253.2)	(249.2)	(179.9)	0.984
[UOBr₅]⁻	**274.16**	**268.58**	**177.35**	**0.980**
	-	-	-	-
	(269.4)	(265.9)	(179.4)	0.987
[MoOF₅]⁻	**185.76**	**194.99**	**178.82**	**1.050**
	-	-	-	-
	-	-	-	-
[MoOCl₅]⁻	**237.46**	**249.38**	**167.74**	**1.050**
	238.78	*264.5*	*165.86*	*1.108*
	-	-	-	-
[MoOBr₅]⁻	**255.19**	**268.35**	**167.33**	**1.052**
	-	-	-	-
	-	-	-	-
[WOF₅]⁻	**190.29**	**198.32**	**172.37**	**1.042**
	-	-	-	-
	-	-	-	-
[WOCl₅]⁻	**237.87**	**250.85**	**170.71**	**1.055**
	231.92	*257.67*	*174.5*	*1.111*
	-	-	-	-
[WOBr₅]⁻	**255.32**	**269.89**	**170.27**	**1.057**
	253.75	*261.00*	*163.00*	*1.029*
	-	-	-	-

3.1.1 Comparing Simulated Complexes to Experimental

Looking first at the f-block [**U**O**X**$_5$]$^-$, complexes; [UO**Cl**$_5$]$^-$, [UO**Br**$_5$]$^-$, [UO**F**$_5$]$^-$: the [UO**Cl**$_5$]$^-$ species was the only structure for which experimental data existed in literature;[7] it was obtained from x-ray crystallography of the solid-state (PPh$_4$)UOCl$_5$ complex.[7] Comparing the simulated data to the experimental for the [UO**Cl**$_5$]$^-$ species, the simulated bond distances were overestimated, the *cis*-distance by 3.93 pm (+1.5% deviation from the experimental) and the *trans*-distance by 8.16 pm (+3.4%). This difference in *cis*- and *trans*-bond ratios for the simulated complexes resultantly manifests as a lesser ITI than that observed experimentally,[7] which is signified by a higher value (closer to 1): 0.976 for the simulated, 0.959 for the experimental. The modelled U-O bond distance of the [UO**Cl**$_5$]$^-$ species however, closely agreed with the experimental, with only a small overestimation of 1.70 pm (deviation of 1.0%). We acknowledge that typically, gas-phase modelling differs from solid-state structures for a number of factors.[8,90,135] Using an LDA functional, Kaltsoyannis *et al*[8] previously simulated the [UO**Cl**$_5$]$^-$ complexes; the data are presented in **table 3.1** in parentheses, along with the details of the model chemistry used. Comparing these data to the experimental provided by Denning,[7] the *cis*-bond distances are well-modelled (underestimating by only 0.40 pm, 0.2%); the axial *trans*-bond distance however, is overestimated (5.90 pm, 2.4%), similar to our simulations. Although the data size is small, it does loosely suggest that the *trans*-bond distance would inherently be over-estimated when modelling the [UO**Cl**$_5$]$^-$ complex.

No experimental data is available for the remaining f-block [UO**X**$_5$]$^-$ complexes (X = F, Br). However, previously simulated data (also from Kaltsoyannis *et al*[8]) can be used for comparison, and are shown in parentheses in **table 3.1**. Considering the [UO**F**$_5$]$^-$ complex, overall, the bond distances are similar, our *cis*-bond distances were 1.75 pm less than those in ref 8[8] (-0.8%) and the *trans*-bond distances only 0.07 pm less (0.03%), this slight difference yields an ITI value of 0.977 for our complexes, just slightly higher (therefore lower in ITI magnitude) than Kaltsoyannis' 0.970.[8] Similar observations are made when comparing the [UO**Br**$_5$]$^-$ and [UO**Cl**$_5$]$^-$ complexes to previously simulated data,[8] overall our data appear to mostly underestimate bond distances. The differences between our simulations and previous work[8] are accounted due to different model

chemistries being used, qualitatively however, they demonstrate a generally similar difference in the *cis-* and *trans-*bonds distances, where the latter is modelled to be **shorter**; overall, manifesting as similar ITIs.

Experimental data for d-block species $[MoOX_5]^-$ and $[WOX_5]^-$ (X = F, Cl, Br) is only available for the $[WOX_5]^-$ (X = Cl,[131,132,136] Br[130]) and $[MoOCl_5]^-$ complexes, they are represented in italics in **table 3.1**. For the $[\mathbf{W}OX_5]^-$ complexes, the experimental $[\mathbf{W}O\mathbf{Cl}_5]^-$ bond distances given in **table 3.1** are an average of three separately sourced crystallographic bond distances;[131,132,136] compared to experimental, our gas-phase simulated $[\mathbf{W}O\mathbf{Cl}_5]^-$ complex gave a greater *cis-*bond distance (5.95 pm, +2.57%), a shorter *trans-*bond distance (6.82 pm, -2.65%) and a shorter W-O distance (3.79 pm, 2.18%), resultantly affording a notably lower TI (1.111 crystal, 1.055 simulated), indicative of a lower magnitude. The *cis-*bond distances for the gas-phase $[\mathbf{W}O\mathbf{Br}_5]^-$ complex generally agree with the experimentally resolved data[130] (overestimating by only 1.57 pm, 0.62%). The W-O bond distance, however, was overestimated by a larger amount (7.27 pm, 4.46%); the *trans-*bond distance by an even greater amount (8.89 pm, 3.40%). This manifested as a **greater** TI value than the crystal data (1.029 crystal, 1.057 simulated).

Considering the $[\mathbf{Mo}OX_5]^-$ complexes, for the $[MoO\mathbf{F}_5]^-$ species, the gas-modelled *cis-*bond distances mostly agreed with crystal bond distances (underestimating by only 1.32 pm, −0.56%), the Mo-O bond distance was underestimated by 1.88 pm (−1.12%); the *trans-*bond distance was greatly underestimated (15.12 pm, −5.72%). Typically, when modelling these d-block complexes in the gas-phase, it appears that the *trans-*bond distance shows the most deviation (relative to other bond distances) to the experimentally resolved data.

3.1.2 Comparing the f- and d-block Optimised Bond Lengths

Comparing the influence magnitudes of the two d-block metals (Mo and W) and their respective halogens: For X = Cl, and Br, the [**W**OX$_5$]⁻ complexes have greater TIs than the [**Mo**OX$_5$]⁻ complexes, for X = F however, the [**Mo**OF$_5$]⁻ complex has a greater TI than the [**W**OF$_5$]⁻ complex. Comparing the ITI and TI, understanding the influence magnitudes as deviations from an idealised value of 1, we see that for the X = F complexes, the deviations (difference between *cis*- and *trans*-bond lengths) are greatest in the [**Mo**OF$_5$]⁻ species, followed by the [**W**OF$_5$]⁻ species, and then [**U**OF$_5$]⁻ with the lowest, suggesting that irrespective of a formal TI or ITI definition, the magnitudes of the influences are greatest in the [**Mo**OF$_5$]⁻ followed by the [**W**OF$_5$]⁻ and then the [**U**OF$_5$]⁻ species. Following suit, for the X = Cl complexes, the difference between the *cis*- and *trans*-bonds is again greatest in the [**W**OCl$_5$]⁻ complexes, followed by the [**Mo**OCl$_5$]⁻ variants, and then the [**U**OCl$_5$]⁻ complexes. The same trend is shown for the X = Br complexes, [**W**OBr$_5$]⁻ with the greatest deviation, then [**Mo**OBr$_5$]⁻ and then [**U**OBr$_5$]⁻ with the least. Conclusively, for all halogen derivatives, the TI in the d-block species has a greater magnitude than the ITI in the f-block species;

3.1.3 ITI and TI as a function of Ligand X

For the f-block [**U**OX$_5$]⁻ species, the *trans*-bonds are 3.03%, 2.36%, and 2.03% **shorter** than the *cis*-bonds for the F, Cl, and Br complexes respectively (with ITIs of 0.970, 0.977, and 0.984, **table 3.1**). This tells us that in the U-based complexes, the ITI is greatest in the F species, followed by the Cl and then the Br, with the lowest ITI. For the d-block [**Mo**OX$_5$]⁻ species, the *trans*-bonds are 4.97%, 5.02%, and 5.16% **longer** than the *cis*-bonds for the F, Cl, and Br complexes respectively (with TIs of 1.050, 1.042, and 1.055, **table 3.1**). Therefore, in the [**Mo**OX$_5$]⁻ complexes, the TI is greatest in the Br species, followed by the F and then the Cl, with the lowest TI magnitude. For the [**W**OX$_5$]⁻ species, the *trans*-bonds are 4.22%, 5.45%, and 5.70% **longer** than the *cis*-bonds for the F, Cl, and Br derivatives respectively (TIs of 1.042, 1.055, and 1.057, **table 3.1**). Therefore, in the [**W**OX$_5$]⁻ species, opposite to the halogens ITI trend in the [**U**OX$_5$]⁻ species, the TI is greatest in the Br species, followed by the Cl, and then the F species with the lowest TI magnitude. To summarise, when comparing the [MOX$_5$]⁻

species as a function of halogen X, the order for increasing influence magnitude goes F > Cl > Br for the [**UOCl$_5$**]$^-$ complex (agreeing with previous literature[8]), Br > F > Cl for the [**MoOCl$_5$**]$^-$ complexes, and Br > Cl > F for the [**WOCl$_5$**]$^-$ complex.

The differences amongst the halogen ligands could superficially be accounted for by the intrinsic properties of the X ligands such as the increasing van der Waal radii of the species (147, 175, 185 pm for F, Cl, and Br respectively)[137] causing greater repulsion, directly influencing the *cis-* and *trans-*bond ratios. Or the difference in electronegativities (decreasing going down group 17) reflecting a change in metal-ligand covalency.[8] Typically, a larger species of ligand would imply less defined p$_x$ and p$_y$ orbitals to participate in *pseudo-*π-bonding for the equatorial ligands (pseudo as the halogen-metal bonds are typically considered to be singly bonded); additionally, the larger ligand radii could infer that steric interactions/repulsions may occur more prominently. Concerning the f-block species, Kaltsoyannis[8] *et al* suggest that the lower ITI magnitude of the bromine-type, (relative to the chlorine and fluorine) could be a result of weaker π-bonding between the *cis-*halogens and the metal,[8] or a stronger σ-bond between the *trans-*halogen and the metal,[8] or both.

However, as the d-block and f-block complexes have the opposite trends upon increasing halogen number, this suggests that the difference is not necessarily an intrinsic property of the ligands, but of the different interactions the metals have with the ligands. To clarify this, increasing the halogen number results in the ITI decreasing (*cis-*bonds decrease, *trans-*bonds increase), and the TI increasing (also, *cis-*bonds decrease, *trans-*bonds increase). i.e. the same effects concerning the *cis-* and *trans-*bonds are seen for the f- and d-block species when increasing the halogen number, it simply manifests differently in terms of the ITI and TI.

Concerning the [UOX$_5$]$^-$ species, Kaltsoyannis *et al*[8] have previously identified the presence of a U-X$_{trans}$ antibonding orbital that is highly present in the bonding characterisation of the bromine species, and decreases in presence when moving up the halogen group (Cl, F). They also report a U-X$_{cis}$ antibonding molecular orbital that follows the opposite trend, prominent in the fluorine species, but less so in the bromine. Interpretably, this would decrease the M-X$_{trans}$ distance whilst increasing a M-X$_{cis}$

distance moving from the fluorine to the bromine species. The ideal situation would be if the opposite is apparent in the d-block complexes, a closer consideration of molecular orbitals is considered in this project.

3.1.4 ITI and TI as a Function of the M-O Bond

A key aspect of the ITI and TIs that is highlighted in **table 3.1**, is that its magnitude directly correlates with the M-O bond distance. As shown, any complex exhibiting a greater ITI/TI (greater deviation from and influence value of 1) is accompanied by a shorter M-O bond distance. For example, in the [WO**Cl**$_5$]⁻ complex, the W-O bond distance is 170.71 pm and has a *trans*-influence of 1.055. Whereas the [WO**F**$_5$]⁻ complex has a greater W-O bond distance (172.37 pm) with a relatively lower *trans*-influence of 1.042. This implies that the σ-donor (O ligand) distance is relatable to the influence magnitudes (irrespective of being the ITI or TI). This can be justified using Denning's perturbation model.[7] As previously detailed in **section 1.3.**4, the model describes the TI/ITI in terms of a core-polarisation induced by a strong σ-donor, the result of which causes a dipolar (TI) or quadrupolar (ITI) effect, depending on the relative parities of the HOMO and LUMO orbitals.[2] Within this framework, one can assume that the closer the anionic ligand is to the metal, the greater the degree of core-polarisation (manifesting as a greater degree of ITI/TI appropriately). Lam *et al*[14] report this polarisation effect in imide complexes where the strongly anionic ligand is a nitrogen atom.[14] Using the optimised bond distances from seven different XC-functionals (see **section 2.2.3**, **table 2.3**), a qualitative plot of the U-O bond distance against the influence percentage was made. This is shown for both the [UOCl$_5$]⁻ and the [MoOCl$_5$]⁻ complexes in **figures 3.1** and **3.2** respectively.
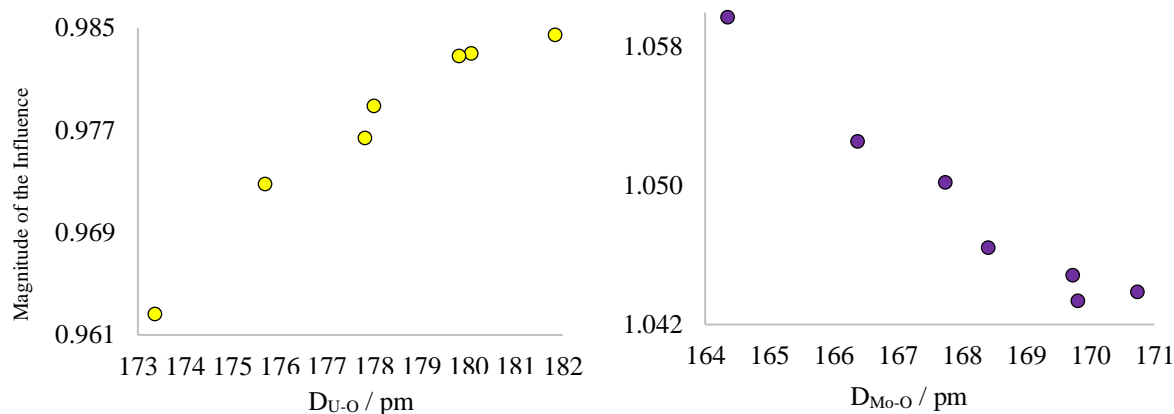
Figures 3.1 (left) and 3.2 (right). An illustrative plot comparing the influence magnitude (%) against M-O bond distance pm for [UOCl$_5$]$^-$ (left) and [MoOCl$_5$]$^-$ (right). Data were obtained from seven different functionals (PBE0, PBE, B3LYP, BHLYP, TPSS, TPSSH, BLYP, see **section 2.2.3** for further details)

Figures 3.1 and **3.2** illustrate how the ITI and TI depend on the distance of the O-ligand from the metal centre. For the ITI (**figure 3.1**), increasing the U-O bond distance increases the ITI value (representative of the *cis-* and *trans*-bonds become more 'like'), signifying a decrease in the ITI. For the TI, (**figure 3.2**), increasing the Mo-O bond distance decreases the TI value. In both cases, it is a result of the *trans/cis*-bond distances likening to each other. This was further tested by 'freezing' the M-O bond length at various distances and allowing the remainder of the structure to relax. For example, the [UOCl$_5$]$^-$ complex, the U-O bond distance was incremented between 170.0 pm and 190.0 pm, in increments of 1.0 pm; the same procedure was carried out for the [MoOCl$_5$]$^-$ under the same constraints (in this case however the Mo-O bond distance ranged from 162 – 178 pm). Each calculation was performed with the B3LYP XC-functional. Both the *cis-* and *trans*-bond distances obtained are plotted against the increasing M-O bond distance, as well as the influence magnitudes as shown in **figures 3.4** and **3.5** for [UOCl$_5$]$^-$ and [MoOCl$_5$]$^-$ respectively.
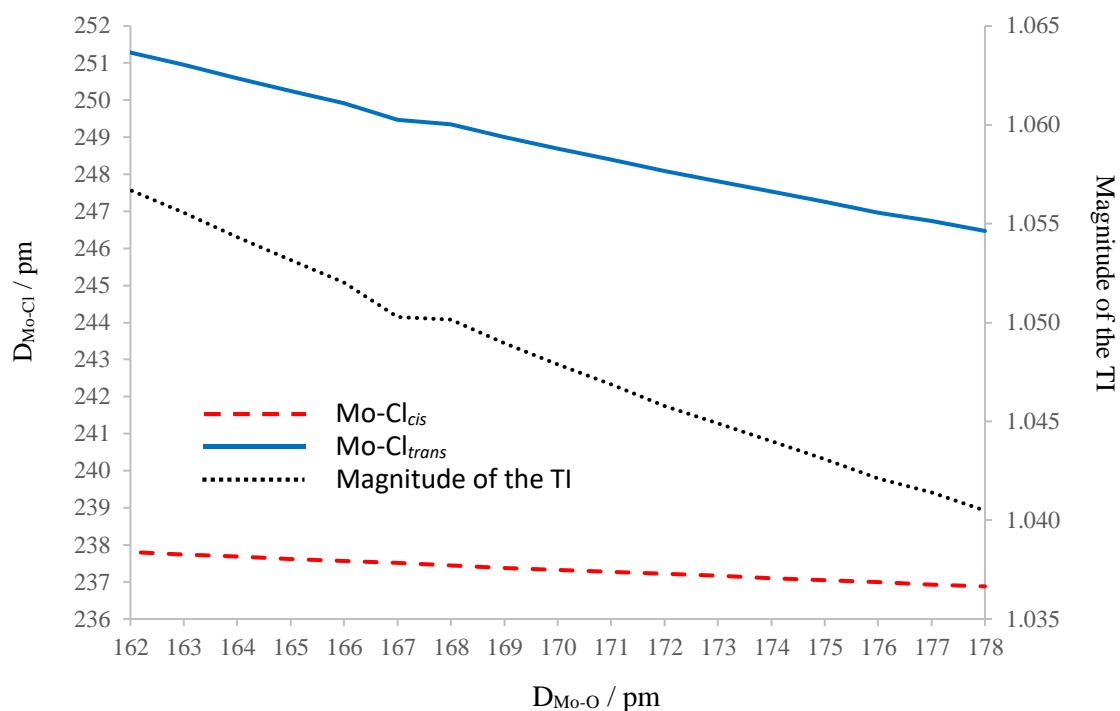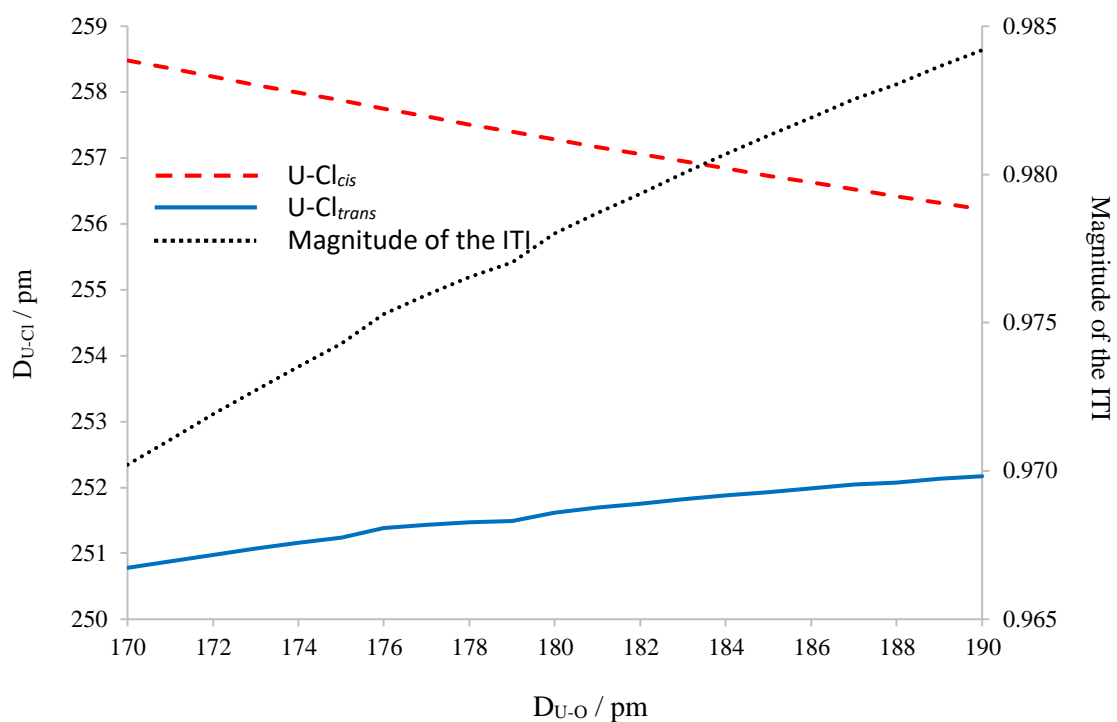
Figures 3.4 (top) + **3.5** (bottom). Plot of the [UOCl₅]⁻ (top, **fig. 3.4**) and the [MoOCl₅]⁻ (bottom, **fig, 3.5**) complexes showing the D_{M-Cl} (*cis*) and D_{M-Cl} (*trans*) bond distances pm vary against an increasing D_{M-O} bond distance pm. In addition, the ITI and TI magnitude values are plotted.

Figure 3.4 qualitatively confirms that the ITI decreases (increasing magnitude value) with increasing U-O bond distance, the ITI being a result of *cis-bond* elongation and *trans*-bond contraction.[8] Interestingly, **figure 3.4** also seems to illustrates that the shortening the U-O distance (increasing the ITI), causes the *cis*-bond distances **increase** more rapidly than the *trans*-bonds **decrease**. This seems to imply that the ITI is more a result of a *cis*-bond elongation, than a *trans*-bond contraction. However, considering the steric effects of moving the O-ligand closer to the equatorial *cis*-ligands, this would probably be expected. **Figure 3.5** shows how the TI decreases with decreasing Mo-O bond distance. Differently to **figure 3.4** however, **figure 3.5** shows how the TI appears to be mostly a result of a *trans*-bond elongation rather than a *cis*-bond contraction. In fact, the slight increase of the *cis*-bond distances could be accounted for simply by the steric interactions from the nearing O-ligand; in which case this would provide further evidence for the *cis*-bond elongation in the ITI (**figure 3.4**) being the dominant contribution to the inverse *trans*-influence. To summarise, the TI in the d-block species is mainly a result of the *trans*-bond increasing relative to the *cis*-bonds. The ITI contrarily is a result of both the *cis*- and *trans*-bond distances increasing, with the former being most pronounced.

3.2 Geometries of the MX$_6$ Complexes

Previous work[138] that pertains to the DFT-characterisation of the ITI/TI in [MOX$_5$]$^-$ (M = U, Mo and X = Cl, Br) complexes, provide an illustration of the descension of symmetry from an O$_h$ (each molecules MX$_6$ structural analogous) to C$_{4v}$ (the [MOX$_5$]$^-$ complexes). Similarly, in this project, the MX$_6$ equivalents to **molecules I – IX** are characterised by DFT simulations using the exact same methodology provided in previous sections, illustrations of these complexes are shown in **figure 3.5** (**molecules X – XVIII**).

All MX$_6$ complexes were modelled using the exact same model chemistry described in previous sections, they possess 0$_h$ symmetry; octahedral geometry and have a formal oxidation state of (IV) for their metal species, with zero unpaired electrons. The purpose of simulating the MX$_6$ species (**figure 5a**, **molecules X – XVIII**) was to provide 'standardised' bond lengths of which the [MOX$_5$]$^-$ complexes could be compared too. Analysing both structure sets in this fashion would provide an insight as to how far the *cis*/*trans*-bond lengths of the [MOX$_5$]$^-$ deviate from the 'normal' MX$_6$ bond lengths. **Table 3.2** shows bond length data for the optimised molecules (**X – XVIII**), as well as the bond lengths of the previously optimised [MOX$_5$]$^-$ complexes (**I – IX,** first presented in **table 3.1**).
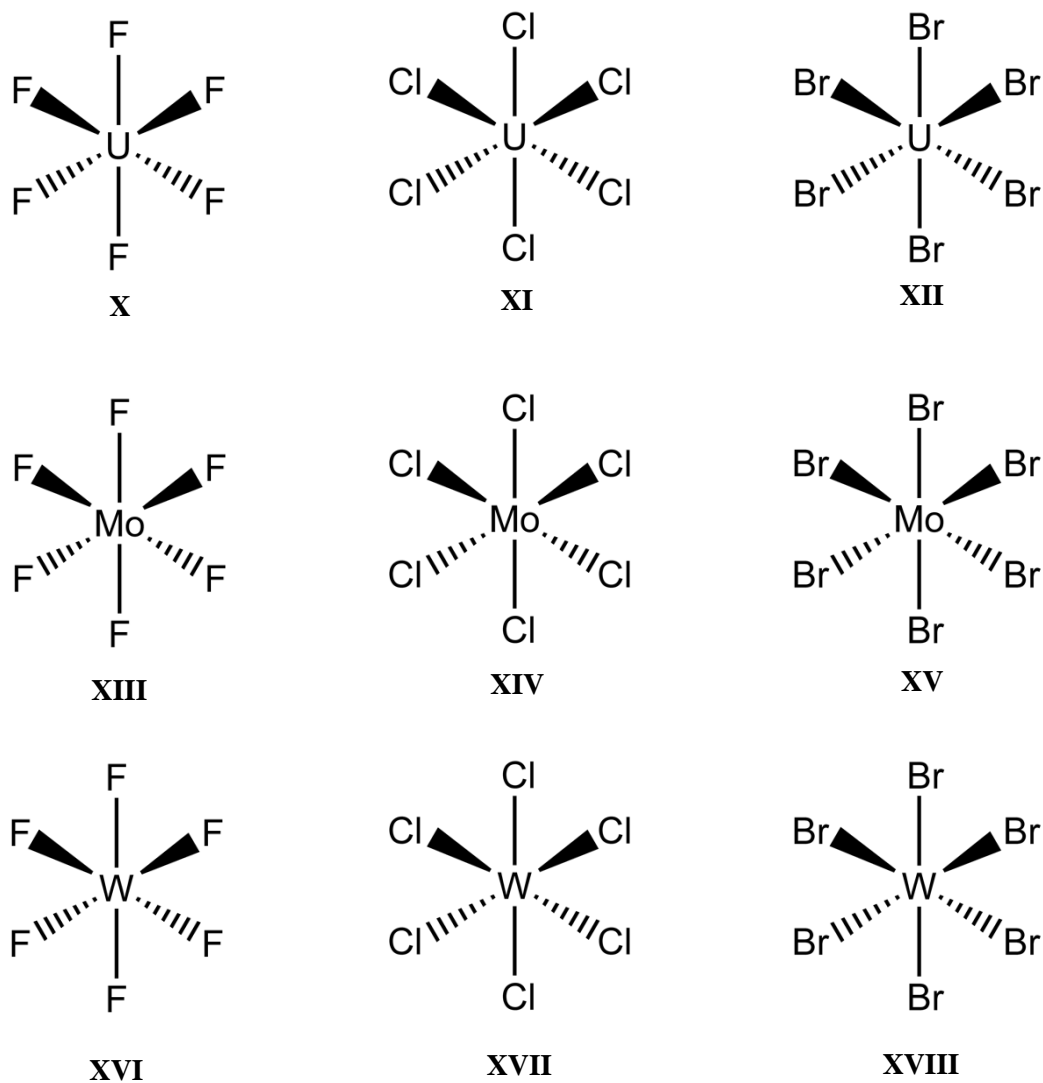
Figure 3.5. an illustration of the MX_6 complexes. The top row, in left-to-right order shows complexes **X**, **XI** and **XII** ([UF$_6$], [UCl$_6$], and [UBr$_6$] respectively). The middle row shows complexes **XIII**, **XIV** and **XV** ([MoF$_6$], [MoCl$_6$], and [MoBr$_6$]). The bottom row shows complexes **XVI**, **XVII** and **XVIII** ([WF$_6$], [WCl$_6$], and [WBr$_6$]).

Table 3.2. The geometrically optimised bond distances, D, for the MX$_6$ complexes (**molecules X – XVIII**) are presented in bold. The corresponding [MOX$_5$]$^-$ bond distances, D, both *cis-* and *trans*-bonds are also presented, where the former are shown italicised (this ordering is demonstrated in the top left box).

M(VI)	D$_{M-F}$ / pm	D$_{M-Cl}$ / pm	D$_{M-Br}$ / pm
UX$_6$	**200.75**	**247.27**	**264.10**
cis - [**UOX$_5$**]$^-$	*210.45*	*257.53*	*274.16*
trans - [**UOX$_5$**]$^-$	204.07	251.46	268.58
	183.34	**231.36**	**249.86**
Mo	*185.76*	*237.46*	*255.19*
	194.99	249.38	268.35
	185.29	**232.34**	**250.52**
W	*190.29*	*237.87*	*255.32*
	198.32	250.85	269.89

3.2.1 Comparing Bond Lengths of the MX$_6$ and the [MOX$_5$]$^-$ Complexes

Definitively, all bond lengths of the [MOX$_5$]$^-$ species are greater than the corresponding MX$_6$ species. This seems reasonable as we would typically expect the steric effects of an O ligand to cause a 'total expansion' of the molecule; in addition, the electronic consequences of including a highly electronegative O species, as well as the [MOX$_5$]$^-$ being singularly anionic compared to the neutral MX$_6$ structures would no doubt cause differences.

Considering just the f-block complexes: modelling the [UOX$_5$]$^-$ complexes as a deviation from their UX$_6$ counterparts, there is a *cis*-bond lengthening of 9.70 pm (increased by 4.8% from the UX$_6$ complex), 10.26 pm (4.2%) and 10.06 pm (3.8%) respectively for X = F, Cl, Br; correspondingly, there is *trans*-bond lengthening of 3.32 pm, 4.19 pm, and 4.48 pm (all with a percentage increase of 1.7%) in the same order. We would generally expect different halogens to give different bond distances on account of their different ionic size and chemistries, and looking at the percentage differences this *appears* to be the case, however, in upon closer inspection, it seems that the *cis*-bonds of the [UOX$_5$]$^-$ complexes all increase by a uniform distance of 10 pm, irrespective of the halogen substituent. The *trans*-bond expansions appear uniformly correlated with increasing halogen size, in the order of F < Cl < Br (ionic radii: 119 pm, 167 pm, and 182 pm for the F, Cl, and Br respectively[139]).

Considering the d-block complexes: comparing the [**Mo**OX$_5$]$^-$ species to their corresponding **Mo**X$_6$ counterparts, in the same order of increasing halogen number (F, Cl, Br), there is a *cis*-bond lengthening of 2.42 pm (1.3%), 6.10 pm (2.6%) and 5.33 pm (2.1%); correspondingly, there is *trans*-bond lengthening of 11.65 pm (6.4%), 18.02 pm (7.8%) and 18.49 pm (7.4%) in the same order. The data for the Mo-Cl and Mo-Br complexes generally agree, the Cl-type causing a slightly greater degree of total bond expansion. The order for increasing deviations for both *cis-* and *trans*-bonds goes Cl > Br > F. Comparing the [**W**OX$_5$]$^-$ complexes to their corresponding **W**X$_6$ counterparts, in the same order of increasing halogen number (F, Cl, Br): there is a *cis*-bond lengthening of 5.00 pm (2.7%), 5.53 pm (2.4%) and 4.80 pm (1.9%); correspondingly, there is *trans*-bond lengthening of 13.03 pm (7.0%), 18.51 pm (8.0%) and 19.37 pm (7.7%) in the same order. The order for increasing deviations (concerning the *cis*-bonds) is F > Cl > Br; interestingly the order for increasing deviations (concerning the *trans*-bonds is the opposite: Cl > Br > F.

3.3 QTAIM Analysis

Up until this point, the discussion of the ITI and TI in the $[MOX_5]^-$ systems has considered optimised bond distances. In this section, a topological discussion of the electron density ρ, using QTAIM methodologies is presented; within this, the intrinsic electronic properties of the *trans-* and inverse *trans*-influences, as a function of the cationic-centre and ligand-type are discussed. We focus specifically on bond critical points (electron density ρ_b, and the Laplacian of the electron density $\nabla^2\rho_b$), and delocalisation indices, $\delta(X,Y)$, we also briefly discuss other integrated metrics including atomic charges q, and atomic volumes v_x.

As previously described in **section 2.4.1** (in particular, **equation 30**), covalency has two mechanisms: overlap-driven and energy-driven. Overlap-driven covalency, measured exclusively using BCP metrics, manifests from the near-degeneracy of atomic wavefunctions, and is a measure of the charge accumulation at the BCP. Energy-driven covalency, on the other hand, manifests from the near-degeneracy of energy levels, it is measured in this project using $\delta(X,Y)$ values, although it should be noted that these values typically measure both types of covalency; therefore, $\delta(X,Y)$ values can be large even with low charge accumulation at the BCP (absence of significant overlap-driven covalency). Of the two covalency types, we would only expect overlap-driven to stabilise the bonding interaction thermodynamically.[36]

For each $[MOX_5]^-$ complex, the topological analysis for its corresponding MX_6 complex will also be provided; the MX_6 data itself will come in two forms: The first form, the MX_6 complexes are geometrically optimised in the same fashion as the $[MOX_5]^-$ complexes in previous sections (the bond lengths are provided in **table 3.2**). The second form, the MX_6 complexes are geometrically-constrained, where each of the M-X bond distances is 'fixed' to the M-X$_{cis}$ bond distance of the corresponding $[MOX_5]^-$ complex. When referring to the bond constrained MX_6 complexes, we differentiate with an asterisk preceding it (e.g. *MX_6).

3.3.1 Bond Critical Points

We first turn our attention to the BCP metrics that typically, are concerned with overlap-driven covalency. BCPs can be probed to obtain values for the electron density at the BCP, ρ_b, and the Laplacian of the electron density at the BCP, $\nabla^2\rho_b$, the latter of which provides insights to the degree of charge depletion at the BCP.[3,94,140] Zhang *et al*[141] propose the following descriptive framework: large values of ρ_b (typically > 0.2 au) and large negative values of $\nabla^2\rho_b$ characterise conventionally covalent bonds, whereas small values of ρ_b (typically < 0.1 au) and large positive values of $\nabla^2\rho_b$ more appropriately characterise closed-shell interactions such as ionic, hydrogen, σ-hole halogen or van der waal bonding.[94] Considering the Laplacian of the electron density, $\nabla^2\rho_b$, a large positive value is characteristic of a charge depletion at the BCP, which implies a predominantly ionic interaction, whereas a negative value implies a charge accumulation at the BCP, indicative of covalent bonding.[94] For example, a conventionally covalent species such as H_2 has a ρ_b of 0.27 au and a $\nabla^2\rho_b$ value of −1.39 au.[141] Whereas a typically more ionically-bonded diatomic such as LiF has a ρ_b of 0.07 au and a $\nabla^2\rho_b$ value of +0.62 au.[141] **Table 3.3** presents the BCP data for the f-block $[UOX_5]^-$ complexes (X = F, Cl, Br) as well as their corresponding UX_6 counterparts (both optimised and constrained).

Table 3.3. QTAIM data concerning BCP metrics of the $[UOX_5]^-$ complexes, as well as their UX_6 counterparts (both optimised and *constrained). The value of the electron density at each BCP ρ_b is provided, along with the value of the Laplacian of the density, $\nabla^2\rho_b$, (of which is presented below in italics). All data is in atomic units au

X	Bond Critical Point (BCP)				
		$[UOX_5]^-$		$*[UX_6]$	$[UX_6]$
	U-O	**U-X**$_{cis}$	**U-X**$_{trans}$	***U-X**	**U-X**
F ρ_b	0.282	0.122	0.142	0.127	0.156
$\nabla^2\rho_b$	*0.302*	*0.430*	*0.417*	*0.379*	*0.459*
Cl ρ_b	0.301	0.080	0.095	0.083	0.099
$\nabla^2\rho_b$	*0.311*	*0.140*	*0.120*	*0.118*	*0.146*
Br ρ_b	0.306	0.068	0.078	0.071	0.084
$\nabla^2\rho_b$	*0.318*	*0.093*	*0.076*	*0.078*	*0.096*

The ρ_b values of the U-X bonds in the [UOX$_5$]$^-$ species (where X = Cl and Br) are less than 0.1 au, whereas in the [UOF$_5$]$^-$ species, the ρ_b values fall between 0.1 and 0.2 au. Applying the outlined framework[141] for relating ρ_b to bond characterisation, the [UOF$_5$]$^-$ have a higher degree of covalency in the U-X bonds relative to the [UOCl$_5$]$^-$ and [UOBr$_5$]$^-$ complexes (both of which would typically be considered to bond ionically considering their ρ_b values are < 0.1 au). Of the [UOBr$_5$]$^-$ and [UOCl$_5$]$^-$ complexes, the ρ_b values show that the U-Br bonding shows a slightly lower degree of covalency (more ionic) than the U-Cl bonds (both *cis-* and *trans-*). To quantify, in the [UOBr$_5$]$^-$ complex, the U-Br bonds have ρ_b values of 0.068 au and 0.078 au for the *cis-* and *trans-*bonds respectively. In the [UOCl$_5$]$^-$ complex, the U-Cl bonds have ρ_b values of 0.080 au and 0.095 au (which is 17.6% and 21.8% greater than the U-Br bonds). In the [UOF$_5$]$^-$ complex, the U-F bonds have ρ_b values of 0.122 and 0.142 (52.5% and 49.5% higher than the U-Cl bonds). Overall, on account of the ρ_b values, the order for increasing covalency goes F >> Cl > Br, where the Cl and Br are fairly similar. The same trend in bond covalency is shown in the UX$_6$ complexes (both optimised and constrained), where the U-F bonds in the UF$_6$ species have the highest ρ_b followed by the U-Cl and then the U-Br (from the UCl$_6$ and UBr$_6$ species respectively); this implies the high ρ_b values are intrinsic to the F-ligand. Furthermore, experimental studies[142] pertaining to the U-F bonds in hexafluoride (UF$_6$) complexes have validated the higher orders of covalency in the U-F bonds.

We can justify the F-ligands increased affinity to bond covalently by considering a hard and soft Lewis acids and bases (HSAB) approach. First introduced by Pearson,[143] HSAB theory is a quantitative predictive model that can be can be used to assess the strength of an interaction between two species. It does this by classifying each species in an interaction (also called a Lewis adduct in HSAB) as either a Lewis acid or base, with assigned levels of 'hardness' or 'softness' based on a multitude of parameters. Lewis acids are defined as electron pair acceptors, and Lewis bases, electron pair donors.[144,145] The criteria for a typical hard species includes high electronegativity, small ionic radii and weak polarizability. The criteria for a soft species is predictably the opposite, lower electronegativity, expanded ionic radii, and more substantial polarizability.[129,146] Under this framework, the rules then state that soft bases will bond more favourably with soft acids, and hard bases will bond favourable with hard acids.[129]

Applying the HSAB model to our molecular systems, the U(VI) species would be considered a **hard** Lewis acid, on account of its small ionic radius and low polarizability; the halogen species, would be the Lewis bases. The fluorine, with a relatively small ionic radius (119 pm)[139] and high electronegativity would typically be described as the hardest, followed by chlorine (167 pm),[139] and then bromine (182 pm)[139] as the softest. Considering this, it seems expected that the F-ligands, being the hardest would bond most effectively with the hard U(VI) species, followed by the Cl-ligands, and then the Br-ligands, which being the softest, would bond the least efficiently (manifesting as decreased bond covalency).

As a brief side note, the ionic radii quoted are obtained from crystal data.[139] A key feature of QTAIM, is that atomic species are not conventionally spherical in molecules; therefore an ionic radius cannot be defined so easily. However, integrated QTAIM atomic volumes can be obtained, and are presented in **table 3.4.** Ultimately, we see that the QTAIM atomic volumes v_x scale similarly to the crystal-obtained ionic radii,[139] with the F-species (atomic radii: 147 pm) exhibiting the smallest QTAIM volume v_x in both the *cis-* and *trans*-positions (129.2 au, and 123.0 au respectively), followed by the Cl (atomic radii: 175 pm, v_x = 245.5 au, and 234.0 au) and then the Br (atomic radii: 185 pm, v_x = 298.6 au, and 287.2 au). The trend in ionic radii q and QTAIM integrated volumes v_x (**table 3.4**) appears to match that of the trend in bond covalency, defined by the ρ_b values (**table 3.3**), where the difference between the [UO**Br**$_5$]$^-$ and [UO**Cl**$_5$]$^-$ is small but [UO**Cl**$_5$]$^-$ and [UO**f$_5$**]$^-$ is significant.

Figure 3.6 shows a plot of the ρ_b and of $\nabla^2\rho_b$ values for the U-X bonds in the [UOX$_5$]$^-$ complexes (both *cis-* and *trans-*), as well as the U-X bonds in the UX$_6$ complexes (optimised and constrained) against their respective bond lengths (bond length data is taken from **tables 3.1** and **3.2**). With the exception of the U-O bonds, **figure 3.6** shows that the ρ_b values appear to scale inversely to bond lengths, which has been previously reported in literature.[147] For example, the bond lengths of the optimised U-X bonds are all around 10 pm **less** than the corresponding constrained *U-X bonds, and correspondingly, the ρ_b values of the U-X bonds are **greater** than the *U-X bonds. In addition, we see that the *cis*-bonds in all [UOX$_5$]$^-$ complexes, which are characteristically **greater** than the *trans*-bonds (in accordance to the ITI), all have

relatively **lower** ρ_b values. This trend is broken however when comparing the constrained U-X bonds to the U-X$_{cis}$ bonds (from the [UOX$_5$]$^-$ complexes), where despite having the same bond lengths, the constrained *U-X bonds have slightly higher ρ_b values than the U-X$_{cis}$ bonds. Therefore we conject that although ρ_b values *mostly* scale inversely with bond length,[147] there must also be other determining factors that come into play.

Table 3.4. For each atomic partition in the [UOX$_5$]$^-$ complexes (M = U, Mo, W and X = F, Cl, Br), the integrated QTAIM data concerning the atomic charges q (au) and volumes v_x (au) are shown (the latter is shown in italics). The atomic charges of a species can provide indications of bonding character, with decreased charge (and charge separation) associated with covalency.[125] The QTAIM atomic volumes are correlated with the atomic charges, where due to the differing nuclear charge felt by the valence electrons, a decrease in the atomic charge causes a volume contraction, and an increase in charge causes a volume expansion.[35]

| M	X	[MOX$_5$]$^-$			
		O	M	X$_{cis}$	X$_{trans}$
	F	−0.87	+3.33	−0.70	−0.65
		137.2	*97.1*	*129.2*	*123.0*
U	Cl	−0.84	+2.78	−0.60	−0.51
		130.4	*108.6*	*245.5*	*234.0*
	Br	−0.84	+2.58	−0.56	−0.48
		129.3	*117.6*	*298.6*	*287.2*
	F	−0.79	+3.14	−0.66	−0.72
		133.0	*56.6*	*118.7*	*124.3*
Mo	Cl	−0.68	+2.45	−0.51	−0.74
		123.0	*71.3*	*228.6*	*250.9*
	Br	−0.69	+2.19	−0.47	−0.64
		123.2	*80.5*	*281.0*	*293.9*
	F	−0.94	+3.46	−0.69	−0.75
		136.7	*58.0*	*119.4*	*124.7*
W	Cl	−0.82	+3.46	−0.56	−0.69
		128.3	*72.7*	*230.9*	*244.9*
	Br	−0.81	+2.46	−0.50	−0.67
		127.1	*81.8*	*281.1*	*295.3*
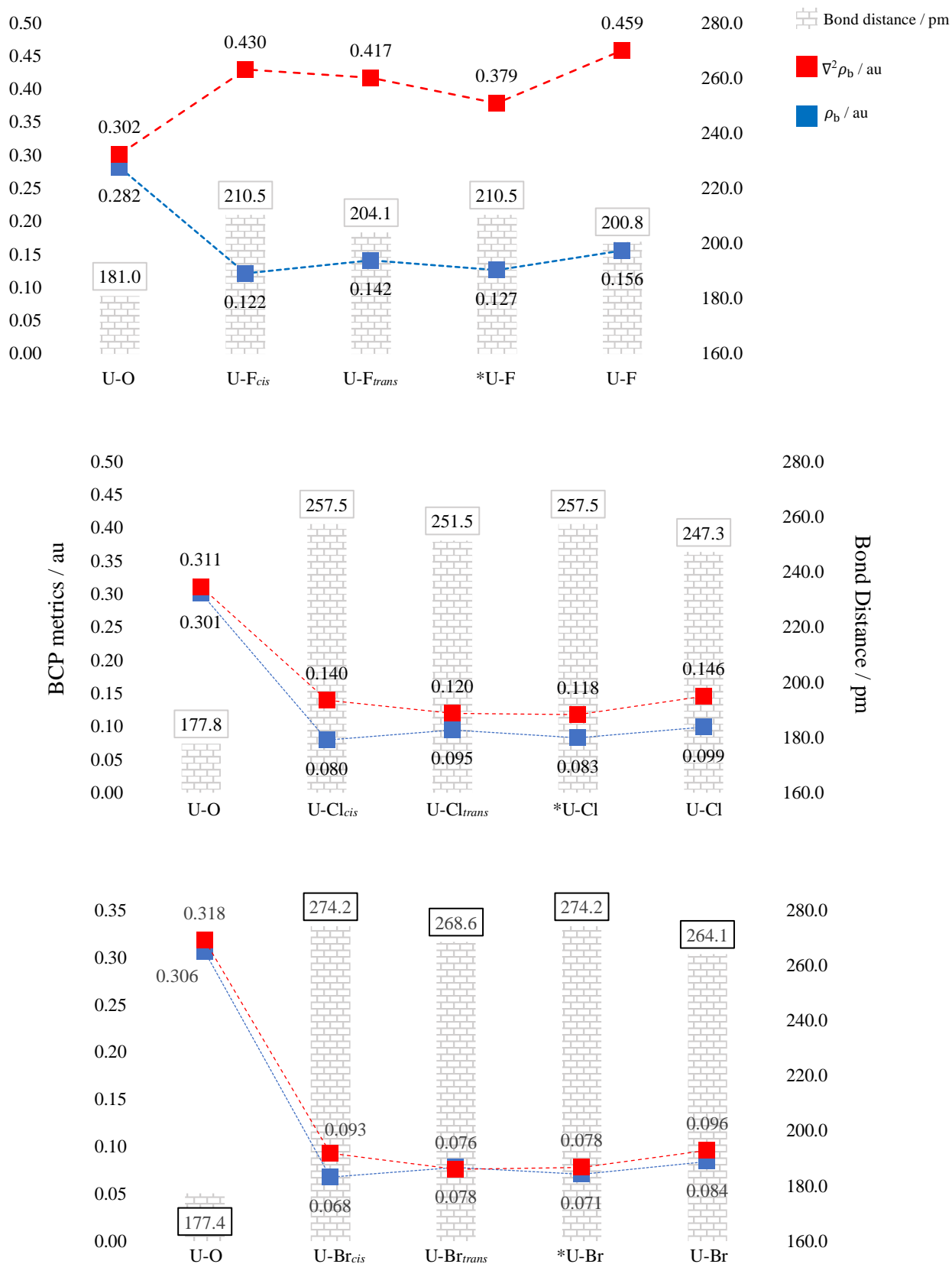
Figure 3.6. plots of the ρ_b, $\nabla^2\rho_b$ values, au, (left axis) and bond lengths, pm, (right axis) for the [UOX$_5$]$^-$ bonds (*cis*- and *trans*- and U-O). The optimised UX$_6$ bonds, and the constrained *UX$_6$ bonds are also provided. X = F in the top graph (**3.6a**), Cl in the middle graph (**3.6b**) and Br in the bottom graph (**3.6c**)

Considering the $\nabla^2\rho_b$ values, under the quantitative framework first outlined,[141] the large positive values of $\nabla^2\rho_b$ (for both the *cis- and trans-*bonds in the f-block complexes) suggests that the f-block complexes predominantly show conventionally ionic bonding; the $[UOF_5]^-$ species exhibiting the highest level of ionic bonding in the U-F bonds, disagreeing with the ρ_b metrics. Zhang *et al*[141] report a similar puzzlement over a homonuclear, and traditionally covalently-bonded fluorine species (F_2), observing high ρ_b and large positive $\nabla^2\rho_b$ values that typically don't agree with the covalency criteria (or even ionic bonding).[141] Berryman *et al*[125] provide elucidation on this matter however, by considering formally covalent-driven M-O bonds (where M = Ti, Hf, Th, Zr, Ce, and U), they notice that the Laplacian values, $\nabla^2\rho_b$, are far more positive than expected, similar to what we are seeing. They rationalise this anomaly as a consequence of the high polarisation of the M-O bonds; furthermore, they conject that a more polarised covalent bond will have a higher $\nabla^2\rho_b$ value. The U-F bonds (of which the ρ_b metrics suggest are the most covalent driven relative to the other halogens) have highly polarised bonds, on account of the high electronegativities of the F-species; therefore, the high, positive values of $\nabla^2\rho_b$ would not be unexpected. If the $\nabla^2\rho_b$ values truly are dependent on the bond polarisation, this justifies the U-O bonds having the next highest $\nabla^2\rho_b$ values after the U-F bonds (O being the second most polarising atomic species after F), followed by the U-Cl bonds, then the U-Br bonds.

As shown in **figure 3.6** the $\nabla^2\rho_b$ values, dissimilar to the ρ_b values, do not necessarily scale with bond length. Which is interesting considering the we notice that the *cis*-bonds have higher $\nabla^2\rho_b$ values than the *trans*-bonds, implying a higher degree of polarisation. Overall, the data in **table 3.3** and **figure 3.6** imply that out of the metal-halogen bonds, the U-F (both *cis*- and *trans*-) have the highest degree of covalency and bond polarization, followed by the U-Cl and then the U-Br. Furthermore, the *cis*-bonds in the $[MOX_5]^-$ complexes have lower degrees of covalency than their respective *trans*-bonds, and higher orders of bond polarisation.

Comparing the $*UX_6$ and the $[UOX_5]^-$ complexes, **figure 3.6** shows that the ρ_b values for the constrained $*$U-X bonds are greater than the U-X$_{cis}$ values (by 0.005 au, 0.003 au, 0.003 au for X = F, Cl, Br), and lower than the U-X$_{trans}$ values (by 0.015 au, 0.012 au, and 0.007 au in the same order). This suggests that the replacement of a halogen ligand X with an O atom in the constrained $*UX_6$ complexes, causes an increase in charge accumulation at BCP of the *trans*-bond and a decrease in charge accumulation at the *cis*-bonds, characteristic of an increase in covalency in the *trans*-bonds, and decrease in the *cis*-bonds (although this is not quantitatively *exact* as the *trans*-bond lengths are all greater than the $*$U-X bonds).

Comparing the *cis*- and *trans*-bonds in each respective $[UOX_5]^-$ species, we see that that the *cis*-bonds have lower ρ_b and higher $\nabla^2\rho_b$ values, indicative of a decreased degree of overlap-driven covalency and increased degree of bond polarisation relative to the *trans*-bonds; this is probably expected considering their greater bond lengths. In terms of bond strength, Gibbs *et al*[140] state that the strength of a bond is proportional to the value of ρ_b, which results in the bonds shortening. Berryman[125] however, conjects that bond strength and bond covalency are in fact not synonymous.[125] We conclude that only by comparisons of like species, such as the *cis*- and *trans*-bonds in the same $[UOX_5]^-$ complex, can we infer ideas of covalency and bond strength, measurable by higher ρ_b values and bond lengths.[148] Considering this, on account of the shorter bond lengths and higher ρ_b values, we propose that the *trans*-bonds in the $[UOX_5]^-$ complexes have an increased bond strength relative to the *cis*-bonds.

Table 3.5 presents the BCP metric data for the d-block $[MOX_5]^-$ complexes (M = Mo, W and X = F, Cl, Br), as well as their corresponding MX_6 counterparts (both optimised and constrained).

Table 3.5. QTAIM data concerning BCP metrics of the d-block [MOX$_5$]$^-$ complexes, as well as their MX$_6$ counterparts (both optimised and *constrained), where M = Mo, and W. The value of the electron density at each BCP ρ_b is provided, along with the value of the Laplacian of the density, $\nabla^2\rho_b$, (of which is presented below in italics). All data is in atomic units au

M	X	Bond Critical Point (BCP)				
		[MOX$_5$]$^-$			*[MX$_6$]	[MX$_6$]
		M-O	M-X$_{cis}$	M-X$_{trans}$	*M-X	M-X
Mo	F	0.267	0.147	0.120	0.158	0.172
		0.986	*0.670*	*0.577*	*0.670*	*0.748*
	Cl	0.284	0.090	0.056	0.090	0.100
		0.917	*0.171*	*0.138*	*0.168*	*0.196*
	Br	0.286	0.073	0.053	0.073	0.080
		0.920	*0.106*	*0.109*	*0.120*	*0.137*
W	F	0.249	0.144	0.119	0.146	0.164
		0.929	*0.647*	*0.576*	*0.660*	*0.772*
	Cl	0.261	0.091	0.067	0.093	0.102
		0.929	*0.156*	*0.158*	*0.157*	*0.185*
	Br	0.264	0.077	0.055	0.077	0.083
		0.928	*0.091*	*0.103*	*0.106*	*0.121*

Perhaps the first thing to note, is that **table 3.5** and the bond length data (**tables 3.1** and **3.2**) for the d-block [MOX$_5$]$^-$ and MX$_6$ complexes confirm that the ρ_b values scale inversely with bond length[147] i.e. shorter bonds have higher ρ_b values, as first implied in the f-block complexes. Typically, the d-block, [MOX$_5$]$^-$ species appear to follow a similar trend to the f-block species, where the halogen bonds in the [MO**F**$_5$]$^-$ species have ρ_b values between 0.1 and 0.2 au, and the analogous M-X bonds in the [MO**Cl**$_5$]$^-$ and the [MO**Br**$_5$]$^-$ species have ρ_b values less than 0.1 au (M-Br with the lowest). This tells us that much like the f-block species, the M-F bonds have the highest charge accumulation relative to the other halogen bonds, indicative of the greatest degree of overlap-covalency.

Considering the Laplacian of the electron density $\nabla^2\rho_b$, the U-F bonds have the largest positive values of $\nabla^2\rho_b$ (**Mo**-F: 0.577, 0.670 for the *cis*- and *trans*-bonds, **W**-F: 0.576, 0.067), suggesting that similarly to the f-block species, the M-F bonds have the greatest

bond polarisations relative to the other halides. The HSAB framework prescribed for the f-block complexes, as well as the reasoning of the F-species being the most electronegative can be applied to validate these results.

We notice that the *trans*-ligand bonds in the [**Mo**OX$_5$]$^-$ and [**W**OX$_5$]$^-$ complexes have lower ρ_b and $\nabla^2 \rho_b$ values relative to the *cis*-ligand bonds, suggesting that the *trans*-ligand bonds have a decreased charge accumulation at the BCP (manifesting as a decreased degree of covalency), and an increased order of bond polarisation, relative to the *cis*-ligand bonds. In addition, the QTAIM integrated data in **table 3.4** shows that the *cis*-bonds in the d-block [MOX$_5$]$^-$ complexes have lower atomic volumes and greater charge depletions than the *trans*-bonds, also indicative of a greater degree of electron sharing. The opposite was the case for the f-block species and considering the formal definition of species exhibiting an TI, this seems expected.

Comparing each of the d-block [MOX$_5$]$^-$ complexes (where M = Mo, and W), for the X = Cl and Br, the ρ_b values of the M-X bonds are **greater** in the [**W**OX$_5$]$^-$ species than in the [**Mo**OX$_5$]$^-$ species. For X = F however, the ρ_b values of the M-F bonds are **lower** in the [**W**OX$_5$]$^-$ species than in the [**Mo**OX$_5$]$^-$ species. Additionally, the ρ_b values of the M-O bonds are **lower** in the [**W**OX$_5$]$^-$ species compared to that of the [**Mo**OX$_5$]$^-$ species. Effectively this tells us that the Cl- and Br-ligands in the [**W**OX$_5$]$^-$ complexes, are bonded more covalently than the Cl- and Br-ligands in the [**Mo**OX$_5$]$^-$ complexes. Whereas the F- and the O-ligands are bonded more covalently in the [**Mo**OX$_5$]$^-$ than in the [**W**OX$_5$]$^-$ species. The same is the case of the MX$_6$ complexes (both optimised and constrained), when X = Cl and Br, the **W**-X bonds have higher degrees of bond covalency than the **Mo**-X bonds (for the **W**X$_6$ and **Mo**X$_6$ species respectively), but when X = F, the **Mo**-X bonds have higher covalency characters than the **W**-X bonds. Applying the HSAB framework, we propose that the Mo(VI) species are 'harder' than the W(IV) species, as evidenced by Mo having a slightly smaller ionic radius (73 pm[139]) than the W (74 pm[139]); furthermore, the QTAIM atomic volumes in **table 3.4** confirm this size difference. The F and O species have similar ionic radii (119 pm, and 126 pm respectively[139]), as well as similar electronegativities (O being the second most electronegative element). Considering this, the O- and F-ligands would being classed as harder Lewis bases relative to the Cl- and Br-ligands, and so we would expect them

to have a stronger bonding interaction with the harder Lewis acid of the two d-block metals, Mo. On the other hand, the Cl and the Br, being relatively softer Lewis acids would have a stronger bonding interaction with the softer Lewis acid, W.

In total, BCP analysis of both TI and ITI-exhibiting complexes, yields that for the former, the *trans*-bonds are **less** covalent than the *cis*-bonds, and in the case of the latter, the *trans*-bonds are **more** covalent than the *cis*-bonds (where covalency in this case is pertaining to the overlap-driven type). This trend matches that of the bond length data, where TI-exhibiting species have relative **longer** *trans*-bonds, and the ITI-exhibiting species have relatively shorter *trans*-bonds. Furthermore, on account of the $\nabla^2 \rho_b$ metrics measuring bond polarisation,[125] the *trans*-bonds in the ITI-exhibiting species are **less** polarised than the *cis*-bonds, but in the TI-exhibiting species the reverse is the case: the *trans*-bonds are **more** polarised than the *cis*-bonds. Assuming that for like-bonds, a shorter length would indicate an increased bond strength,[140] the BCPs provide rationalisation, where shorter bonds (such as the *trans*-bonds in ITI-exhibiting complexes) have higher values of ρ_b, which can typically be considered to relate to higher thermodynamic stabilities of the bonds. We now turn our attention to the delocalisation indices afforded by QTAIM.[36]

3.3.2 Delocalisation indices

Delocalisation indices $\delta(A, B)$ measure the degree of electron sharing between two atomic basins, A and B (of which do not necessarily have to be 'formally bonded').[36] In unpolarised bonds, $\delta(A, B)$ values can be considered analogous to the classical notion of bond order. Higher values of $\delta(A, B)$ typically imply higher degrees of electron sharing. For example, LiH, one of the more definitive examples of an idealised ionic bond, has been shown to have a $\delta(Li, H)$ value of 0.20 au;[149,150] LF, another example has a $\delta(Li, F)$ value of 0.18 au.[150,151] Whereas more covalently bonded species, such as the O-Br bond in HOBr, that would generally be considered to have a greater degree of electron sharing, has a higher $\delta(O, Br)$ value of 1.05 au.[124] In addition, delocalisation indices have been shown to infer the polarity of the bond.[152] Along with BCP analysis, $\delta(A, B)$ values provide further characterisation to the bonding region between two species, differently to BCP metrics however, $\delta(A, B)$ values measure **both** overlap-driven and energy-driven covalency (BCPs are only concerned with the former). Therefore, a bonding region with a high $\delta(A, B)$ value but a low ρ_b value suggests that the energy-driven covalency type dominates. **Table 3.6** presents the $\delta(A, B)$ values for the d- and f-block, $[MOX_5]^-$ complexes, as well as the optimised MX_6 and constrained $*MX_6$ complexes.

Table 3.6. QTAIM data for the delocalisation indices (DI) of the f- and d-block [MOX$_5$]$^-$ complexes, as well as their MX$_6$ counterparts (both optimised and *constrained).

M	X	[MOX$_5$]$^-$			MX$_6$	*MX$_6$
		$\delta(U,O)$	$\delta(U,X_{cis})$	$\delta(U,X_{trans})$	$\delta(U,X)$	*$\delta(U,X)$
	F	1.951	0.752	0.840	0.961	0.935
U	Cl	2.004	0.826	0.986	1.088	1.062
	Br	2.031	0.863	0.991	1.129	1.103
	F	1.779	0.676	0.529	0.815	0.816
Mo	Cl	1.935	0.795	0.443	0.949	0.947
	Br	1.950	0.810	0.575	0.985	0.984
	F	1.632	0.639	0.497	0.743	0.744
W	Cl	1.788	0.748	0.524	0.906	0.907
	Br	1.835	0.795	0.542	0.956	0.957

When modelled with a suitable model chemistry, $\delta(A,B)$ values will generally scale to zero with the stretching of a bond length i.e. they scale inversely with bond length. This is reflected when comparing the f-block UX$_6$ and *UX$_6$ bond lengths and $\delta(U,X)$ values (the former has bond lengths of 200.8 pm, 247.3 pm , and 264.1 pm for X = F, Cl, Br; the latter has bond lengths of 210.45 pm, 257.53 pm, and 274.16 pm, same order), clearly the optimised U-X bonds, have longer bond lengths, which are accompanied by lower $\delta(U,X)$ values (roughly 0.025 au less). However, this is not necessarily the case for the d-block species, where the optimised MX$_6$ complexes, for the most part, despite having shorter bonds, in some cases (MoF$_6$, and all of the **W**X$_6$ species) actually have lower $\delta(M,X)$ values, relative to the constrained *MX$_6$ complexes.

Comparing the $\delta(M,X)$ values of the cis- and trans-ligand bonds for all [MOX$_5$]$^-$ species, we see that in the f-block [**U**OX$_5$]$^-$ complexes, the $\delta(U,X_{trans})$ values are **greater** than the $\delta(U,X_{cis})$ values, whereas in the d-block [MOX$_5$]$^-$ complexes, we see the opposite is the case, the $\delta(U, trans\text{-}X)$ values are **lower** than the $\delta(U,X_{cis})$; this is expected considering the relative bond lengths. This tells us that in the f-block species, the degree of electron sharing is greatest in the trans-bond relative to the cis-bonds, and

in the d-block species, the degree of electron sharing is greatest in the cis-bonds relative to the trans-bonds, which conclusively follows a similar trend as BCP metric data.

Considering the f-block $[\mathbf{U}O\mathbf{X}_5]^-$ species as a function of halogen X, the U-Br bonds (both the *cis-* and *trans-*bonds, from the $[\mathbf{U}O\mathbf{Br}_5]^-$ complex) have the highest $\delta(\mathrm{U}, \mathrm{X})$ values, followed by the $[\mathbf{U}O\mathbf{Cl}_5]^-$ and then the $[\mathbf{U}O\mathbf{F}_5]^-$ complexes, suggesting the degree of electron sharing in the U-X bonds is greatest when X = Br, and lowest when X = F. The opposite trend was shown in the charge accumulation metrics ρ_b, where the U-F bonds in the $[\mathbf{U}O\mathbf{F}_5]^-$ species have the greatest ρ_b values, indicative of the highest charge accumulation, followed by the U-Cl, and then the U-Br bonds. Effectively, these two opposing trends imply that in the case of the U-X bonds in the f-block species, the overlap-driven covalency (measurable by ρ_b metrics) and energy-driven covalency (indicative from both $\delta(\mathrm{A}, \mathrm{B})$ and ρ_b values) appear to scale opposingly, where the orbital-driven type is **greatest** in the U-F bonds and **lowest** in the U-Br bonds, and the energy-driven type, is **lowest** in the U-F bonds but **greatest** in the U-Br bonds. **Table 3.5** and **3.6** also show that this trend is the same for both of the d-block $[\mathbf{M}O\mathbf{X}_5]^-$ species (M = Mo, W), where the $\delta(\mathrm{M}, \mathrm{X})$ values and ρ_b metrics scale opposingly. The $[\mathbf{M}O\mathbf{F}_5]^-$ species have the highest values ρ_b values and the lowest values $\delta(\mathrm{M}, \mathrm{Br})$, and the $[\mathbf{M}O\mathbf{Br}_5]^-$ species have the lowest ρ_b values but the highest values of $\delta(\mathrm{M}, \mathrm{Br})$.

Comparing the M-X bonds in the d-block $[\mathbf{Mo}O\mathbf{X}_5]^-$ and $[\mathbf{W}O\mathbf{X}_5]^-$ complexes, **table 3.6** shows that the $\delta(\mathbf{Mo}, \mathrm{X})$ values are typically greater than the $\delta(\mathbf{W}, \mathrm{X})$ values (both *cis-* and *trans-*), suggesting a higher degree of electron-sharing in the bonds (however as they are constituted from different bonding species and exhibit different bond lengths, we can determine this qualitatively). Furthermore, **table 3.5** shows the ρ_b values of the **Mo**-X bonds are also greater than the **W**-X bonds, suggest that the **M**-X bonds in the $[\mathbf{Mo}O\mathbf{X}_5]^-$ species have higher degrees of overlap-driven covalency relative to the **W**-X bonds in the $[\mathbf{W}O\mathbf{X}_5]^-$ species. As DIs typically acknowledge both types of covalency, it seems possible, that the slightly higher $\delta(\mathbf{Mo}, \mathrm{X})$ values (relative to the $\delta(\mathbf{W}, \mathrm{X})$ values) are also due to this increase in orbital-driven covalency, whilst perhaps the energy-driven covalency in the $[\mathbf{Mo}O\mathbf{X}_5]^-$ and $[\mathbf{W}O\mathbf{X}_5]^-$ species' M-X bonds are similar (or scaling slightly with the bond length differences).

Comparing the f-block U-X bonds' $\delta(\mathbf{U}, \mathrm{X})$ values (in the $[\mathbf{UOX_5}]^-$ complex, both *cis*- and *trans*-) to their corresponding U-X bonds from the UX_6 counterparts, we see that the $\delta(\mathbf{U}, \mathrm{X})$ values of the former are lower than the $\delta(\mathbf{U}, X)$ values of the latter, suggesting the U-X bonds in the $[\mathbf{UOX_5}]^-$ complex have **lower** degrees of electron-sharing than of that in the UX_6 complex. As the $\delta(U, X_{cis})$ values are lower than the $\delta(U, X_{trans})$ values in the $[\mathbf{UOX_5}]^-$ complex, this suggests that replacing a ligand X with a strong σ-donor (O-ligand) in the UX_6 complexes causes the $\delta(\mathbf{U}, axial\text{-}X)$ to decrease by 19.0%, 24.1%, and 23.6% (forming the *trans*-bond) and the $\delta(\mathbf{U}, equatorial\text{-}X)$ by 12.6%, 9.4%, and 12.2% (forming the *cis*-bonds) for the F, Cl, and Br ligands respectively.

In the d-block complexes (M = Mo, W), a similar trend is shown when comparing the M-X bonds' $\delta(\mathbf{M}, \mathrm{X})$ values in the $[\mathbf{MOX_5}]^-$ complexes to that of the corresponding MX_6 complexes. Both the $\delta(M, X_{cis})$ and $\delta(M, X_{\mathrm{trans}})$ values (from the $[\mathbf{MOX_5}]^-$ complexes) than the MX_6 complexes, with the $\delta(\mathbf{M}, trans\text{-}X)$ values being lower than the $\delta(M, X_{cis})$. Therefore replacing a ligand X with an O species in the MX_6 complexes causes the electron-sharing in the bonds to decrease in both the axial and equatorial directions (with the latter being most significant).

3.4. Natural Bond Orbitals Analysis

Following the QTAIM topological approach, where we provided clarification into the energy-driven and overlap-driven covalencies established in the M-X bonds in the $[MOX_5]^-$ complexes, we now turn our attention to an alternative orbital-based approach to assess bonding covalency, natural bond orbital analysis (NBO).

3.4.1. NBO Analysis of the f-block Species

As discussed in **section 2.4.2**, NBO assigns each atomic species in a molecule a Lewis structure, as well as a set of orthonormal, localised, bonding orbitals akin to the conical s, p, d, and f. Furthermore, in the case of a formal bond between two Lewis structures, NBO details each species' contributions into the bond, providing insights to the degree of covalency and bond polarisation in terms of bond orbitals. **Figure 3.7** shows the NBO data of the f-block species' U-X σ-bonds, where the individual bond orbital percentages of the *cis-* and *trans*-bonds, from each species are scaled to the species contribution to the bond. Additionally, the NBO data for the corresponding U-X σ-bonds from the optimised UX_6 complexes are also presented. The data presented in **figure 3.7** is provided in the supplementary section (**section 7**, **table 7.1**).

Firstly, it would be useful to give an illustrative example, to clarify what we mean by the bond contribution percentages and 'scaled up' bond orbital percentages. Typically, a 'perfectly' covalent metal-halogen bond would have a 50% bond contribution from each bonding species. The degree of covalency increases with the metal contribution percentage, as the metal species becomes more 'involved' with the bonding. As for the natural bond orbitals, NBO provides a break-down of the species' contribution to a bond in terms of percentages of s, p, d, and f-bond orbital character. We 'scale' these bond orbital percentage (by multiplying it by the species bond contribution percentage), so as to obtain the exact percentage of bond orbital from that species in the overall bond. In the case of the $[UOX_5]^-$ complexes, the in U-X bonds are a result of around 10-20% uranium contribution, and 90-80% halogen contribution. A **higher** U-contribution (accompanied by a **lower** X-contribution) would signify a **greater** shared element to the U-X bonding, characteristic of being **more covalent.**

Perhaps the first thing to note from **figure 3.7** is that as the halogen atomic number increases (moving from F to Br), the degree of covalency increases for both the *cis-* and *trans*-bonds, as indicated by the higher U (and lower X) contributions to the U-X bonds (and this is the case for both the $[UOX_5]^-$ and the UX_6 complexes). Resultantly, this tells us, that by NBO classification, the lowest degree of bond polarisation and highest degree of bond covalency resides in the U-Br bonds, followed by the U-Cl, and then the U-F bonds are the least covalent-like and polarised. We note that this trend in covalency agrees with the QTAIM $\delta(U, X)$ values (shown in **table 3.6**) but disagrees with the QTAIM ρ_b values (**table 3.3**), where the former classifies both overlap-driven and energy-driven, and the latter classifies overlap-driven exclusively. This suggests that the NBO covalency characterisations are predominantly focused on the elucidation of energy-driven covalency, and not necessarily overlap-driven. Furthermore, the NBO trend in bond polarisations matches that of the QTAIM $\nabla^2 \rho_b$ metrics, whereby the U-F species have the most positive values (indicative of a more polarised bond).
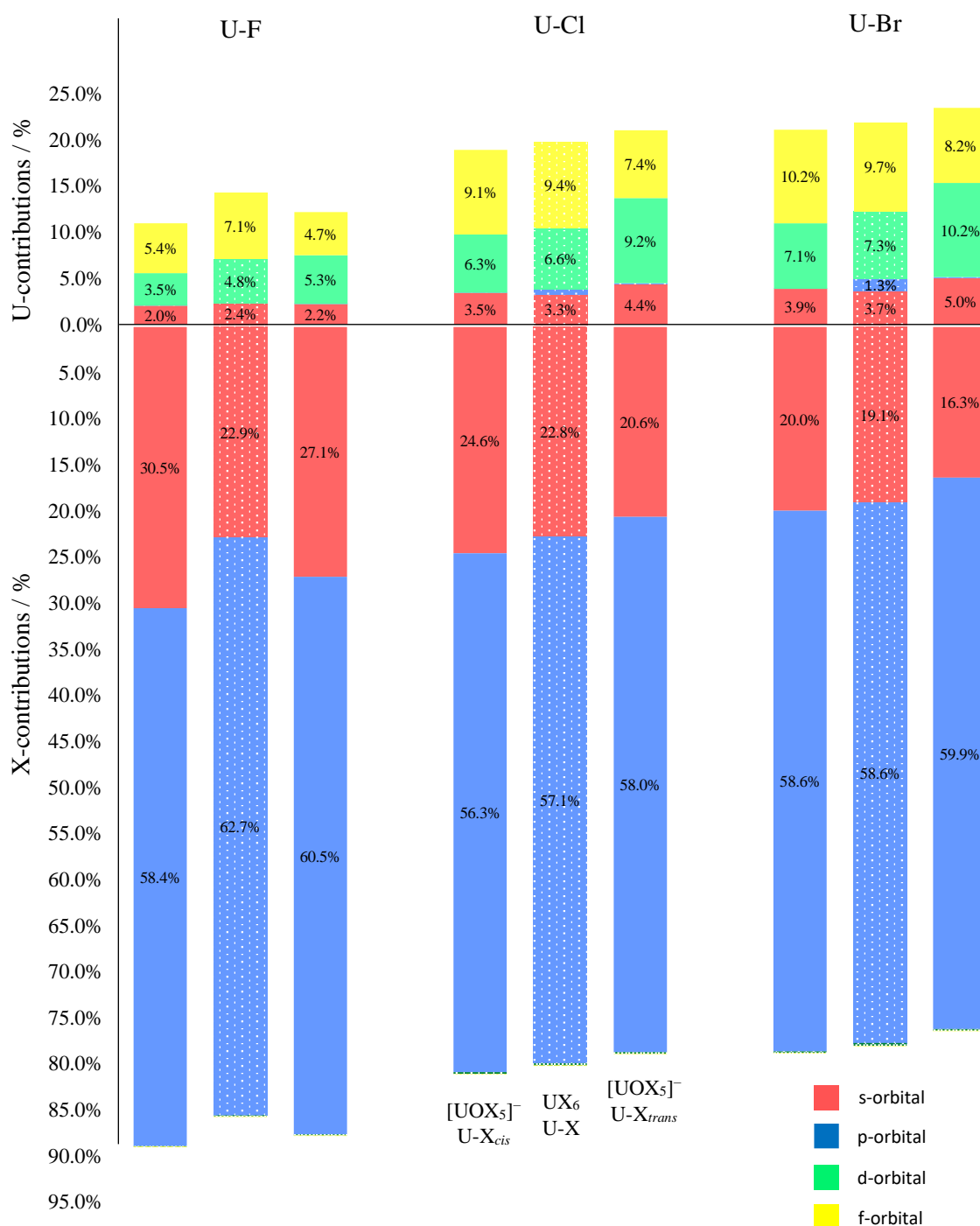
Figure 3.7. NBO data for the U-X σ-bonds for the $[UOX_5]^-$ and UX_6 complexes, where X = F (left trio), Cl (middle), and Br (right). The top part of the graph shows the U-contributions to the bond (%); the bottom half shows the halogen X-contributions to the bond (%). Within each of the groupings, the left and right columns represent the *cis*-bonds and *trans*-bonds in the $[UOX_5]^-$ species; the middle column represents the U-X bonds in the corresponding UX_6 complexes. For each bond contribution, a percentage for the constituent bonding orbitals are provided (s, p, d, and f in the colours red, blue, green and yellow respectively).

It is interesting to see the significance of the f-bonding orbitals from the U species in the U-X bonds, reminding us that the general FEUDAL[34,38] bonding model, (f's essentially unaffected, d's accommodate ligands) breaks down in the case of the ITI exhibiting complexes, as previously shown by Berryman.[37] However, the fact that the UX_6 complexes, that do not exhibit an ITI, also show dominant f-orbital contributions, suggests the FEUDAL model may not be apparent in NBO analysis. Notable, is that there are no p-orbital contributions from the U, which is surprising considering that the *pseudo*-core 6p-orbital plays an integral role in the polarisation model of the ITI.[7] However, if we recall, the model describes how the 6p-orbital effectively lowers the energy of adjacent orbitals, allowing for more significant overlap of those orbitals. Furthermore, this suggests that the 6p-orbital plays more of an indirect role in the ITI, and therefore it is probably expected to be absent in the NBO analysis of the bonding.

By modelling the $[UOX_5]^-$ complexes as a 'deviations' from the UX_6 complex: for X = Cl and Br, we see that the replacement of a ligand X with a ligand O in the UX_6 causes the equatorial bonds (that go on to become the *cis*-bonds in the $[UOX_5]^-$ complex) to **decrease** in covalency, on account of lower U-contributions (0.4% and 0.8% decrease for the Cl and Br variants respectively); the axial bonds (that become the *trans*-bonds) **increase** in covalency, on account of greater U-contributions (1.4% increase for both Cl and Br variants). For the $[UOCl_5]^-$ species, the decreased covalency in the *cis*-bonds compared to the UCl_6 complexes appears to be mediated by a decrease in both d- and f-orbital constituents (0.3% for both), and an increase in the s-orbital (0.2%). For the $[UOBr_5]^-$ species, the decrease covalency is also mediated by a decrease in d-orbital (0.2%) and increase in s-orbital (0.2%), but alternatively, an increase in the f-orbital (0.5%). However, comparing U-X bonds in the UBr_6 and UCl_6 species, we see the former has a more significant p-orbital character, which may affect the change in f-orbital character when compared to the $[UOBr_5]^-$ species. The **increased** covalency, of the *trans*-bonds in the $[UOX_5]^-$ complex (X = Cl, Br) compared to the UX_6 bonds, appears to be driven by a simultaneous **increase** in d-orbital (2.6% for the U-Cl*trans* and 2.9% for the U-Br*trans*) and s-orbital (1.1%, and 1.3%, same order), subsidised by a decrease in f-orbital character (2.0% and 1.5%, same order).

As for X = F species, replacing a ligand F in the UF_6 species with an O ligand causes the U contributions in both axial (*trans*-) and equatorial (*cis*-) U-F bonds to decrease, indicative of a decrease in the degree of bond covalency, with the latter being more significant. The decrease in covalency of the *cis*- and *trans*-bonds compared to the UF_6 bonds is primarily driven by an decrease in f-orbital character (1.7% for the *cis*-bonds, 2.4% for the *trans*-bonds), as was the case for just the *trans*-bonds in the $[UOCl_5]^-$ and $[UOBr_5]^-$ species (but in these cases, the *cis*-bonds' orbital constituents remained relatively uniform with the UX_6 orbital constituents). What is interesting is that the d-orbitals contributions increase in the *trans*-bonds (4.8% in the UF_6 to the 5.3% in the U-F$_{trans}$ bonds) but decrease in the *cis*-bonds (4.8% to 3.5% in the U-F$_{cis}$ bonds). This overall implies that the increased covalency of the *trans*-bond can be traced to an increased d-bond orbital character.

Comparing the *cis*- and *trans*-bonds in terms of X- and U-contributions to the bond, we see that the *cis*-bonds have lower U and higher X contributions than the *trans*-bonds. This describes the U species as being less 'involved' in the U-X$_{cis}$ bonds relative to the U-X$_{trans}$ bonds; suggests a decreased bond covalency in the *cis*-bonds relative to the *trans*-bonds, agreeing with both the bond length and topological analysis. Furthermore, the increased covalency in the *trans*-bond, relative to the *cis*-bond, appears to be driven by a greater s-orbital (0.2%, 0.9%, and 1.1% for the X = F, Cl, Br respectively), and d-orbital constituents (1.8%, 2.9%, and 3.1%, same order), whilst subsidised by a lower f-orbital constituent (0.7%, 1.7%, and 2.0%, same order). Overall, this suggests that the shortened and relatively more covalent *trans*-bonds (as characterised by bond optimisations and QTAIM) in ITI-exhibiting molecules, can be accounted for due to an increase in d- and s-orbital, and a decrease in d-orbital constituents by NBO definitions.

3.4.2. NBO Analysis of the d-block Species

We have attempted to assess the d-block $[MOX_5]^-$ (M = Mo, W) species with NBO. However, it was found that the d-block species did not 'conform' to Lewis-like structures as easily as the f-block species. Using the \$CHOOSE function in the NBO software,[109] we were able to manually assign Lewis-structures to the [**Mo**OX_5]$^-$ species (where X = Cl, and Br), but puzzlingly, not the [**W**OX_5]$^-$ or [**Mo**OF_5]$^-$ species. **Figure 3.8** presents the NBO data of the [**Mo**OCl_5]$^-$ and [**Mo**OBr_5]$^-$ species, along with their analogous $MoCl_6$ and $MoBr_6$ complexes. The data presented in **figure 3.8** is provided in the supplementary section (**section 7**, **table 7.2**).

Figure 3.8 shows that for the d-block [**Mo**OX_5]$^-$ species, the *trans*-bonds have a **lower** Mo-contribution percentage (17.0% and 17.9% for X = Cl, and Br respectively) than the *cis*-bonds (26.1% and 24.6%, same order), suggesting a **decrease** degree of covalency for the former. Considering the f-block [**U**OX_5]$^-$ species showed the opposite trend via NBO analysis (the *trans*-bonds had **greater** U-contribution than the *cis*-bonds), and considering our characterisation of the ITI and TI in both the bond length and QTAIM sections showed the *trans*-bonds had **increased** covalency in ITI-exhibiting species, and **decreased** covalency in TI-exhibiting species, this trend between the d-block *cis*- and *trans*-bonds, via bond-orbital analysis seems expected.

Comparing the [**Mo**OX_5]$^-$ species to their MoX_6 counterparts, we see a similar trend as was shown between the [**U**OF_5]$^-$ and UF_6 species, where both the *cis*- and *trans*-bonds (of the [**Mo**OX_5]$^-$ complex) have **lower** metal contribution percentages than the Mo-X in the MoX_6 complexes. In terms of the bonding orbital characters, we see that the relative decrease in Mo-contribution is mediated by a **decrease** in both s- (6.0% for Cl, 7.1% for Br) and d-orbital (4.9% and 7.7%) constituents. For the *cis*-bonds, we see that Mo-contributions in the Mo-Cl_{cis} bonds (from the [**Mo**OCl_5]$^-$ complex) have similar orbital constituents to the Mo-Cl bonds from the $MoCl_6$ complex (differing by around 1% for both s- and d-orbitals). whereas in the Br-based derivative, the Mo-Br_{cis} bonding has significantly lower s-orbital character (4.5%) from the Mo-contribution than in the Mo-Br bonds in the $MoBr_6$ complex.
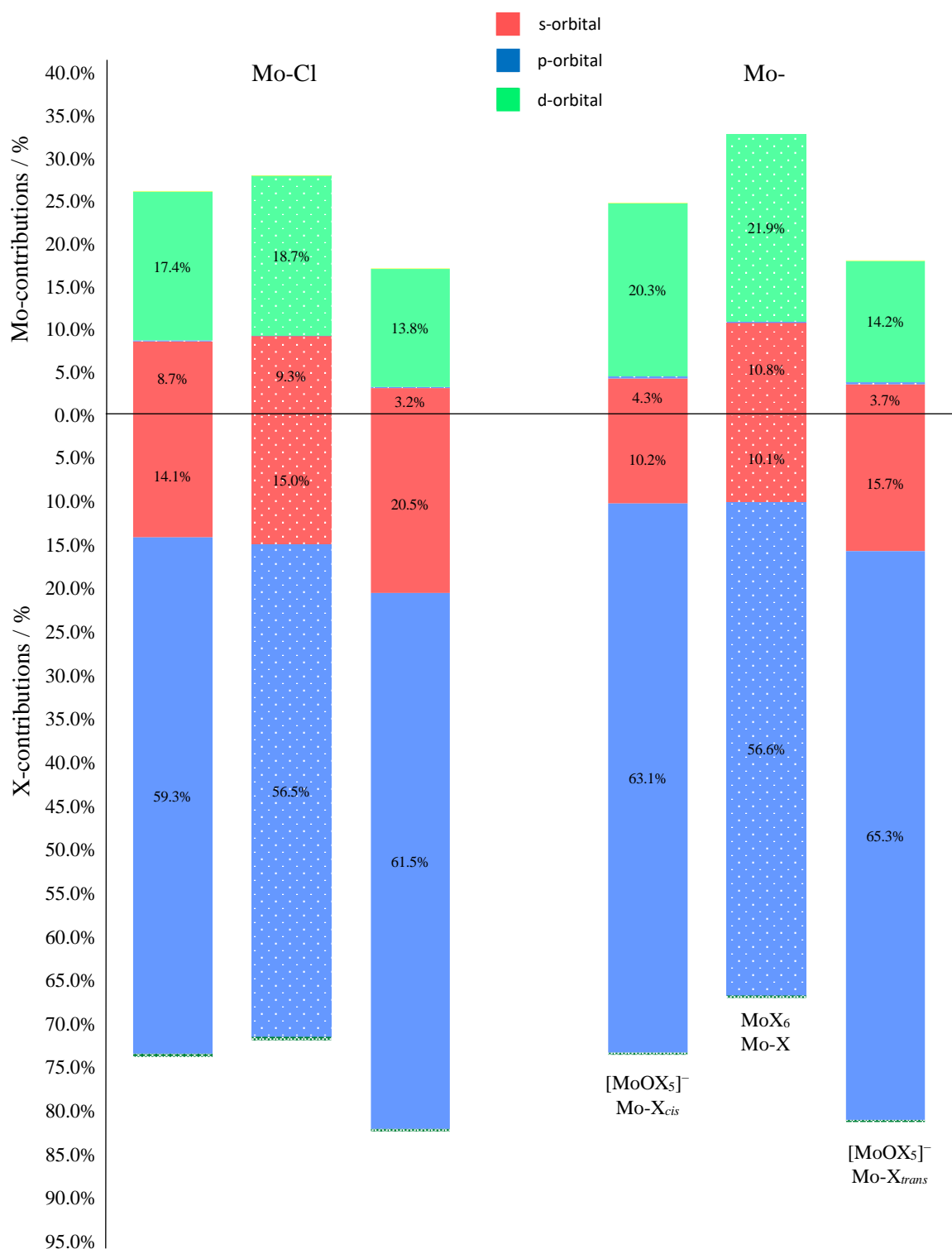
Figure 3.8. NBO data for the Mo-X σ-bonds in the [MoOX$_5$]$^-$ and MoX$_6$ complexes, where X = F (left trio), Cl (middle), and Br (right). The top part of the graph shows the Mo-contributions to the bond (%); the bottom half shows the halogen X-contributions to the bond (%). Within each of the groupings, the left and right columns represent the *cis*-bonds and *trans*-bonds in the [MoOX$_5$]$^-$ species; the middle column represents the Mo-X bonds in the corresponding UX$_6$ complexes.

Figure 3.8 unexpectedly seems to imply that for the d-block $[MoOX_5]^-$ complexes, X = F, Br, the *cis*-bonds are more polarised than the *trans*-bonds, and furthermore, less covalent in character. Considering our definitions and interpretations of the TI up to this point, this is puzzling. The NBO data for $[MoOCl_5]^-$ seems to model the TI as we would expect, where the *trans*-bonds are typically more polarised and more ionic (less covalent) than the *cis*-bonds. Furthermore, **figure 3.8** shows that in the $[MoOCl_5]^-$ species, the *cis*-bonds are relatively uniform to the Mo-Cl bonds in the $MoCl_6$ complex, whereas the *trans*-bond **decrease** covalency character, a result of their lower s- and d-orbital contributions (the latter being more significant). Interestingly, in the f-block $[UOCl_5]^-$ species, the *cis*-bonds are also relatively uniform with the UCl_6 bonds, whilst the *trans*-bonds **increase** in covalency, on account of an increase in d-orbital character.

Chapter 4

Results & Discussions at the Excited States

4.1 Overview of the Excited States

Following on from our characterisation of the ITI/TI in the ground state, our aim here in the excited state sections, is to find specific electronic transitions between molecular orbitals (MO) that could effectively remove, decrease or increase the ITI/TI. This was considered by identifying, and then exciting out of (or into) 'interesting' MOs found at the ground state; then allowing the structure to relax under a geometry optimisation at this new excited state. Our conjecture was that if these particular MOs had contributory roles to the ITI or TI, depopulating (or populating) would yield characteristic differences influencing the extent of the ITI or TI.

We define 'MOs of interest' as any MOs around the UV/Vis region that would characteristically affect the linear O-M-X$_{trans}$ moiety in the [MOX$_5$]$^-$ complexes differently to the axial *cis*-ligands; effectively causing a shift in the magnitudes of ITI or TI. MOs pertaining to the linear O-M-X$_{trans}$ moiety are A$_1$ in symmetry. The excited state section is separated into two parts: assessment of the excited states in the ITI exclusively (which only include the f-block species, **complexes I – III**, **figure 1.3**), and assessment of the excited states pertaining to **both** the ITI and the TI (which involves *all* complexes in **figure 1.3** **I – IX**). The excited state properties of each of the d- and f-block **complexes I – IX** were investigated using a time-dependant density functional theory approach (TD-DFT), implemented with the ESCF program[153] from the TURBOMOLE[61] software package. The calculations use the same basis sets (aug-cc-pVTZ for the main group elements) and electronic structure method, B3LYP detailed in previous sections. TD-DFT is the generalisation of the methodology provided by DFT to the excited states, it is formally based around the Runge-Gross (RG) theorem, essentially a time-dependant analogue of the Hohenberg-Kohn (HK) theorem.[154]

Complexes I – IX are all C$_{4v}$ symmetry, with 8 symmetry operations: E (the identity operation), a C$_4$ rotational axis (±90° rotations), a coincident C$_2$ axis, together with 2σ$_v$ and 2σ$_d$ mirror planes. The principle C$_4$ axis coincides with the O-M-X$_{trans}$ moiety.

4.2 Excitations Exclusive to the ITI

The intuition behind considering how excitation could affect the ITI came from a paper published by Kaltsoyannis *et al.*[8] They showed that by considering the MOs of differently substituted $[UOX_5]^-$ complexes, where X = F, Cl, and Br (the same used in this project), one could rationalise the different ITI magnitudes. To elaborate, a species exhibiting lower magnitudes of ITI, are shown to exhibit higher antibonding character in the M-X$_{trans}$ position (for example the bromine f-block complex), whereas species exhibiting higher levels of ITI magnitudes (such as the fluorine types) have lower antibonding character in the in the M-X$_{trans}$ position.[8] A rationalisation of this is afforded using Denning's[7] polarisation model (a reminder that this is critically dependant of the relative parities of the metal's HOMO and LUMOs, as detailed in the introduction). Higher antibonding character in the M-X$_{trans}$ static interaction causes a greater polarisation of the metal's core electrons, resulting in an increase in dipolar character and increase in the *trans*-bond length (decreasing the ITI). Our work follows on from here, detailing what happens to the structure when electrons are excited **out of** certain orbitals and into non-bonding orbitals (effectively reducing or increasing their bonding contributions), as far as we are aware this is the first documentation of attempting to remove the ITI via excitation. **Figure 4.1** presents a flow chart for the methodology in this section.

1. Locate 'interesting' MOs (bonding or antibonding) that could play a role in the ITI	**2.** Identify the same corresponding MOs in all other f-block complexes	**3.** Excite out of (or into if it is antibonding) the interesting MO	**4.** Allow the structure to 'relax' under a geometry optimisation of the excited state	**5.** Compare the *cis- trans*-bond ratios to the ground state bond ratios

Figure 4.1. flow chart of the methodology behind the excited state calculations exclusive to the f-block species.

Considering tasks 1 and 2 in **figure 4.1**, for each halide derivative of the $[UOX_5]^-$ complexes, we have characterised two types of 'interesting' MOs exclusively in the f-block species, that have similar energies and quantitative characteristics. Both of the MOs definably have U-fz^3 character. The first type shows formal bonding between the O-2pz and *trans*-Cl-2pz of which we label from now on as the σ_u MO (on account of their *approximate* parity symmetries resembling that of a formal σ_u interaction). The

second type is the antibonding counterpart to the σ_u MO, which we define here as the σ_u* MO. **Figure 4.2** shows depictions of these MOs for each halogen type as well as their energies in eV. All MOs in **figure 4.2** span the A_1 irreducible representation; their similar qualitative representations lead us to believe they are comparable. Henceforth, when referring to these molecular orbitals, we will use the code MX-μa_1, whereby M is the metal, X is the ligand, and μ describes the a_1 MO. For example, the top left MO in **figure 4.2** would be UF-14a_1.

Figure 4.3a, shows the non-bonding U species' f_δ virtual orbital, where the electrons from the σ_u MOs (**figure 4.2a**) will be excited into, an illustration of this movement of electronic energy is shown in **figure 4.4a**, we henceforth title this non-bonding orbital δ_U. The δ_U MOs are highly desirable for exciting into due to their symmetric and uranium-centric nature. Typically, exciting into these non-bonded virtual orbitals would cause the U(VI) cation to increase in electronic charge, lowering its oxidation state; reducing its effective nuclear pull, which resultantly, we would expect would lower the interactions between the U and the ligands. The advantage, however, is that all U-X bonds would be affected in the same way, with no directionality to the changes.

$[UOF_5]^-$	$[UOCl_5]^-$	$[UOBr_5]^-$

	$[UOF_5]^-$	$[UOCl_5]^-$	$[UOBr_5]^-$
σ_u	**14a₁** (−4.90 eV)	**19a₁** (−6.06 eV)	**28a₁** (−5.63 eV)
σ_u^*	**16a₁** (2.45 eV)	**21a₁** (0.82 eV)	**30a₁** (0.49 eV)
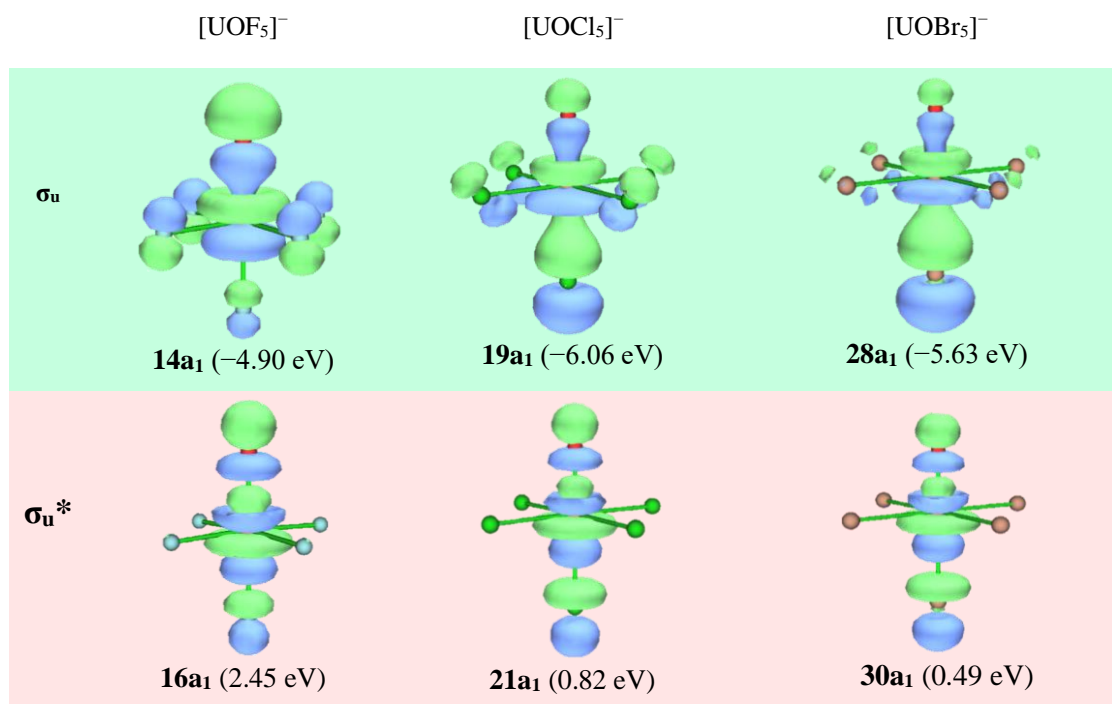
Figure 4.2a (top) + **4.2b** (bottom) depictions of the f-block σ_u and σ_u^* molecular orbitals for each halogen type, as well as their a_1-type classification and orbital energy in parenthesis.

δ_U virtual	*cis*-$p_{x/y}$ occupied
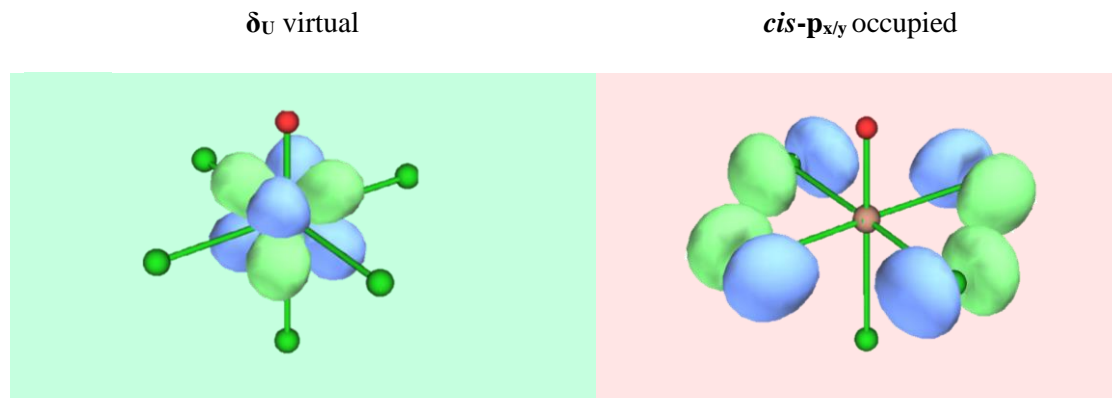
Figure 4.3a (left) + **4.3b** (right). MO depictions for the orbitals we excite into (left) and out of (right). These depictions are taken from the $[UOCl_5]^-$ complex. The δ_U non-bonding orbital (left) has the following energies and classifications for each halogen type: 0.087 eV (3b1), −0.803 eV (4b1), and −0.922 eV (8b1) for the F, Cl, and Br-types respectively. The *cis*-$p_{x/y}$ non-bonding occupied orbitals (right) have the following energies and classifications for each halogen type: −7.47 eV (2b1), −5.98 (3b1), and −5.50 eV (7b1) for the F, Cl, and Br-types respectively.

Figure 4.3b shows the occupied *cis*-$p_{x/y}$ non-bonding MOs, of which their electrons will be excited out of, and into the antibonding σ_u^* MOs (**figure 4.2b**), an illustration of this movement of electronic energy is shown in **figure 4.4b**. Differently to excitations involving the δ_U orbital, we would expect excitations involving the *cis*-$p_{x/y}$ orbital to affect the *cis*-ligands differently to the *trans*-ligands as the MO is highly directional in the position of the former. As clearly shown in **figure 4.3b**, the density is concentrated only on the equatorial ligands and not the axial ligands; we speculate that exciting from this orbital would cause the *cis*-ligands to decrease in electron density slightly more so than the *trans*-ligands. If this is the case, we might expect the interaction between the U and the *cis*-ligands to decrease slightly more so than that of the U and the *trans*-ligands (manifesting as a greater bond length elongation).
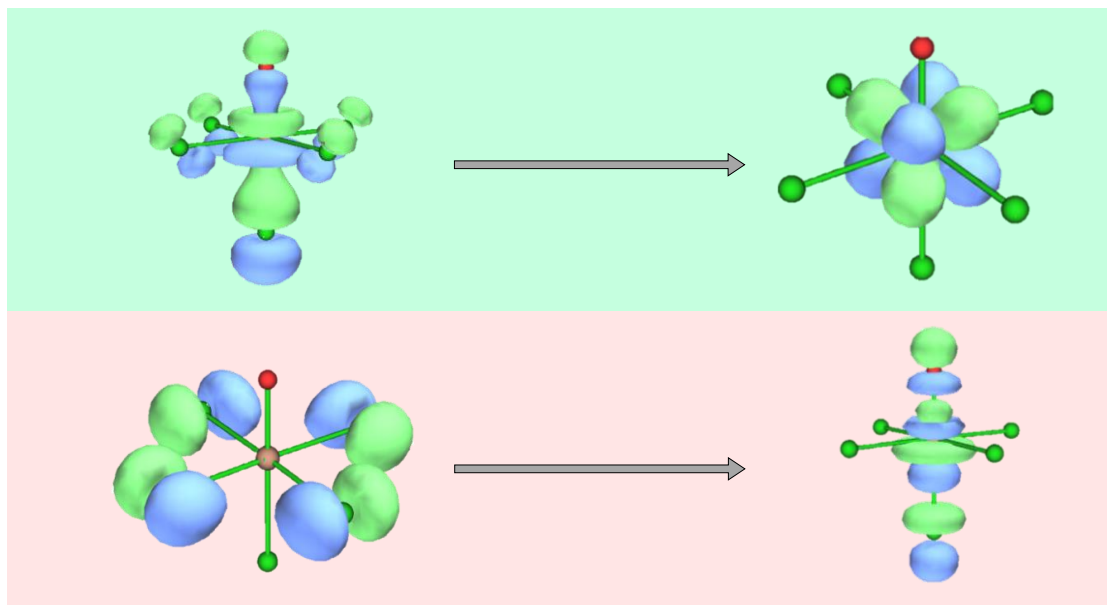

Figure 4.4a (top) + **4.4b** (bottom). The top illustration shows the excitation involving the σ_u MOs (**fig. 4.2a**) being excited to the δ_U MOs (**fig. 4.3a**). The bottom illustration shows the excitation involving the σ_u^* MOs (**fig. 4.2b**) being populated from electrons from the *cis*-$p_{x/y}$ MOs (**fig. 4.3b**).

The first 20 singlet excitations in the B_1 state were considered for the $[UOX_5]^-$ complexes, of these 20, specific excitations that predominantly involved the desired MO transitions (illustrated in **figure 4.4**) were identified. **Table 4.1** summarises the relevant transitions at the ground state geometry, including their dominant orbital transition contributions, alongside their excitation number (respective of the ground state vertical excitation) and the excitation energy. When referring to excitation, we use the capitalised $\sum$ symbol to distinguish which excitation is pertaining to which MO, for example, excitations involving a transition out of the σ_u MO will be referred to as $\sum_u$ excitations, and excitations involving transition into the σ_u* MOs will be referred to as $\sum_u$* excitations.

Table 4.1. The Σ_u and Σ_u* excitations at the ground state geometry, of which predominantly involve the σ_u and σ_u* MOs respectively (shown in bold) are presented as a sum of the dominant contributions and excitation energies (Ex. Energy) in eV.

Excitation	Complex	B_1 vector	Ex. energy / eV	Contributions	$\left\lvert \text{Coeff.} \right\rvert^2 \times 10^2$
F-Σ_u	$[UOF_5]^-$	**6**	4.627	**14a1 → 3b1**	89.4
				10e → 12e	4.2
Cl-Σ_u	$[UOCl_5]^-$	**7**	3.013	**19a1 → 4b1**	48.7
				14e → 16e	28.0
				13e → 16e	10.7
				20a1 → 4b1	4.8
Br-Σ_u	$[UOBr_5]^-$	**7**	2.651	**28a1 → 8b1**	44.5
				24e → 27e	30.2
				25e → 27e	13.2
				25a1 → 28b1	8.1
F-Σ_u*	$[UOF_5]^-$	**16**	6.410	**2b1 → 16a1**	99.9
Cl-Σ_u*	$[UOCl_5]^-$	**15**	4.511	**3b1 → 21a1**	84.8
				11e → 16e	9.8
Br-Σ_u*	$[UOBr_5]^-$	**14**	4.088	**7b1 → 30a1**	49.2
				26a1 → 8b1	29.6
				22e → 27e	17.9

Figures 4.5(a-c) show transition diagrams for the $[UOX_5]^-$ complexes (X = F, Cl, and Br), the **middle** columns display the vertical excitations at the ground state geometry, the green lines represent the Σ_u excitations, the red lines represent the Σ_u* excitations, and the yellow lines represent excitations concerning the metal's dz^2 MO (which is discussed further in **section 4.3**). Following the identification of these excited states of

interest, the molecular structure of each of these states was optimised (tasks 3 + 4 in **figure 4.1**). The transitions at the replaced σ_u focussed geometry (from the Σ_u excitation) are shown in the right-hand column; the transitions at the replaced σ_u^* focused geometry (from the Σ_u^* excitation) are shown in the left-hand column. In both cases, at the excited state geometries, the ground state energy is increased, and the energy of the MO of interest is decreased (relative to the ground state geometries).

Considering the data in the top section of **table 4.1**, we acknowledge that the desired transitions for the $[UOX_5]^-$ complexes where X = Cl, and Br, have low contribution percentages (48.7% and 44.5% for the Cl, Br respectively). The $[UOF_5]^-$ species on the other hand, has a far more definitive contribution amount from the desired transition (89.4%). Nevertheless, the fact that both species have inherently similar contributions and energies tells us that these excitations must be analogous and comparable.
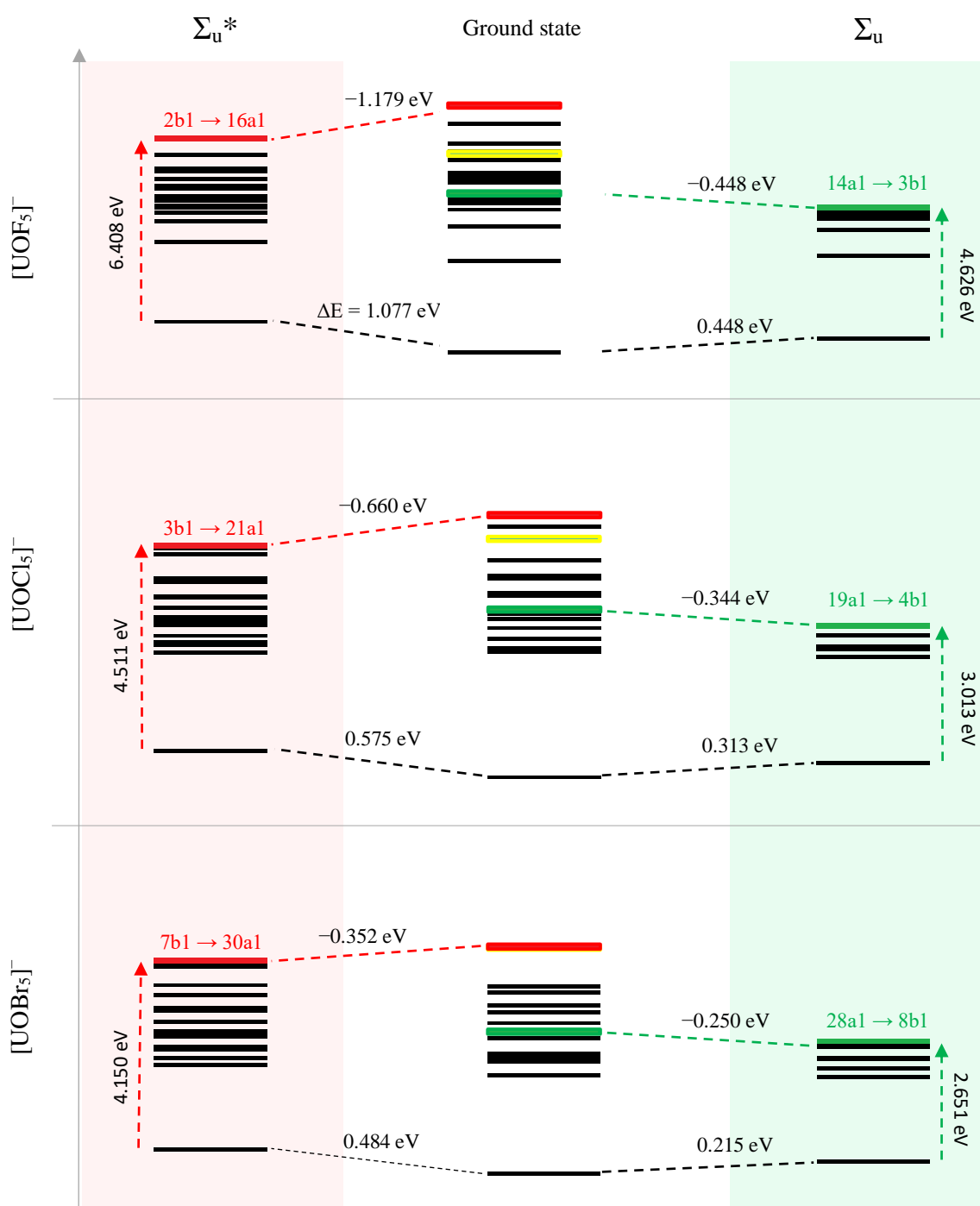
Figures 4.5a, b, and c (top to bottom). Transition diagrams for B_1 vertical singlet excitations in the $[UOX_5]^-$ complexes, where X = F (top. **Fig. 4.5a**), X = Cl (middle, **fig 4.5b**), and X = Br (bottom, **fig 4.5c**). The middle columns show the vertical excitation energy in the ground state geometry, the left-hand columns show vertical excitation energies when optimised to the Σ_u^* state's corresponding geometry; the right-hand columns show the energies when optimised to the Σ_u excited state geometry.

4.2.1. Optimising the Σ_u Excited State

Figure 4.6 shows a plot of the bond distances in picometres (pm) for all f-block $[UOX_5]^-$ species at the ground state geometries, alongside the Σ_u and Σ_u^* excited state geometries (green and red plot points respectively). The numerical data for this graph is presented in **section 6**, **table 6.12**. There is an 'idealised' line (grey, dashed) that represents a 'perfect' bond ratio value of 1, where the *cis-* and *trans*-bonds are equal. If the plot points go over this line from the ground state, then it signifies a reversal of the influence (ITI species now exhibiting a TI for example). Alongside this, the excited state bond lengths are presented as a percentage increase from the ground state bond lengths for the Σ_u excited state (**fig 4.7**), and the Σ_u^* excited states (**fig 4.8**).

Both **figures 4.6** (**b** + **c**) and **4.7** show that the $[UOCl_5]^-$ and $[UOBr_5]^-$ complexes behave similarly when optimising at the respective UCl-Σ_u and UBr-Σ_u excitations. For the X = Cl complex, the *cis*-bond lengths increase by 2.7% relative to their original ground state value (from 257.7 pm to 264.5 pm); the *trans*-bond length increases by 7.3% (251.5 pm to 269.8 pm), and the U-O bond length increases by 1.2% (177.8 pm to 179.9 pm). For the X = Br complex, the *cis*-bond lengths are increased by 2.4% (274.2 pm in the ground state to 280.6 pm in the excited), the *trans*-bond is lengthened by 6.1% (268.6 pm to 285.1 pm), and the U-O bond length increases by 0.9% (177.4 pm to 179.0 pm). The ITI magnitude for the $[UO\mathbf{Cl}_5]^-$ complex changes from 0.977 in the ground state, to 1.020 in the excited state, and for the $[UO\mathbf{Br}_5]^-$ complex, 0.98 to 1.016. The values now being greater than 1, signifies a reversal of the ITI into a *trans*-influence, on account of their *trans*-bond lengths being greater than the *cis*-bond lengths in the excited state geometries.
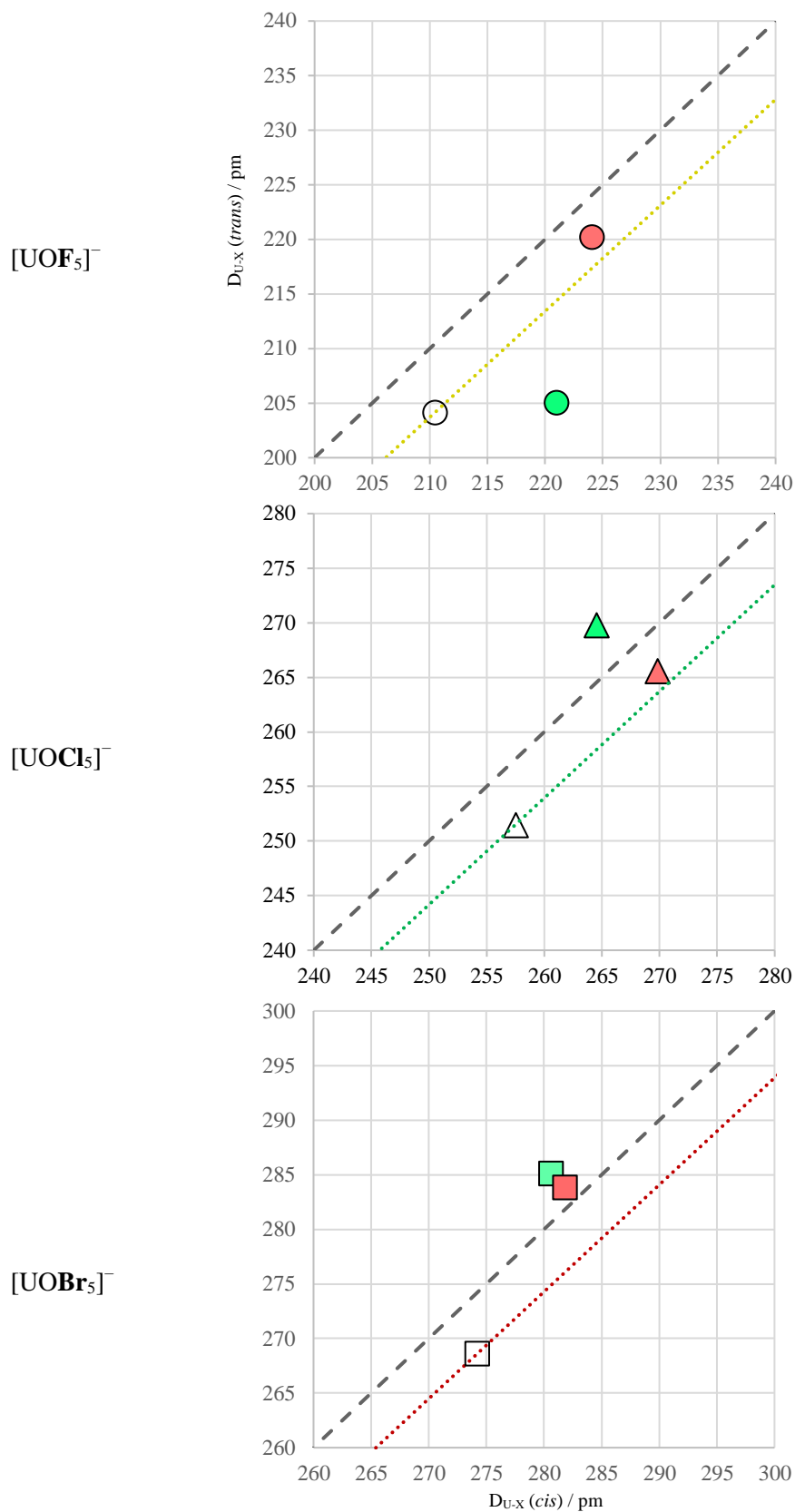
Figure 4.6a-c. Plot of the *cis-* (x-axis) and *trans-*bond (y-axis) distances (in pm) of the $[UOX_5]^-$ complexes at the ground (colourless), $\sum_u$ (green) and $\sum_u^*$ (red) excited state geometries where X = F (top, **fig 4.6a**), Cl (middle, **fig 4.6b**), and Br (bottom, **fig 4.6c**). An idealised line with a *cis/trans* bond ratio of 1 is plotted (dashed grey line). Numerical data for these plots is shown in **table 6.12** (**section 6**).

Complex	ITI (gs)	ITI ($\sum_u$)
[UOF$_5$]$^-$	0.970	0.928
[UOCl$_5$]$^-$	0.977	1.020
[UOBr$_5$]$^-$	0.980	1.016
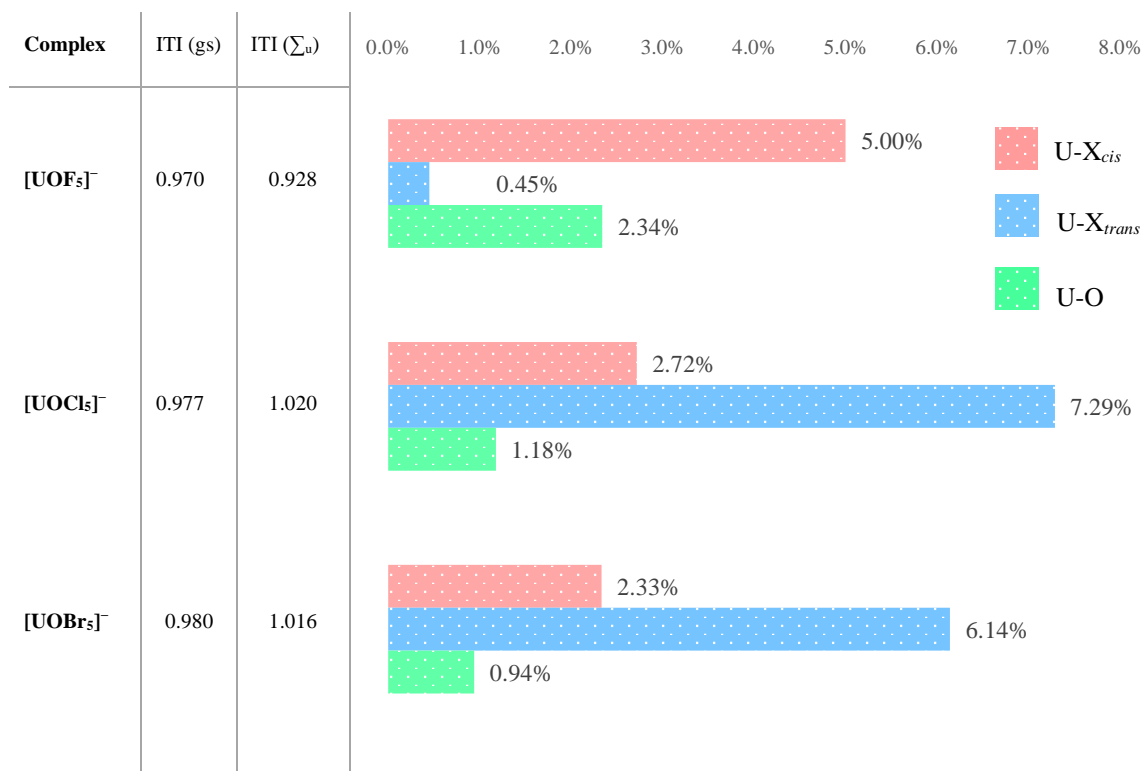
Figure 4.7. Graph showing the $\sum_u$ excited state bond lengths for the [UOX$_5$]$^-$ complexes (X = F, Cl, Br) as a percenatge increase from the ground state bond lengths, where the red bars represent the U-X$_{cis}$ bonds, the blue bars represnet the U-X$_{trans}$ bonds, and the green bars represent the U-O bonds. In addition, the magnitudes of the ITI at the gound state (gs) are shown in the far left coulmn, and at the $\sum_u$ excited state in the second column.

As shown in **figures 4.6a + 4.7**, the geometry of the [UO**F**$_5$]$^-$ complex in the $\sum_u$ state does not follow the same deformation pattern as the [UO**Cl**$_5$]$^-$ and [UO**Br**$_5$]$^-$ complexes. This is quite surprising as throughout the ground state characterisation, both QTAIM and NBO detailed how the [UO**F**$_5$]$^-$ complexes typically mirrored the [UO**Cl**$_5$]$^-$ and [UO**Br**$_5$]$^-$ complexes' behaviour qualitatively. Differently (in fact opposite to the [UO**Cl**$_5$]$^-$ and [UO**Br**$_5$]$^-$ complexes), the corresponding excitation in the [UO**F**$_5$]$^-$ results in the *cis*-bonds elongating far more significantly than the *trans*-bonds (manifesting as an **increase** in the ITI). Specifically, the U-F *cis*-bonds lengthen by 5.0% (210.5 pm in the ground state, 221.0 pm in the excited); the *trans*-bond is only lengthened by 0.5% (204.1 pm to 205.0 pm), the U-O bond lengthens by 2.4% (which is also more significant than what is observed for the UCl-$\sum_u$ and UBr-$\sum_u$ excited geometries).

The bond length changes cause the magnitude of the ITI value in the excited state geometries to deviate further from the idealised value of 1 (from 0.970 to 0.928), of which implies an **increase** in the ITI magnitude.

Referring back to the σ_u orbital depictions for the $[UOX_5]^-$ complexes (orbitals: UF-14a$_1$, UCl-19a$_1$, UBr-28a$_1$, **fig. 4.2a**), we can make reasonable assumptions as to why exciting from these orbitals' manifests with the bond length changes shown in **figures 4.6** and **4.7**. Considering the $\sum_u$ excitations for the $[UOCl_5]^-$ and $[UOBr_5]^-$ complexes (concerning MOs UCl-19a$_1$, UBr-28a$_1$ respectively), there is a clear bonding interaction between the uranium's f$_{z^3}$ lower lobe, and *trans*-ligands' p$_z$ orbital. Whereas in the $[UOF_5]^-$ complexes' UF-14a$_1$ MO, there is clear non-bonding interaction between the same orbital components. Resultantly, exciting from the bonding interaction between the U metal and the *trans*-ligand in the UCl-19a$_1$ and UBr-28a$_1$ MOs yields an increase in the bond length, whereas in the $[UOF_5]^-$ complex, there is no interaction to excite from; therefore, there is little change in the *trans*-bond length. Correspondingly, the *cis*-F ligands (in the UF-14a$_1$ MO) have a more substantial p$_z$ orbital character, relative to the UCl-19a$_1$ and the UBr-28a$_1$ MO (the latter's contribution being almost negligible). We see that this follows the trend where exciting out of the UBr-28a$_1$ MO (for the $[UOBr_5]^-$ complex) has the least significant effect in *cis*-bond lengths, followed by the $[UOCl_5]^-$ complex, and then the $[UOF_5]^-$ with the **most** significant change in *cis*-bond lengths. Alongside this, we point out that the *cis*-ligands' p$_z$ orbitals in the $[UOCl_5]^-$ and $[UOBr_5]^-$ complexes actually have inverted parity to the *cis*-ligands in the $[UOF_5]^-$ complex, and so this may affect the excitation character.

With the same reasoning, the bonding character between the lower lobe of the U-f$_{z^3}$ MO component and O-2p$_z$ lobe is **more** substantial in the UF-14a$_1$ MO, relative to that of the UCl-19a$_1$ and UBr-28a$_1$ MOs. Similarly to the *trans*-ligand interaction trend between the F, Cl and Br-complexes, the more significant U-O bonding interaction, this time, is in UF-14a$_1$ MO, and resultantly yields a more substantial increase in the bond distance relative to that of the UCl-19a$_1$, UBr-28a$_1$ MOs.

We draw focus to the small elongation of the *trans*-bond in the UF-$\sum_u$* geometry, and propose two scenarios to rationalise this: the first, excitation out of the UF-$14a_1$ MO (**fig. 4.2a**) via the F-$\sum_u$ excitation has **no** differential effect on the *trans*-bond, in which case the slight increase in bond length is a result of the 'total expansion' previously described when populating the δ_U non-bonding orbital. The second, that optimising at the UF-$\sum_u$ excitation actually causes a **decrease** in the U-F$_{trans}$ bond length which is counteracted by the population of the δ_U MO.

Figure 4.8 shows illustrations of the difference in electron densities between the ground state and the excited state for each $[UOX_5]^-$, at both the ground state geometries (left-hand side), and the excited state geometries (right-hand side). These plots were obtained using the egrad[96,97] function in TURBOMOLE[61] and plotted using the multiWFN[112] visualisation software.

For the $[UOF_5]^-$ complexes, the density difference plots at both the ground and $\sum_u$ excited state geometries (**fig 4.8**, top row) have a large focus in the *cis*-ligand positions. Comparing both geometries' density differences, the density plots in the *cis*-positions are uniform at both geometries, whereas in the *trans*-positions, there is a slight change in character at the excited geometry. As for the density difference plots of the $[UOCl_5]^-$ and $[UOBr_5]^-$ complexes (**fig 4.8** second and third rows), in the ground state geometries (LHS), compared to the $[UOF_5]^-$ complex, the densities are more heavily focused in the linear U-O-X$_{trans}$ component, relative to the equatorial *cis*-plane (with $[UOBr_5]^-$ being more significant in this respect). Alongside this, the density difference plots at the excited state geometries show a further reduction in the equatorial (*cis*-bond) plane, accompanied by a reduction of character in the U-O bonding region.

Complex	Ground State Geometry	$\sum_u$ Excited State Geometry
$[UOF_5]^-$		
$[UOCl_5]^-$		
$[UOBr_5]^-$		
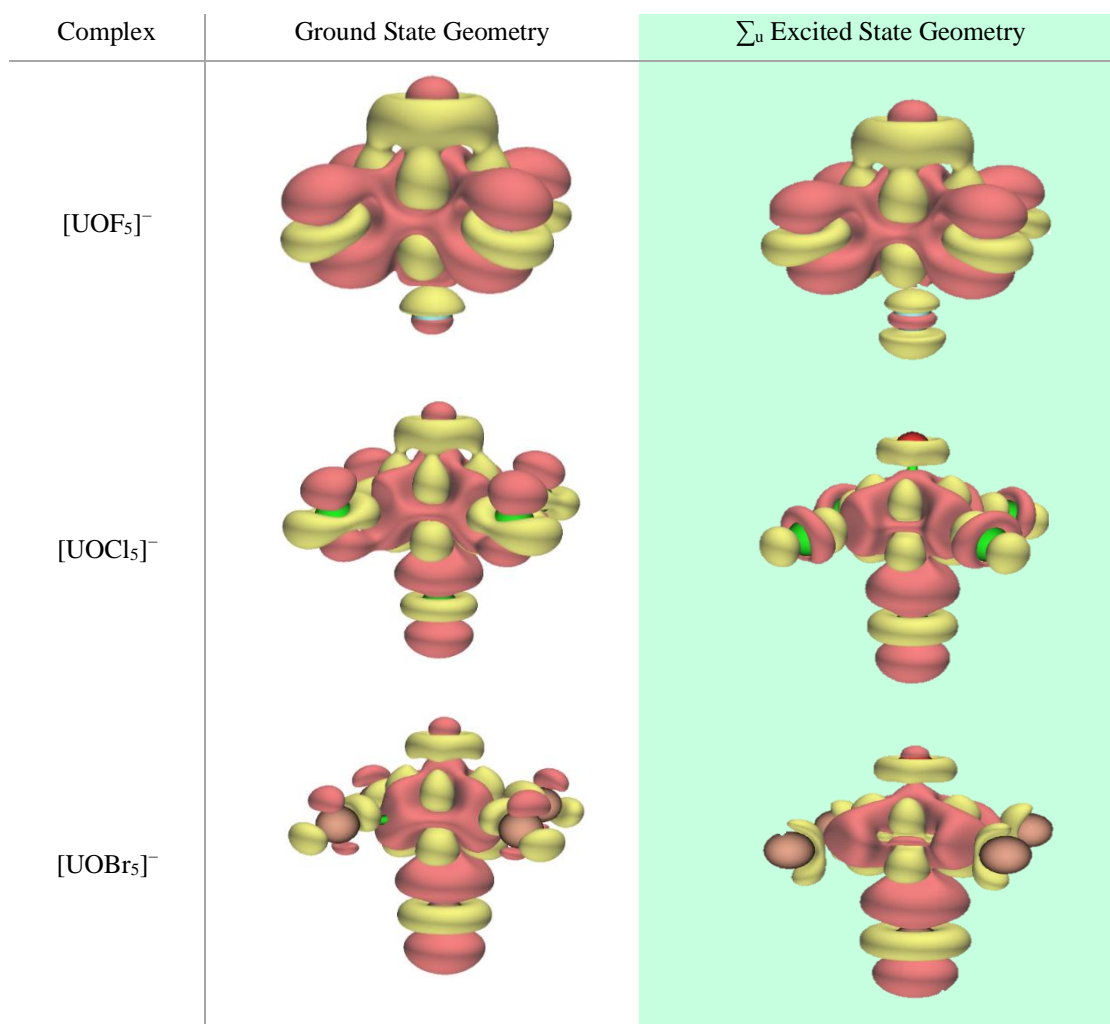
Figure 4.8. density difference plots for between ground and $\sum_u$ excited state densities for the $[UOX_5]^-$ complexes (top to bottom, X = F, Cl, Br), where the left-hand side shows the density differences at the ground state geometry; the right-hand side shows the density differences at the excited state geometry.

4.2.2. Optimising the $\Sigma_u{}^*$ excited state

The $\Sigma_u{}^*$ transitions characteristically involve exciting from *cis*-p$_{x/y}$ non-bonding MOs (**fig 4.3b**) and populating the $\sigma_u{}^*$ MOs (**fig 4.2b**). The constituent transitions of these excitations are shown in the bottom half of **table 4.1**; the left columns in **figures 4.5(a-c)** show these transitions at the new excited state geometries post-optimisation. Considering the data in **table 4.1**, the $\Sigma_u{}^*$ excitations typically have more dominant contributions of the desired $\sigma_u{}^*$ MOs than the Σ_u excitations (99.9%, 84.8% for the F, and Cl)**,** with the exception of the $[UO\mathbf{Br}_5]^-$ complex (49.2%). Referring back to **figure 4.6**, the bond lengths in picometres (pm) for $\Sigma_u{}^*$ excited state geometries of all f-block

complexes are plotted against the ground state bond lengths; additionally, **figure 4.9** shows the $\Sigma_u{}^*$ bond lengths as a percentage increase from the ground state bond lengths.
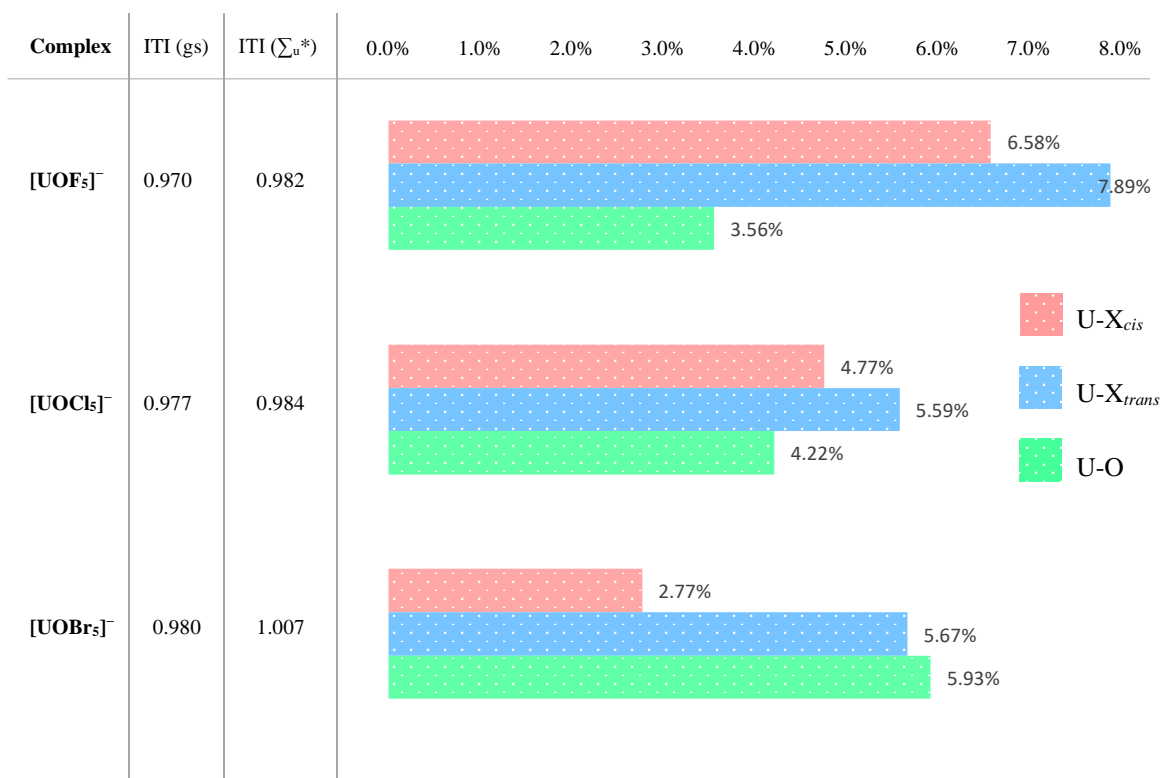
Figure 4.9. Graph showing the $\sum_u{}^*$ excited state bond lengths for the [UOX$_5$]$^-$ complexes (X = F, Cl, Br) as a percenatge increase from the ground state bond lengths, where the red bars represent the *cis*-bonds, the blue bars represnet the *trans*-bonds, and the green bars represent the U-O bonds. In addition, the ITI influence magnitudes at the gound state (gs) are shown in the far left column, and the new ITI magnitude values at the $\sum_u$ excited state in the column to the right of it.

Figure 4.6 shows that for the $\sum_u{}^*$ geometries of all [UOX$_5$]$^-$ complexes, both the *cis*- and *trans*-bond lengths increase relative to the ground state bond lengths, and that the *trans*-bond increase being more significant than the *cis*-bond increase. **Figure 4.9** shows that relative to the ground state geometry, the increase in **both** *cis*- and *trans*-bond lengths is most significant in the UF-$\sum_u{}^*$ geometry (6.6% and 7.9% increase for the *cis*- and *trans*-bonds), followed by the UCl-$\sum_u{}^*$ geometry (4.8%, 5.6%) and then the UBr-$\sum_u{}^*$geometry (2.8%, 5.7%). This trend appears to match that of the $\sigma_u{}^* \rightarrow$ U-δ transitions' contribution percentages the overall $\sum_u{}^*$ excitation, as shown in **table 4.1**, where the percentage is greatest in the UF-$\sum_u{}^*$ excitation (99.9%), and lowest in the Br-$\sum_u{}^*$ excitation (49.2%).

Figure 4.9 shows that for the $[UOF_5]^-$ and $[UOCl_5]^-$ complexes, the difference between the *cis*- and *trans*-bond increase percentages is 1.3% and 0.8%, suggesting that they increase at a fairly similar rate. This slight change in *cis*- and *trans*-bond ratios (where the *trans*-bond becomes more *cis*-like), results in the magnitude of the ITI moving closer to a value of 1, which implies a formal **decrease** in the ITI relative to the ground state (0.970 to 0.982 for the UF-$\sum_u$*and 0.977 to 0.984 for the UCl-$\sum_u$*).

As for the $[UOBr_5]^-$ complex, **figure 4.6c** shows in the UBr-$\sum_u$* optimised geometry, the *trans*-bonds lengthen almost three times the amount that the *cis*-bonds lengthen from the ground state (*trans*-bonds: +6.1%, *cis*-bonds: +2.3%). The more significantly shifted ratio of *cis*- and *trans*-bond lengths (relative to the UF-$\sum_u$* and UCl- F-$\sum_u$* geometries) results in the U-Br$_{trans}$ bond length now being greater than the U-Br$_{cis}$ (274.2 pm, 268.6 for the *cis*- and *trans*-bonds in the ground state, 277.0 pm, 282.4 pm in the UBr-$\sum_u$* geometry). Consequently, as shown in **figure 4.6c**, the UBr-$\sum_u$* geometry is redefined to exhibit a TI (on account of the plot point ascending over the idealised line). We rationalise the difference in the UBr-$\sum_u$* geometry being a result of the different MO transition contributions and magnitudes shown in **table 4.1**.

4.3. Excitations Invoking the TI and the ITI

After considering the f-block species, and by extension, the ITI exclusively, we go on to compare the f-block excitations to d-block excitations, and further, the ITI to the TI. We begin with a hypothesis that the ITI and TI originate from the same electronic effects, such that exciting from analogous MOs in the d-block species as were considered in the f-block, should therefore show a reverse or at least an interpretably opposing effect. In accordance to this, **figure 4.10** shows a revised flow chart.

1. Locate 'interesting' MOs that could play a role in the ITI	**2.** Identify corresponding MOs in all other f-block **and d-block** complexes	**3.** Excite out of (or into) the interesting MO	**4.** Allow the structure to 'relax' under a geometry optimisation at the excited state	**5.** Compare the *cis- trans*-bond ratios of the f- and d-block species post-excitation
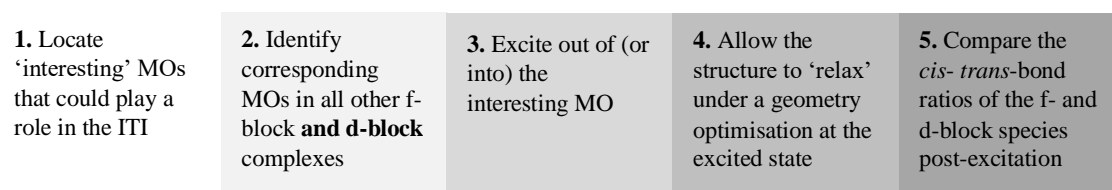
Figure 4.10. flow chart of the methodology behind the excited state calculations involving the f-block and the d-block species.

Considering tasks one and two in **figure 4.10**, the previously characterised MOs for the f-block species (σ_u and σ_u^*) are unsuitable, as the d-block species do not contain analogous occupied fz^3 orbitals. Therefore, we expand our definition of 'interesting orbitals' so as to include MOs present in both the f-block and d-block species. The most apt comparable orbital for both the f- and d-block species that incorporate the linear O-M-X$_{trans}$ feature, are the MOs centred around the metal-d_{z^2} atomic orbitals ($6d_{z^2}$ for the U, $4d_{z^2}$ for the Mo; $5d_{z^2}$ for the W). **Figure 4.11** shows these identified MOs of the a_1-type for the d-block and f-block species, as well as their orbital energies (eV). These MOs will henceforth be referred to as the σ_g MOs, in accordance with their relative *approximate* parities (no inversion centre and so no formal parity classifications).

	F	Cl	Br
[UOX₅]⁻	**12a₁** (−8.40 eV)	**17a₁** (−7.60 eV)	**26a₁** (−7.54 eV)
[MoOX₅]⁻	**9a₁** (−9.29 eV)	**14a₁** (−8.84 eV)	**23a₁** (−8.91 eV)
[WOX₅]⁻	**9a₁** (−8.07 eV)	**14a₁** (−8.84 eV)	**23a₁** (−8.55 eV)
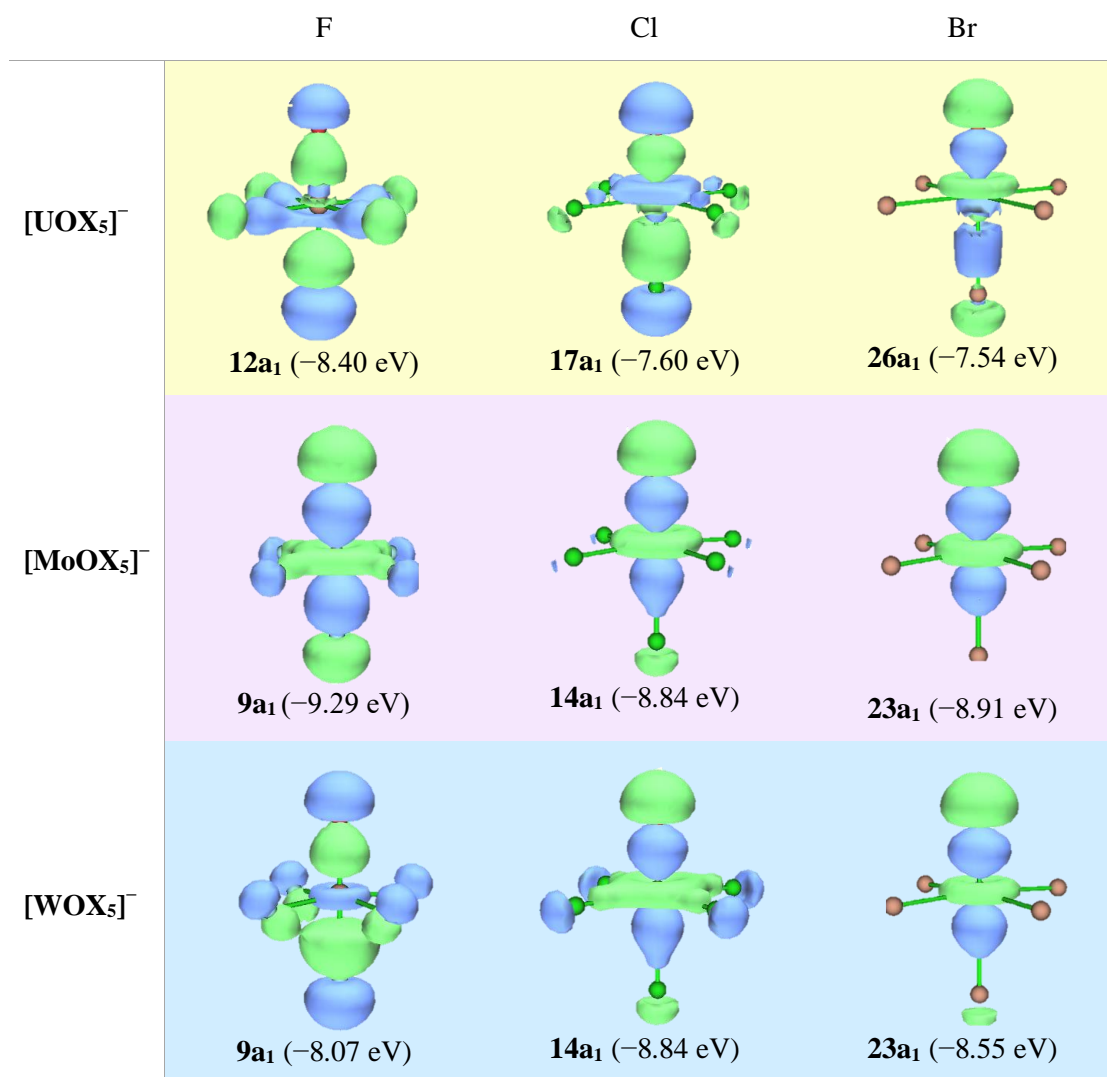
Figure 4.11. Depictions of the d_{z^2}-focused MO's for both the f-block uranium species (top row) and the d-block molybdenum and tungsten species (second and third rows respectively). The illustrations were generated using the multiWFN software package. [112] Note that the top row f-block species are highlighted in yellow, as transitions containing these MOs were previously identified in **figure 4.5**.

Figure 4.11 illustratively shows how the σ_g MOs in the f-block species (top row) in fact exhibit a mix of the d_{z^2} and f_{z^3} atomic orbitals (the former being dominant), presumably due to the similar energies and symmetry of those AOs. We also note a similar qualitative trend of both the d- and f-block σ_g MOs compared to the σ_u MOs (**figure 4.2a**), where the involvement of the *cis*-X orbitals appears to be lessened when moving from X = F to X = Cl, with the *cis*-Br ligands having essentially no contribution to the MO, this is evident in both the f-block and d-block species.

For the transitions involving the f-block species (depopulating the σ_g MOs), the same virtual δ_U MOs (**figure 4.3a**) previously utilised in the $\sum_u$ excitations are used again here. As for the d-block species, we identify a similar non-bonding MO to take part in these excitations; this orbital is illustrated in **figure 4.12.** Due to its similarity to the d_{xy} atomic orbital, we will refer to this MO as the d_{xy} MO for the remainder of this project.
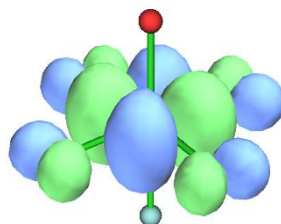
Figure 4.12. The non-bonding d_{xy} MO, a virtual orbital that becomes occupied upon excitation out of the d-block σ_g MOs.

Similarly to the comments made about the non-bonding *cis*-$p_{x/y}$ MOs used for the $\sum_u$* excitations (**fig. 4.3b**), the non-bonding d_{xy} orbital (**fig. 4.12**) has contributions from the *cis*-ligands but not from the *trans*-ligand. We would expect that populating this MO would increase the electronic charge on the equatorial ligands unequally compared to the axial ligands, likely resulting a slight uneven lengthening of the *cis*-bonds relative to the *trans*-bonds.

The first 20 b_1 vertical excitations in each $[MOX_5]^-$ complex were considered; the desired Σ_g excitations involving the MO transitions $\sigma_g \rightarrow \delta_U$ (for the f-block species) and $\sigma_g \rightarrow d_{xy}$ (for the d-block species) were identified, table **4.2** shows the results.

Table 4.2. the Σ_g excitations at the ground state geometry that predominantly involve depopulating the σ_g MOs (shown in bold) are presented as a sum of the dominant contributions and excitation energies.

Excitation	Complex	B_1 vector	Ex. energy / eV	Contributions	$\lvert$Coeff.$\rvert^2 \times 10^2$
UF-Σ_g	[UOF$_5$]$^-$	**6**	4.627	**14a$_1$ → 3b$_1$**	89.4
				10e → 12e	4.2
UCl-Σ_g	[UOCl$_5$]$^-$	**7**	3.013	**19a$_1$ → 4b$_1$**	48.7
				14e → 16e	28.0
				13e → 16e	10.7
				20a$_1$ → 4b$_1$	4.8
UBr-Σ_g	[UOBr$_5$]$^-$	**7**	2.651	**28a$_1$ → 8b$_1$**	44.5
				24e → 27e	30.2
				25e → 27e	13.2
				25e → 28e	8.1
MoF-Σ_g	[MoOF$_5$]$^-$	**16**	6.85	**9a$_1$ → 2b$_1$**	73.7
				10a$_1$ → 2b$_1$	12.4
				4e → 9e	12.2
MoCl-Σ_g	[MoOCl$_5$]$^-$	**9**	5.024	**14a$_1$ → 3b$_1$**	72.3
				9e → 14e	26.9
MoBr-Σ_g	[MoOBr$_5$]$^-$	**9**	4.591	**23a$_1$ → 7b$_1$**	63.8
				20e → 25e	35.6
WF-Σ_g	[WOF$_5$]$^-$	**8**	7.575	**9a$_1$ → 2b$_1$**	92.8
WCl-Σ_g	[WOCl$_5$]$^-$	**9**	5.573	**14a$_1$ → 3b$_1$**	79.7
				9e →145e	11.1
WBr-Σ_g	[WOBr$_5$]$^-$	**9**	5.074	**23a$_1$ → 7b$_1$**	82.5
				20e → 25e	14.5

Using the same optimisation procedure outlined in the f-block exclusive section, **figure 4.13** shows the *cis-* and *trans-*bond lengths (in pm) at both the ground state, and Σ_g excited state geometries of the [UOX$_5$]$^-$ complexes, where X = F (**fig**. **4.13a**), Cl (**fig**. **4.13b**), and Br (**fig**. **4.13c**). The shaded region signifies species exhibiting a ITI; the non-shaded region signifies a species exhibiting a TI. The numerical data for these plots is provided in the supplementary information, **section 7**, **table 7.3**. Additionally, **figure 4.14** presents the excited state bond lengths as percentage changes from the ground state bond lengths.
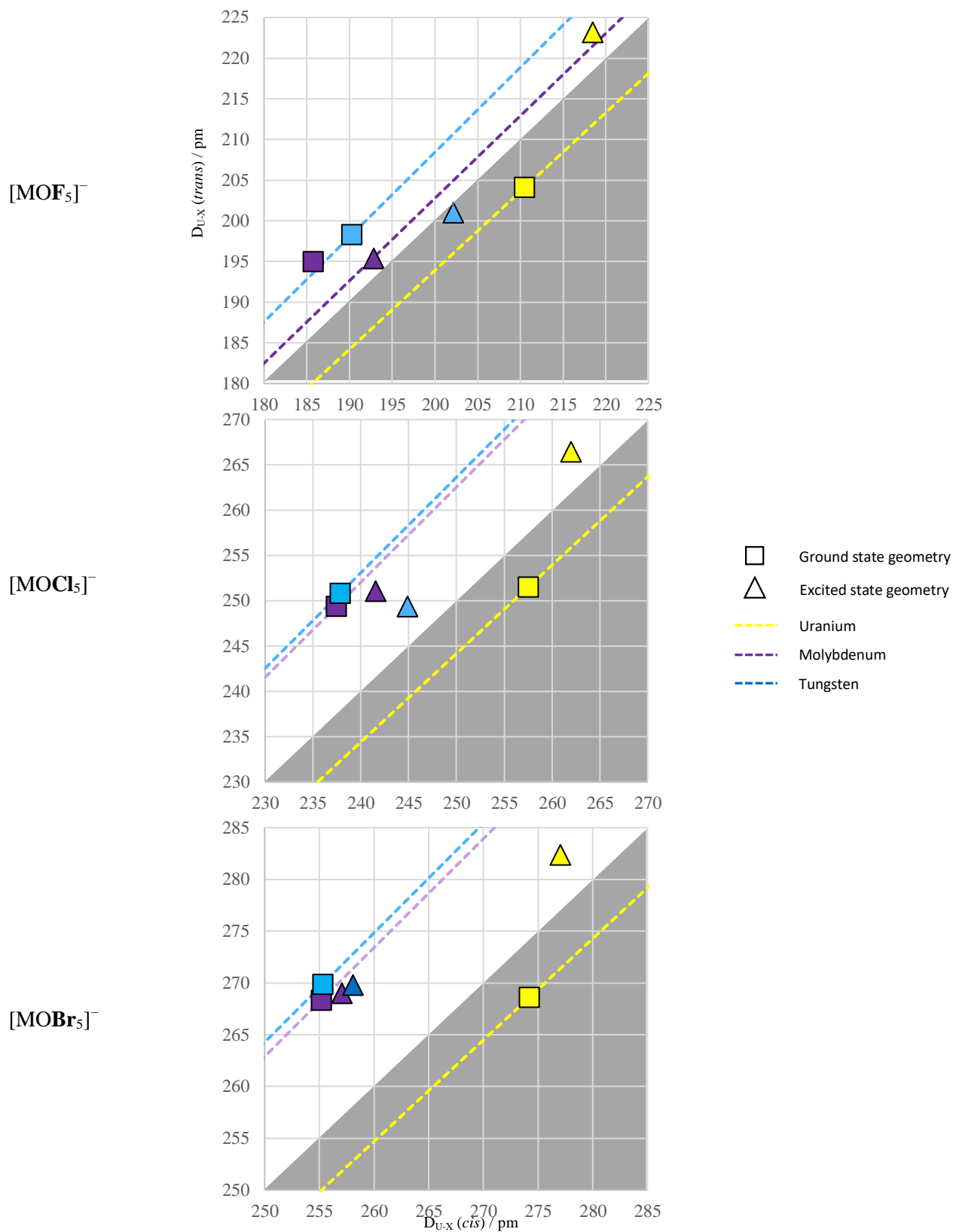
Figure 4.13a-c. Plot of the *cis-* (x-axis) and *trans*-bond (y-axis) lengths in pm of the [MOX$_5$]$^-$ complexes at both the ground (square markers) and $\sum_g$ (triangle markers), where X = F (top, **fig 4.6a**), Cl (middle, **fig 4.6b**), and Br (bottom, **fig 4.6c**), M = U (yellow), Mo (purple), W (blue).

Complex	ITI/TI (gs)	ITI/TI ($\sum_g$)		
[UOF₅]⁻	0.970	1.022	cis 3.76% / trans 9.36% / M-O 1.88%	
[UOCl₅]⁻	0.977	1.017	cis 1.74% / trans 5.96% / M-O 6.89%	
[UOBr₅]⁻	0.980	1.019	cis 1.03% / trans 5.13% / M-O 8.80%	
[MoOF₅]⁻	1.055	1.013	cis 3.78% / trans 0.20% / M-O 11.26%	
[MoOCl₅]⁻	1.050	1.040	cis 1.72% / trans 0.69% / M-O 8.11%	
[MoOBr₅]⁻	1.052	1.047	cis 0.73% / trans 0.25% / M-O 10.56%	
[WOF₅]⁻	1.042	0.995	cis 6.22% / trans 1.38% / M-O 0.95%	
[WOCl₅]⁻	1.055	1.018	cis 2.95% / trans -0.58% / M-O 4.97%	
[WOBr₅]⁻	1.057	1.046	cis 1.07% / trans -0.03% / M-O 8.00%	

Figure 4.14. Graph showing the $\sum_g$ excited state bond lengths for the [MOX₅]⁻ complexes (X = F, Cl, Br and M = U, Mo, W) as a percenatge increase from the ground state bond lengths, where the red bars represent the *cis*-bonds, the blue bars represent the *trans*-bonds, and the green bars represent the U-O bonds. In addition, the influence percentages of the gound state are shown in the far left coulmn, and the new influence percentages at the $\sum_g$ excited state are shown in the column to the right.

A point to note, the TI, as previously defined is an elongation of the bond opposite a strong σ-donor relative to the remaining *cis*-ligands, characteristic in d-block complexes.[1] The ITI is the opposite, a shortening of the *trans*-bond opposite a σ-donor, typically only observed in f-block complexes.[7] For this section, we loosen these definitions slightly so that they are not exclusive to their particular element block in the periodic table. This effectively positions the ITI and TI on a dynamical scale, where the ITI is dominates when the *trans*-bond lengths are **shorter** than the *cis*-bond lengths, and the TI dominates when the *trans*-bond lengths are **longer** than the *cis*-bond lengths, irrespective of the central cation's location on the periodic table.

4.3.1. $\sum_g$ Optimizations for the X = F Complexes

For the $[MOF_5]^-$ complexes (M = U, Mo, W), considering the f-block $[UOF_5]^-$ species, **figures 4.13a** and **4.14** show that optimising at the UF-$\sum_g$ excitation (characteristically exciting out of the UF-σ_g MO and into the δ_U MO) results in a reversal of the ITI on account of the lengths of the *trans*-bonds now being greater than the *cis*-bonds (218.4 pm, and 223.3 pm, increasing by 3.8% and 9.4% respectively from the ground state, **fig. 4.14**). Interestingly, in the d-block $[WOF_5]^-$ complex, optimising the analogous $\sum_g$ excitation concerning the WF-$\sigma_g \rightarrow d_{xy}$ transition, results in a reversal of the TI on account of the *cis*-bond lengths now being greater than the *trans*-bond lengths (202.1 pm and 201.1 pm, increasing by 6.2% and 1.4% from the ground state). Therefore, optimising the geometry after exciting out of the σ_g MO for the $[UOF_5]^-$ redefines the structure as exhibiting a TI, whereas the analogous excited state in the d-block $[WOF_5]^-$ species redefines the structure as exhibiting an ITI.

The analogous excited state geometry for the d-block $[MoOF_5]^-$ species is qualitatively similar to the $[WOF_5]^-$ species, where the TI is **reduced** from 1.055 to 1.013, on account of the *cis*-bond lengths increasing by 3.8% (185.8 pm to 192.8 pm), and the *trans*-bonds lengths staying relatively uniform; only increasing by 0.2% (195.0 pm to 195.4 pm). Differently to the WF-$\sum_g$ geometry however, the change in bond length ratio is not enough to classify the structure as now exhibiting an ITI, as shown in **figure 4.13a,** the **W**F-$\sum_g$ geometry is plotted in the shaded region, whereas the **Mo**F-$\sum_g$ geometry is not, and stays on the TI-side of the plot.

The slight increase in the *trans*-bond lengths could be considered a result of populating the metal-centred non-bonding d_{xy} MO (**fig. 4.12**); in which case we could argue that optimising at the $\sum_g$ excitation for the [**MoOF$_5$**]$^-$ species has either **no** effect of the *trans*-bond lengths, or the *trans*-bond lengths are actually decreased from the ground state (which is counteracted by the expansion caused from populating the d_{xy} MO). A similar reasoning may be applied for optimising at the $\sum_g$ excitation for the [**WOF$_5$**]$^-$ species, but not for the f-block [**UOF$_5$**]$^-$ complex (UF-$\sum_g$ excitation) due to the more significant change in *trans*-bond length, suggesting a more deliberate effect.

4.3.2. $\sum_g$ Optimizations of the X = Cl and Br Complexes

Turning our attention to the [MOCl$_5$]$^-$ complexes, where M = U, Mo, and W. For the [**UOCl$_5$**]$^-$ complex, optimising at the UCl-$\sum_g$ excitation, similarly to the UF-$\sum_g$ analogue, results in the ITI **decreasing** and resultantly switching to a TI (as shown in **figure 4.13b**), a manifestation of the *trans*-bond elongating more significantly than the *cis*-bonds. Specifically, the *trans*-bond length increases by 15.0 pm (6.0% increase from the ground state *trans*-bond), and the *cis*-bonds lengthen by a less pronounced 4.5 pm (1.8% from the ground state geometry); this ratio-shift results in the ground state ITI magnitude value ascending over the idealised value of 1, from 0.977 to 1.017; redefining the structure as TI-exhibiting.

For the d-block [**MoOCl$_5$**]$^-$ and [**WOCl$_5$**]$^-$ species, optimising the analogous $\sum_g$ excitations (concerning the $\sigma_g \rightarrow d_{xy}$ MO transitions) results in a **decrease** of the TI. For the **Mo**Cl-$\sum_g$ geometry, the *trans*-bond length remains similar to the ground state bond length (only lengthening by only 0.7 pm), whilst the *cis*-bond lengths lengthen more significantly (increasing by 4.0 pm, or 1.70% from the ground state). Resultantly, this causes the TI of the [**MoOCl$_5$**]$^-$ species to reduce from 1.050 to 1.040.

A similar (but more prominent) trend is shown in the [**WOCl$_5$**]$^-$ complex, the *cis*-bonds lengthen by 7.0 pm (3.0% increase from the ground state), and remarkably, the *trans*-bond actually **shortens** by 1.5 pm (−0.6% decrease from ground state *trans*-bond). Overall, this results in the TI magnitude value of the [**WOCl$_5$**]$^-$ complex reducing from its ground state value of 1.055, to the excited state geometry value of 1.018.

As previously mentioned, when populating a non-bonding orbital such as the d_{xy} MO (**fig. 4.12**), we would expect a 'total expansion' of the molecules bond length (directional in the *cis*-bonds). This suggests that the *trans*-bond length actually decreasing when optimising the WCl-$\sum_g$ excitation in the [**WOCl₅**]⁻ complex (out of the WCl-σ_g and into the d_{xy} MO), is most likely competing with this 'total expansion.' Furthermore, this implies that exciting to the WCl-$\sum_g$ state and optimising may actually result in the *trans*-bond **contracting** more significantly than what is shown in **figures 4.13b** and **4.14**.

Figures 4.13c and **4.14** show that the $\sum_g$ excited state geometries of the [**MOBr₅**]⁻ complexes closely match that of the [**MOCl₅**]⁻ complexes. For example, in the f-block species, similar to the UCl-$\sum_g$ optimisation, optimising at the U**Br**-$\sum_g$ state causes a reversal of the ITI into a TI (0.980 in the ground state, 1.019 in the excited state), a result from the *trans*-bonds lengthening more significantly (5.1% increase from the ground state lengths) than the *cis*-bonds (1.0% increase). In the d-block [**MOBr₅**]⁻ species (M = Mo, W), the magnitudes of the TI decreases (1.052 to 1.047 for the Mo; 1.057 to 1.046 for the W), pushing them closer in the ITI direction, although not as significantly as the changes in the [**MOCl₅**]⁻ complexes. We also point out that similar to the [**WOCl₅**]⁻ complex, the *trans*-bond in the [**WOBr₅**]⁻ complex **shortens** relative to the ground state geometry (by a much less significant 0.03% however).

4.3.3. $\sum_g$ Optimizations and the M-O bond

Considering **figure 4.14**, for the [**UOX₅**]⁻ and [**MoOX₅**]⁻ species, we note that the percentage increase (from the ground state bond length) of the M-O bond length is opposite in magnitude to the percentage increase of the *trans*- and *cis*-bond lengths. The *cis*-bonds can be rationalised if we consider the steric and repulsive effects of moving an O-ligand closer to the metal centre. As for *trans*-bonds, we have previously mentioned the dependence of the TI and ITI on the M-O bond lengths. Typically, for the ITI-exhibiting [UOX₅]⁻ complexes, a shorter U-O bond is accompanied by a shorter *trans*-bond, and resultantly, greater ITI (defied by a magnitude value). We see from **figure 4.14** that this is not the case here, a shorter U-O bond length results in a greater *trans*-bond length and less prominent (closer to 1) ITI. For TI-exhibiting [MOX₅]⁻

complexes (M = Mo, W), in the ground state, a shorter M-O bond distance results in a lengthened *trans*-bond, that manifests as an increase TI magnitude; clearly this is still the case in the $\sum_g$ excited state geometries.

To summarise, for all halogen types in the f-block species, exciting out of the σ_g MOs results in the *trans*-bonds lengthening more significantly than the *cis*-bond lengths; ultimately redefining the excited state structure to exhibit a regular *trans*-influence. As for the d-block species, exciting out of the analogous σ_g MOs results in *cis*-bonds lengthening more significantly than the *trans*-bonds (in the case of the $[WOCl_5]^-$ complex, the *trans*-bond actually contracts slightly). Overall this results in a decrease of the TI from the typical ground state values of 1.05 to the excited state values of 1.01; particular attention is drawn to the $[WOF_5]^-$ complex, where in the excited state, the *cis*- and *trans*-bond ratio is calculated to be 0.995, implying the species now marginally exhibits an ITI (instead of a TI).

Chapter 5

Conclusions + Further work

5.1 Conclusions at the Ground State

The research in this project aimed to elucidate the conventional ITI and TI in a series of several complexes, of the form $[MOX_5]^-$ (where M = U, Mo, W and X = F, Cl, and Br). It also considers the impact of electronic excitation on the magnitude and nature of these influences.

For the ground state, based on DFT calculations, three separate analyses were used to characterise the TI and ITIs in the $[MOX_5]^-$ complexes: bond length (via geometry optimisations), QTAIM, and NBO, all of which mostly agreed with each other. Through bond length analysis, we confirm that the ITI in the f-block $[\mathbf{U}OX_5]^-$ species manifests as the U-X$_{trans}$ (opposite to the O-ligand) **shortening**, typically by around 2.9% relative to the U-X$_{cis}$ bonds. For the TI, we show that in the d-block $[MOX_5]^-$ species (M = Mo, W), the M-X$_{trans}$ bond is **lengthened** by around 5.0% for the $[\mathbf{Mo}OX_5]^-$ species, and 5.1% for the $[\mathbf{W}OX_5]^-$ complexes, relative to the M-X$_{cis}$ bonds. We treat the bond length differences as a ratio, which provides a generalised measure of the magnitude of the influences, where greater deviations above (TI) or below (ITI) an idealised value of 1 indicate a greater magnitude. Considering this measure with the f-block $[\mathbf{U}OX_5]^-$ complexes, the $[UO\mathbf{F}_5]^-$ species have the greatest magnitudes, followed by the $[UO\mathbf{Cl}_5]^-$ and the $[UO\mathbf{Br}_5]^-$ species. For the d-block $[\mathbf{Mo}OX_5]^-$ complexes, the $[MoO\mathbf{F}_5]^-$ species have the greatest magnitudes, followed by the $[MoO\mathbf{Cl}_5]^-$ and then the $[MoO\mathbf{Br}_5]^-$ species (the same ordering as the f-block), and for the d-block $[\mathbf{W}OX_5]^-$ complexes, the $[MoO\mathbf{Cl}_5]^-$ species have the greatest magnitudes, followed by the $[MoO\mathbf{F}_5]^-$ and then the $[MoO\mathbf{Br}_5]^-$ species.

In all cases, the $[MO\mathbf{Br}_5]^-$ species have the least differential between the *cis-* and *trans-* bond lengths. Additionally, using the optimised ground state complexes, we rationalise the TI and ITI magnitudes as a function of the M-O bond, finding that the ITI and TI magnitudes scale inversely with the length of the M-O bond.

Intrinsic properties, most of which relate to the degree of covalency in the *cis-* and *trans-*bonds, are discussed using two approaches: a topological QTAIM approach, and bond-orbital NBO approach. Considering the first approach: Charactering the ITI-exhibiting [**UOX$_5$**]$^-$ complexes using BCP metrics, we show that the relative **shortening** of the *trans-*bond (compared to the *cis-*bonds) is accompanied by an increased degree of overlap-driven covalency, on account of the higher ρ_b values. Using integrated DI metrics, we observe that the degree of electron-sharing in the *trans-*bond is greater than the *cis-*bonds (on account of higher $\delta(\mathrm{U, Br}_{trans})$ values relative to the $\delta(\mathrm{U, Br}_{cis})$ values). This suggests that the increased covalency in the *trans-*bonds relative to the *cis-*bonds for the [**UOX$_5$**]$^-$ complexes (X = F, Cl, Br), is predominantly overlap-driven in nature. Correspondingly, QTAIM characterisation of the analogous d-block, TI-exhibiting [**MOX$_5$**]$^-$ complexes (M = Mo, W) afforded qualitatively similar results. The **lengthened** *trans-*bonds had both lower ρ_b and $\delta(M, X_{trans})$ values relative to the *cis-*bonds. This suggests a lower degree of overlap-driven covalency and electron-sharing in the M-X*trans* bonds relative to the M-X*cis* bonds, the opposite of what is shown in the ITI-exhibiting [**UOX$_5$**]$^-$ species.

For the Laplacian of the BCP electron density $\nabla^2\rho_b$, we opt to use an interpretation[125] where the higher values imply higher bond polarisation. With this in mind, we see that in the f-block [**UOX$_5$**]$^-$ complexes, the U-F bond(s) are the **most** polarised, followed by the U-O, U-Cl, and then the U-Br bonds, which matches the trends of electronegativity. For the d-block [**MOX$_5$**]$^-$ complexes, the M-O bonds are most polarised, followed by the M-F, M-Cl and M-Br. We provide a rationalisation for this using HSAB principles.[143,146]

Considering the [**MOX$_5$**]$^-$ species as a function of ligand X, QTAIM analysis showed that for both f- and d-block, the degree of overlap-driven covalency (measured by the ρ_b metric), was greatest in the [**MOF$_5$**]$^-$ species, followed by the [**MOCl$_5$**]$^-$ and then the [**MOBr$_5$**]$^-$ species (with the latter two being similar). However, analysis of the $\delta(M, X)$ values showed the reverse trend, where the $\delta(M, \mathbf{Br})$ was greatest, followed by $\delta(M, \mathbf{Cl})$, and $\delta(M, \mathbf{F})$. This suggests that the overlap-driven covalencies, on account of the ρ_b values, and energy-driven covalencies on account of the $\delta(M, X)$ values, scale opposingly for increasing halogen number (F to Br). To clarify, the M-F bonds (from

the d- and f-block [M**O**F$_5$]$^-$ complexes) have the **highest** order of overlap-driven, but **lowest** order of energy-driven covalency, and the M-Br bonds (from the [M**O**Br$_5$]$^-$ complex) have the **lowest** order of overlap-driven, but **highest** order of energy-driven covalency.

Using NBO analysis, we have characterised the U-O, U-X$_{cis}$ and U-X$_{trans}$ bonds in terms of ligand X and U-metal contributions for each of the ITI-exhibiting [UOX$_5$]$^-$ complexes. On account of greater contribution from the cation, the order of covalency in the U-X goes Br > Cl > F. This agrees with the $\delta(U,X)$ metrics from the QTAIM analysis but disagrees with the ρ_b values (that showed the overlap-driven covalency increased in the order of F > Cl > Br). This suggested that the NBO characterisation was more akin to measuring the energy-driven covalency than the overlap-driven.

Comparing the U-X$_{cis}$ and U-X$_{trans}$ bonds defined by NBO for all halogen derivatives, the *trans*-bonds have a higher order of bond covalency relative to the *cis*-bonds. Furthermore, analysis of the bond orbitals of the U's contributions tells us that the greater covalency in the *trans*-bonds, compared to the *cis*-bonds is motivated predominantly, by an increase in d- and s-orbital (with a simultaneous but lesser decrease in f-orbital) characters. The [UOX$_5$]$^-$ complexes were compared to their analogous UX$_6$ complexes. The NBO data for the *cis*-bonds in the [UOX$_5$]$^-$ complexes, where X = Cl, and Br, shows similarities to the corresponding UX$_6$ bonding, whereas the *trans*-bonds show increased U-contribution, mediated by an increase in d- and s-orbital, and decrease in f-orbital character. For X = F however, the *cis*- and *trans*-bonds in the [UOF$_5$]$^-$ complex **both** had lower U-contributions than the U-F bonds in UF$_6$ complex, but with the *cis*-bonds being significantly lower.

Overall, in terms of NBO characterisation in the [**U**OX$_5$]$^-$ complexes, for X = F, Cl, and Br, the change in covalency of the *trans*-bond (in accordance to the ITI, and characterised by QTAIM) can be accounted for by increased d- and s- orbital contributions, and decreased f-orbital contributions from the U-species.

The NBO analysis of the d-block $[\mathbf{W}OX_5]^-$ species was inconclusive. It was found that the structures did not conform to the Lewis arrangements required by NBO as expected. For the $[\mathbf{Mo}OX_5]^-$ complexes, only the X = Br and Cl derivatives could be characterised. In the $[MoOCl_5]^-$ and $[MoO\mathbf{Br}_5]^-$ complexes, expectantly for the TI, the NBO analysis characterised the *trans*-bonds as being less covalent than the *cis*-bonds, on account of lower Mo-contributions. Interestingly, the decrease in *trans*-bond covalency was shown to be motivated by a decrease in the s- and d-orbital character. Therefore, we conclude that the **increase** in *trans*-bond covalency in the ITI-exhibiting $[\mathbf{U}OCl_5]^-$ complexes is driven by an **increase** in d- and s-orbital characters (as well as a decrease in f-orbital character), and the **decrease** in *trans*-bond covalency in the d-block $[\mathbf{Mo}OX_5]^-$ complexes (X = Cl, Br), is appropriately driven by a **decrease** in d- and s-orbital characters.

To summarise the ground state analysis, we have shown that for the $[MOX_5]^-$ complexes, the M-X bond lengths typically scale inversely with covalency, where shorter bonds have higher degrees of overlap-driven covalency and lower degrees of bond polarisation. This applies directly to the relative shortenings/lengthening of the *trans*-bond in the ITI/TI-exhibiting $[MOX_5]^-$ complexes. We show that in all of the $[MOX_5]^-$ complexes considered, the X = F species have the highest magnitudes of TI (for the d-block species) and ITI (for the f-block species), which can be rationalised by the higher orders of overlap-driven covalency in the M-F bonds relative to the other halogens (despite having lower orders of energy-driven covalency, characterised by QTAIM delocalisation indices).

5.2 Conclusions from the Excited states

The influence of electronic excitation (using TD-DFT) was considered for the d- and f-block $[MOX_5]^-$ complexes, with the intent to identify key molecular orbitals (MO) that have contributory or defining roles in the TI and ITI. The excited state analysis was divided into two parts: excited states of the ITI in the f-block $[\mathbf{U}OX_5]^-$ species, and excited states of both the ITI **and** the TI across the d- and f-block $[MOX_5]^-$ species. The former primarily focused on transitions involving MOs with U-fz^3 character (that we label as σ_u MOs), whose occupation is exclusive to the f-block complexes; the latter focused on transitions involving MOs with M-dz^2 character (for M = U, Mo , and W, that we label σ_g), which are occupied in both d- and f-block species. For the $[MOX_5]^-$ complexes, with C_{4v} symmetry, low-lying transitions pertaining to the desired MOs were identified from the first 20 B_1 singlet vertical excitations in the relevant excited states. Following this, the complexes were optimised geometrically, and the structural effect (pertaining to the ITI/TI) of populating or depopulating the selected MOs was assessed.

The excited state analysis of the f-block exclusive excitations was also subdivided based on the character of the transition: the first involved *depopulating* the σ_u MOs, and the second involved *populating* the analogous σ_u* antibonding orbital. For the former, optimising the $[UOX_5]^-$ geometries post-excitation (where X = Cl, and Br) resulted in the *trans*-bond lengths increasing by roughly 7.0% relative to the ground state, and the *cis*-bond lengths increasing by around 2.5%. Resultantly, at the excited state geometries (for the $[UO\mathbf{Cl}_5]^-$ and $[UO\mathbf{Br}_5]^-$ complexes), the *trans*-bond lengths were now **greater** than the *cis*-bonds, which effectively redefined the structures as exhibiting a TI at the excited state geometries. Differently for the $[UO\mathbf{F}_5]^-$ species, the *cis*-bonds lengthened more significantly (5.0% from the ground state) than the *trans*-bonds (0.5%), this shift in bond ratios resulted in an **increase** in the ITI. We provide elucidation into the variances between the $[UO\mathbf{F}_5]^-$ species and the $[UO\mathbf{X}_5]^-$ species (where X = Cl, Br), suggesting they arise from the differences in the character of the MO. Specifically the *trans*-ligand's pz orbital component in the $[UO\mathbf{F}_5]^-$ complex, relative to the X = Cl, and Br derivatives, has less significant interaction with the U-fz^3 orbital component. In addition, in the $[UO\mathbf{F}_5]^-$ species, the *cis*-ligand's pz orbital components have inverted

polarities compared to the same components in the $[UOCl_5]^-$ and $[UOBr_5]^-$ species, which provides some justification to their *opposite* behaviour when depopulated.

Exciting **into** the σ_u^* antibonding orbital (that has strong U-fz^3 antibonding character), involved depopulating a non-bonding, occupied MO centred around the U-species. Post-excitation, the geometries of the three halide derivatives of the $[UOX_5]^-$ species were qualitatively the same, where the *cis-* and *trans*-bond lengths both increased relative to the ground state; the latter of which was more significant. The *cis*-bond elongation was greatest in the $[UOF_5]^-$ complex, followed by the $[UOCl_5]^-$ and $[UOBr_5]^-$ complex; the *trans*-bond elongation was greatest in the $[UOF_5]^-$ complex, followed by $[UOBr_5]^-$ and $[UOCl_5]^-$ (which had near-identical bond increase percentages). We rationalise the bond length increase percentages by referring to the percentage contributions the specific orbital transitions make to the overall excitation, where the $[UOF_5]^-$ complex has the highest contribution from its σ_u^* transition (over 99%), followed by the $[UOCl_5]^-$ (85%) and the $[UOBr_5]^-$ (49%). Overall, this change in bond length ratios manifested as a decrease in the ITI; the $[UOBr_5]^-$ complex was the only species in which the *trans*-bonds were elongated significantly enough so that they were greater than the *cis*-bonds, causing a reversal of the ITI into a TI.

Overall for the f-block species exclusively, depopulating the σ_u MO in the f-block $[UOX_5]^-$ species (where X = Cl, and Br) resulted in a reversal of the ITI, redefining the structure to exhibit a TI, and for the X = F species, the ITI was increased. Populating the corresponding σ_u^* antibonding orbitals similarly resulted in the ITI changing to a TI; this was the case across all halide derivatives.

Considering the excited state analysis of both the d- and f-block species, for the f-block $[\mathbf{U}OX_5]^-$ complexes, the considered transitions involved depopulating the σ_g MO, and populating the U-centred non-bonding UΔ virtual. The analogous transition for the d-block $[MOX_5]^-$ complexes (M = Mo, and W), the transitions involved populating a M-centred non-bonding orbital that resembled the d_{xy} atomic orbital. Comparing the f-block $[\mathbf{U}OX_5]^-$ excited state geometries to the ground state geometries, we found that for all halide derivatives, there was an increase of both the *cis-* and *trans*-bond lengths; the latter being more significant, enough so that the *trans*-bond lengths became longer

than the *cis*-bond lengths at the excited state geometries, thereby switching to exhibit a TI. In terms of this effect as a function of ligand, the U-F bonds (both *cis-* and *trans-*) in the [UO**F**$_5$]$^-$ complex are elongated most substantially, followed by the U-Cl and U-Br (in the [UO**Cl**$_5$]$^-$ and [UO**Br**$_5$]$^-$ complexes respectively); additionally, the magnitudes of these new 'TIs' also follow in this order, where the [UO**F**$_5$]$^-$ complex has the most pronounced magnitude of the TI, and the [UO**Br**$_5$]$^-$ the least pronounced.

For the analogous excitation in the d-block [MOX$_5$]$^-$ species (M = Mo, W), the geometries at the excited states were qualitatively the same for all d-block complexes, where the *cis*-bonds elongated to a greater extent than the *trans*-bonds (opposite to what was shown in the f-block excitations). This shift in bond ratios resulted in a **decrease** of the TI magnitude. The [**W**O**X**$_5$]$^-$ complex was the only species where the *trans*-bond lengthening was significant enough that it became greater than the *cis*-bonds in length, redefining the structures as ITI-exhibiting. For both d-block species, the *cis*-bond elongation was greatest in the F-based complexes, and lowest in the Br-based complexes. As for the *trans*-bonds, in the [**Mo**O**X**$_5$]$^-$ complexes, the *trans*-bond elongation was greatest in the [MoO**Cl**$_5$]$^-$ species, followed by [MoO**Br**$_5$]$^-$ and [MoO**F**$_5$]$^-$ species. In the [**W**O**X**$_5$]$^-$ species, the *trans*-bond elongate from the ground state for the [WO**F**$_5$]$^-$ species, but in the [WO**Cl**$_5$]$^-$ and [WO**Cl**$_5$]$^-$ species, we found that they actually **decrease** from the ground state bond lengths (by 0.6% and 0.05% for X = Cl, and Br respectively). This decrease seems to suggest that a *trans*-bond contraction is intrinsic to the optimisations at this excited state in the [WO**X**$_5$]$^-$ species (X = Cl, Br).

Excitations involving the σ_g MO showed comparable trends in the d- and f-block species, where optimising in the excited states resulted in the *cis*- and *trans*-bond lengths becoming more alike for both the d- and f-block species. Comparing the excited geometries to the ground state geometries, in the f-block complexes, the *trans*-bond lengthened more significantly than the *cis*-bonds, which reversed the ITI, whereas in the d-block species, the *cis*-bonds lengthened more significantly than the *trans*-bonds, lessening the TI.

Revisiting Denning's[7] polarisation model, whereby the σ-donor's polarisation of the metal centre, manifests in two ways: dipolar, where charge build-up occurs in the *trans*-bond, causing it to lengthen (TI, d-block species), and quadrupolar, where charge build-up occurs in the *cis*-bonds, causing them to lengthen (ITI, f-block species). The manifestations of these effects are shown to be reversed upon excitation out of the σ_g MOs identified in both the d- and f-block species. In the TI-exhibiting d-block species, upon excitation, the *cis*-bonds are lengthened relative to the *trans*-bonds, similar to a quadrupolar effect. In the ITI-exhibiting f-block species, upon excitation, the *trans*-bonds are lengthened relative to the *cis*-bonds, similar to a dipolar effect.

Of the two main MO types considered here, the σ_g MOs appear to have a more useful and clear-cut implementation into reversing the relative influences than the σ_u MOs. Not only are these MOs occupied in **both** the d- and f-block species, allowing for this comparison to be made, but our results showed that upon excitation, there is a distinctively conversing trend in the d- and f-block species, where the *cis*- and *trans*-bond length ratios move closer to a value of 1, but by opposite means (for the d-block species, the *cis*-bonds stretch; for the f-block species the *trans*-bonds stretch).

5.3 Final Remarks and Further work

Based on the limitations in this project, our immediate suggestions for further work would be to find a way to analyse the $[WOX_5]^-$ complexes using a bond-orbital approach (as well as the $[MoOF_5]^-$ complex). As well considering the excited state analysis whilst implementing a solvation model, something that was not achieved in this project. In terms of expanding upon the theory and implications of this project, considering the ITI in species beyond the $[UOX_5]^-$ complexes would be a good approach, providing insights to the differences and similarities between ITI-exhibiting complexes, much like the work in this project comparing the TI-exhibiting $[MoOX_5]^-$ and $[WOX_5]^-$ species.

In summary, we show that in the ground state of ITI/TI-exhibiting $[MOX_5]^-$ complexes, the bond opposite (*trans-*) to a strong σ-donor, compared to the *cis*-bonds, is shorter with a greater degree of covalency in the f-block species, and longer with a lower degree of covalency in the d-block species. For both the d- and f-block, the difference in *cis*- and *trans*-bond lengths is greatest in the X = F complexes, and lowest in the X = Br complexes. Correspondingly, the M-F bonds have the greatest degree of overlap-driven covalency, and lowest degree of energy-driven and the M-Br bonds have the lowest degree of overlap-driven covalency, and greatest degree of energy-driven covalency.

In the excited states, we have successfully identified several occupied molecular orbitals exclusive to the f-block $[UOX_5]^-$ complexes, that upon excitation, yields a reversal of the ITI to a TI (whereby the *trans*-ligand bond lengths are then greater than the remaining *cis*-ligand bond lengths). But perhaps more significantly, we have identified a molecular orbital (with high d_{z^2} character) occupied in both d- and f-block species, that upon excitation, yields a decrease in the TI for the former species, and a decrease of the ITI (whereby it is switched to a TI) for the latter.

Chapter 6

Bibliography

1   B. J. Coe and S. J. Glenwright, *Coord. Chem. Rev.*, 2000, **203**, 5–80.

2   A. W. Adamson, in *Inorganic Chemistry*, 1963, vol. 2, p. 665.

3   I. Fryer-Kanssen and A. Kerridge, *Chem. Commun.*, 2018, **54**, 9761–9764.

4   A. J. Lewis, P. J. Carroll and E. J. Schelter, *J. Am. Chem. Soc.*, 2013, **135**, 13185–13192.

5   M. Gregson, E. Lu, D. P. Mills, F. Tuna, E. J. L. McInnes, C. Hennig, A. C. Scheinost, J. McMaster, W. Lewis, A. J. Blake, A. Kerridge and S. T. Liddle, *Nat. Commun.*, 2017, **8**, 1–11.

6   A. Kovács and R. J. M. Konings, *ChemPhysChem*, 2006, **7**, 455–462.

7   R. G. Denning, *Complexes, Clust. Cryst. Chem.*, 1992, **79**, 215–276.

8   E. O'Grady and N. Kaltsoyannis, *J. Chem. Soc. Dalt. Trans.*, 2002, 1233–1239.

9   A. J. Lewis, K. C. Mullane, E. Nakamaru-Ogiso, P. J. Carroll and E. J. Schelter, *Inorg. Chem.*, 2014, **53**, 6944–6953.

10   R. G. Denning, *J. Phys. Chem. A*, 2007, **111**, 4125–4143.

11   K. W. Bagnall, J. G. H. Du Preez, B. J. Gellatly and J. H. Holloway, *J. Chem. Soc. Dalt. Trans.*, 1975, 1963–1968.

12   K. Tatsumi and R. Hoffmann, *Inorg. Chem.*, 1980, **19**, 2656–2658.

13   W. R. Wadt, *J. Am. Chem. Soc.*, 1981, **103**, 6053–6057.

14   O. P. Lam, S. M. Franke, H. Nakai, F. W. Heinemann, W. Hieringer and K. Meyer, *Inorg. Chem.*, 2012, **51**, 6190–6199.

15   J. Chatt, L. A. Duncanson and L. M. Venanzi, *J. Chem. Soc.*, 1956, **0**, 2712–2725.

16   L. Carlton, M. A. Fernandes and E. Sitabule, *Proc. Natl. Acad. Sci.*, 2007, **104**, 6969–6973.

17   P. N. Kapoor and R. Kakkar, *J. Mol. Struct. THEOCHEM*, 2004, **679**, 149–156.

18   P. B. Hitchcock, B. Jacobson and A. Pidcock, *J. Chem. Soc. Dalt. Trans.*, 1977, **0**, 2043–2048.

19   W. R. Scheidt, *Inorg. Chem.*, 1973, **12**, 1758–1761.

20   F. R. Hartley, *Chem. Soc. Rev.*, 1973, **2**, 163–179.

21   B. D. M Adams, J. Chatt, J. Gerratt and A. D. Westland, *Russ. J. Inorg. Chem*, 1958, **26**, 5.

22   G. B. Kauffman, in *Encyclopedia of Inorganic and Bioinorganic Chemistry*, John Wiley & Sons, Ltd, Chichester, UK, 2011.

23   G. B. Kauffman, *Il'ya Il'ich Chernyaev (1893-1966) and the trans effect*, UTC, 2009, vol. 54.

24 A. A. Grinberg, G. A. Shagisultanova and M. I. Gel'fman, *Bull. Acad. Sci. USSR Div. Chem. Sci.*, 1963, **12**, 529–537.

25 R. F. See and D. Kozina, *J. Coord. Chem.*, 2013, **66**, 490–500.

26 T. G. Appleton, H. C. Clark and L. E. Manzer, *Coord. Chem. Rev.*, 1973, **10**, 335–422.

27 A. Pidcock, R. E. Richards and L. M. Venanzi, *J. Chem. Soc. A Inorganic, Phys. Theor.*, 1966, 1707–1710.

28 R. Mason and A. D. C. Towl, *J. Chem. Soc. A Inorganic, Phys. Theor. Chem.*, 1970, **0**, 1601–1613.

29 M. Stebler-Röthlisberger, A. Ludi, W. Hummel, H. B. Bürgi, P. A. Pittet and A. E. Merbach, *Inorg. Chem.*, 1988, **27**, 1358–1363.

30 K. A. Nolin, J. R. Krumper, M. D. Pluth, R. G. Bergman and F. D. Toste, *J. Am. Chem. Soc.*, 2007, **129**, 14684–14696.

31 R. E. P. Chandrasena, K. P. Vatsis, M. J. Coon, P. F. Hollenberg and M. Newcomb, *J. Am. Chem. Soc.*, 2004, **126**, 115–126.

32 J. J. Wilson and S. J. Lippard, *Chem. Rev.*, 2014, **114**, 4470.

33 J. D. Atwood, *Inorganic and organometallic reaction mechanisms*, VCH Publishers, 2nd edition., 1997.

34 H. S. La Pierre and K. Meyer, *Inorg. Chem.*, 2013, **52**, 529–539.

35 N. N. Greenwood and A. Earnshaw, *Chemistry of the Elements pt.2*, Butterworth-Heinemann, Oxford (Boston), 2nd edn., 1997.

36 A. Kerridge, *Chem. Commun.*, 2017, **53**, 6685–6695.

37 E. Lu, S. Sajjad, V. E. J. Berryman, A. J. Wooles, N. Kaltsoyannis and S. T. Liddle, *Nat. Commun.*, 2019, **10**, 634.

38 L. R. Morss, N. M. Edelstein and J. Fuger, *The chemistry of the actinide and transactinide elements. Volumes 1-6*, Springer, 2010.

39 N. Govind and W. A. de Jong, *Theor. Chem. Acc.*, 2014, **133**, 1–7.

40 Keith Kostecka, *Bull. Hist. Chem.*, 2008, **33**, 89–93.

41 A. Kerridge, *RSC Adv.*, 2014, **4**, 12078–12086.

42 K. N. Raymond and V. C. Pierre, *Bioconjug. Chem.*, 2005, **16**, 3–8.

43 WNA, Uranium Mining Overview - World Nuclear Association, http://www.world-nuclear.org/information-library/nuclear-fuel-cycle/mining-of-uranium/uranium-mining-overview.aspx, (accessed 10 July 2019).

44 International Atomic Energy Agency, *IAEA-TECDOC-1450 Thorium fuel cycle - Potential benefits and challenges*, 2005.

45 E. D. Davis, C. R. Gould and E. I. Sharapov, *Int. J. Mod. Phys. E*, 2014, **23**, 1430007.

46 R. J. de Meijer, V. F. Anisichkin and W. Van Westrenen, *Chem. Geol.*, 2013, **345**, 40–49.

47 B. Kosog, H. S. La Pierre, F. W. Heinemann, S. T. Liddle and K. Meyer, *J. Am. Chem. Soc.*, 2012, **134**, 5284–5289.

48   J. M. Bartleet, R. G. Denning and I. D. Morrison, *Mol. Phys.*, 1992, **75**, 601–612.

49   H. S. La Pierre, M. Rosenzweig, B. Kosog, C. Hauser, F. W. Heinemann, S. T. Liddle and K. Meyer, *Chem. Commun.*, 2015, **51**, 16671–16674.

50   S. Beer, O. B. Berryman, D. Ajami and J. Rebek, *Chem. Sci.*, 2010, **1**, 43–47.

51   A. C. Sather, O. B. Berryman and J. Rebek, *J. Am. Chem. Soc.*, 2010, **132**, 13572–13574.

52   T. M. Trnka and R. H. Grubbs, *Acc. Chem. Res.*, 2001, **34**, 18–29.

53   I. The Shodor Education Foundation, Overview of Computational Chemistry, http://www.shodor.org/chemviz/overview/ccbasics.html, (accessed 20 June 2019).

54   M. Born, *Nature*, 1927, **119**, 354–357.

55   C. J. Cramer, *Essentials of Computational Chemistry Theories and Models*, 2004, vol. 42.

56   B. S. Robert Mulliken, *Electronic Structures of Polyatomic Molecules and Valence. II. General Considerations*, vol. 41.

57   E. G. Lewars, *Computational chemistry: Introduction to the theory and applications of molecular and quantum mechanics: Third Edition 2016*, Springer, third., 2016.

58   P. Reinhardt and P. E. Hoggan, in *International Journal of Quantum Chemistry*, 2009, vol. 109, pp. 3191–3198.

59   E. Besalú and R. Carbó-Dorca, *J. Math. Chem.*, 2011, **49**, 1769–1784.

60   W. J. Hehre, R. F. Stewart and J. A. Pople, *J. Chem. Phys.*, 1969, **51**, 2657–2664.

61   TURBOMOLE V6.6 2014, a development of University of Karlsruhe and Forschungszentrum
Karlsruhe GmbH, 1989-2007, TURBOMOLE GmbH, since 2007; available from http://www.turbomole.com.

62   T. H. Dunning, *J. Chem. Phys*, 1989, **90**, 1007.

63   M. Jabłoński and M. Palusiak, *J. Phys. Chem. A*, 2010, **114**, 2240–2244.

64   S. Grimme, *J. Comput. Chem.*, 2004, **25**, 1463–1473.

65   A. D. Becke, *J. Chem. Phys.*, , DOI:10.1063/1.4869598.

66   P. H. and W. Kohn, *Phys. Rev.*, 1964, **136**, 864–871.

67   W. Kohn and L. J. Sham, *Phys. Rev. *, 1965, **140**, 1133–1138.

68   E. Fermi, *Rendiconti Lincei*, 1927, **6**, 602–607.

69   L. H. Thomas, *Cambridge Philos. Soc.*, 1927, **23**, 542–548.

70   F. Jensen, *Introduction to Computational Chemistry*, Wiley, second., 2014.

71   J. P. Perdew, *AIP Conf. Proc.*, 2001, **577**, 1–20.

72   J. P. Perdew, K. Burke and M. Ernzerhof, *Phys. Rev. Lett.*, 1996, **77**, 3865–3868.

73   A. D. Becke, *Phys. Rev. A*, 1988, **38**, 3098–3100.

74   R. Ahlrichs, M. Bär, M. Häser, H. Horn and C. Kölmel, *Chem. Phys. Lett.*, 1989, **162**,

165–169.

75   P. A. M. Dirac, *Math. Proc. Cambridge Philos. Soc.*, 1930, **26**, 376–385.

76   J. Toulouse and C. Adamo, *Chem. Phys. Lett.*, 2002, **362**, 72–78.

77   A. D. Becke, *J. Chem. Phys.*, 1998, **109**, 2092–2098.

78   J. P. Perdew, S. Kurth, A. Zupan and P. Blaha, *Phys. Rev. Lett.*, 1999, **82**, 2544–2547.

79   A. D. Becke, *J. Chem. Phys.*, 1993, **98**, 5648–5652.

80   C. Adamo and V. Barone, *J. Chem. Phys.*, 1999, **110**, 6158–6170.

81   A. D. Becke, *J. Chem. Phys.*, 1993, **98**, 1372–1377.

82   S. H. Vosko, L. Wilk and M. Nusair, *Can. J. Phys.*, 1980, **58**, 1200–1211.

83   P. J. Stephens, F. J. Devlin, C. F. Chabalowski and M. J. Frisch, *J. Phys. Chem.*, 1994, **98**, 11623–11627.

84   V. N. Staroverov, G. E. Scuseria, J. Tao and J. P. Perdew, *J. Chem. Phys.*, 2003, **119**, 12129–12137.

85   V. N. Staroverov, G. E. Scuseria, J. Tao and J. P. Perdew, *J. Chem. Phys.*, 2004, **121**, 11507.

86   J. P. Perdew, M. Ernzerhof and K. Burke, *J. Chem. Phys.*, 1996, **105**, 9982–9985.

87   K. Burke, *J. Chem. Phys.*, 2012, **136**, 150901.

88   E. A. C. Bushnell and J. W. Gauld, *J. Comput. Chem.*, 2013, **34**, 141–148.

89   M. Straka, M. Patzschke and P. Pyykkö, *Theor. Chem. Acc.*, 2003, **109**, 332–340.

90   N. I. Giricheva, M. S. Fedorov, S. N. Ivanov and G. V. Girichev, *J. Mol. Struct.*, 2015, **1085**, 191–197.

91   S. Grimme, J. Antony, S. Ehrlich and H. Krieg, *J. Chem. Phys.*, 2010, **132**, 130901.

92   R. E. Skyner, J. L. McDonagh, C. R. Groom, T. van Mourik and J. B. O. Mitchell, *Phys. Chem. Chem. Phys.*, 2015, **17**, 6174–6191.

93   J. Tomasi, B. Mennucci and R. Cammi, *Chem. Rev.*, 2005, **105**, 2999–3094.

94   J. P. W. Wellington, A. Kerridge and N. Kaltsoyannis, *Polyhedron*, 2016, **116**, 57–63.

95   O. Treutler and R. Ahlrichs, *J. Chem. Phys.*, 1995, **102**, 346–354.

96   F. Furche and R. Ahlrichs, *J. Chem. Phys.*, 2002, **117**, 7433–7447.

97   D. Rappoport and F. Furche, *J. Chem. Phys.*, 2005, **122**, 064105.

98   J. Tao, J. P. Perdew, V. N. Staroverov and G. E. Scuseria, *Phys. Rev. Lett.*, 2003, **91**, 146401.

99   R. A. Kendall, T. H. Dunning and R. J. Harrison, *J. Chem. Phys.*, 1992, **96**, 6796–6806.

100   D. E. Woon and T. H. Dunning, *J. Chem. Phys.*, 1993, **98**, 1358–1371.

101   A. K. Wilson, D. E. Woon, K. A. Peterson and T. H. Dunning, *J. Chem. Phys.*, 1999, **110**, 7667–7676.

102   A. Schäfer, H. Horn and R. Ahlrichs, *J. Chem. Phys.*, 1992, **97**, 2571–2577.

103   A. Schäfer, C. Huber and R. Ahlrichs, *J. Chem. Phys.*, 1994, **100**, 5829–5835.

104   X. Cao, M. Dolg and H. Stoll, *J. Chem. Phys.*, 2003, **118**, 487–496.

105   W. Küchle, M. Dolg, H. Stoll and H. Preuß, *J. Chem. Phys.*, 1994, **100**, 7535–7542.

106   K. Eichkorn, F. Weigend, O. Treutler and R. Ahlrichs, *Theor. Chem. Acc.*, 1997, **97**, 119–124.

107   D. Andrae, U. Häußermann, M. Dolg, H. Stoll and H. Preuß, *Theor. Chim. Acta*, 1990, **77**, 123–141.

108   F. Weigend and R. Ahlrichs, *Phys. Chem. Chem. Phys.*, 2005, **7**, 3297–3305.

109   Glendening, J. K. et al. NBO 6.0 (Theoretical Chemistry Institute, University of Wisconsin, Madison, 2013).

110   Richard. F. Bader, *Atoms in Molecules: A Quantum Theory*, Oxford University Press, Oxford, 1990.

111   AIMAII (version 19.02.13), Todd A. Keith, TK Gristmill Software, Overland Park KS, USA, 2019 (aim.tkgristmill.com)

112   T. Lu and F. Chen, *J. Comput. Chem.*, 2012, **33**, 580–592.

113   A. D. Becke and K. E. Edgecombe, *J. Chem. Phys.*, 1990, **92**, 5397–5403.

114   A. Savin, A. D. Becke, J. Flad, R. Nesper, H. Preuss and H. G. von Schnering, *Angew. Chemie Int. Ed. English*, 1991, **30**, 409–412.

115   M. A. Spackman and P. G. Byrom, *Chem. Phys. Lett.*, 1997, **267**, 215–220.

116   A. E. Reed, R. B. Weinstock and F. Weinhold, *J. Chem. Phys.*, 1985, **83**, 735–746.

117   J. Tanti, M. Lincoln and A. Kerridge, *Inorganics*, 2018, **6**, 88.

118   A. C. Behrle, A. J. Myers, A. Kerridge and J. R. Walensky, *Inorg. Chem.*, 2018, **57**, 10518–10524.

119   R. E. Wilson, S. De Sio and V. Vallet, *Nat. Commun.*, 2018, **9**, 2–10.

120   P. L. A. Popelier, in *The Chemical Bond: Fundamental Aspects of Chemical Bonding*, 2014, pp 271–308.

121   R. F. W. Bader and C. F. Matta, *J. Phys. Chem. A*, 2004, **108**, 8385–8394.

122   G. R. Runtz, R. F. W. Bader and R. R. Messer, *Can. J. Chem.*, 1977, **55**, 3040–3045.

123   C. F. Matta and R. J. Boyd, *The Quantum Theory of Atoms in Molecules: From Solid State to DNA and Drug Design*, 2007.

124   R. Hilal, S. G. Aziz, A. O. Alyoubi and S. Elroby, *Procedia Comput. Sci.*, 2015, **51**, 1872–1877.

125   V. E. J. Berryman, Z. J. Whalley, J. J. Shephard, T. Ochiai, A. N. Price, P. L. Arnold, S. Parsons and N. Kaltsoyannis, *Dalt. Trans.*, 2019, **48**, 2939–2947.

126   W. W. Lukens, N. M. Edelstein, N. Magnani, T. W. Hayton, S. Fortier and L. A. Seaman, *J. Am. Chem. Soc.* 2013, **135**, 10742–10754.

127   J. R. Walensky, R. L. Martin, J. W. Ziller and W. J. Evans, *Inorg. Chem.*, 2010, **49**,

10007–10012.

128   R. F. W. Bader, M. T. Carroll, J. R. Cheeseman and C. Chang, *J. Am. Chem. Soc.*, 1987, **109**, 7968–7979.

129   C. Barnes, *J. Chem. Educ.*, 2009, **80**, 747.

130   M. Tamm, T. Bannenberg, V. Urban, T. Pape and O. Kataeva, *Zeitschrift für Naturforsch. B*, 2015, **61**, 1189–1197.

131   N. A. Ovchinnikova, A. E. Sinyakov, V. S. Sergienko and G. G. Aleksandrov, *Crystallogr. Reports*, 2003, **48**, 602–605.

132   C. A. Dodds, M. D. Spicer and T. Tuttle, *Organometallics*, 2011, **30**, 6262–6269.

133   M. Bortoluzzi, F. Marchetti, M. G. Murrali, G. Pampaloni and S. Zacchini, *Dalt. Trans.*, 2015, **44**, 8729–8738.

134   W. Levason, F. M. Monzittu, G. Reid and W. Zhang, *Chem. Commun.*, 2018, **54**, 11681–11684.

135   F. R. Cordell and J. E. Boggs, *J. Mol. Struct. THEOCHEM*, 1988, **164**, 175–182.

136   M. Bortoluzzi, F. Guarra, F. Marchetti, G. Pampaloni and S. Zacchini, *Polyhedron*, 2015, **99**, 141–146.

137   A. Bondi, *J. Phys. Chem.*, 1964, **68**, 441–451.

138   H. Chermette, K. Rachedi and F. Volatron, *J. Mol. Struct. THEOCHEM*, 2006, **762**, 109–121.

139   R. D. Shannon, *Acta Crystallogr. Sect. A*, 1976, **32**, 751–767.

140   G. V. Gibbs, F. C. Hill, M. B. Boisen and R. T. Downs, *Phys. Chem. Miner.*, 1998, **25**, 585–590.

141   L. Zhang, F. Ying, W. Wu, P. C. Hiberty and S. Shaik, *Chem. - A Eur. J.*, 2009, **15**, 2979–2989.

142   C. G. Gianopoulos, V. V. Zhurov, S. G. Minasian, E. R. Batista, C. Jelsch and A. A. Pinkerton, *Inorg. Chem.*, 2017, **56**, 1775–1778.

143   R. G. Pearson, *J. Am. Chem. Soc.*, 1963, **85**, 3533–3539.

144   D. F. Eaton, *International union of pure and applied chemistry organic chemistry division commission on photochemistry. Reference materials for fluorescence measurement*, 1988, vol. 2.

145   A. D. McNaught and A. Wilkinson, *IUPAC compendium of chemical terminology*, Blackwell Scientific Publications, Oxford, 2nd ed., 2013, vol. 40.

146   R. G. Parr and R. G. Pearson, *Absolute Hardness: Companion Parameter to Absolute Electronegativity*, 1983, vol. 105.

147   B. Bankiewicz, P. Matczak and M. Palusiak, *J. Phys. Chem. A*, 2012, **116**, 452–459.

148   Maurice L. Huggins, 1953, **75**, 4126–4133.

149   R. C. Bochicchio, L. Lain and A. Torre, *Chem. Phys. Lett.*, 2003, **374**, 567–571.

150   J. G. Ángyán, M. Loos and I. Mayer, *Covalent bond orders and atomic valence indices in the topological theory of atoms in molecules*, 1994, vol. 98.

151   X. Fradera, M. A. Austen and R. F. W. Bader, *J. Phys. Chem. A*, 1999, **103**, 304–314.

152   D. Hugas, L. Guillaumes, M. Duran and S. Simon, *Comput. Theor. Chem.*, 2012, **998**, 113–119.

153   C. van Wüllen, *J. Comput. Chem.*, 2011, **32**, 1195–1201.

154   E. Runge and E. K. U. Gross, *Phys. Rev. Lett.*, 1984, **52**, 997–1000.

Chapter 7

Supplementary Data

Table 7.1. NBO data for the f-block $[UOX_5]^-$ complexes, showing each species' contribution % to the bond , and of that contribution, the percentages of constituent bonding orbitals (s, p, d, and f) that make it up. The data in **figure 3.7** is obtained by multiplying the contribution percentages by the bonding orbital percentages

	Species in the U-X bond	Contribution to the bond / %	s-orbital	p-orbital	d-orbital	f-orbital
[UOF₅]⁻	U-F*cis* (F)	89.0%	34.3%	65.6%	0.1%	0.0%
	U-F*cis* (U)	11.0%	18.5%	0.1%	32.1%	49.1%
	U-F*trans* (F)	87.7%	30.9%	69.0%	0.1%	0.0%
	U-F*trans* (U)	12.3%	18.2%	0.1%	43.1%	38.3%
[UOCl₅]⁻	U-Cl*cis* (Cl)	81.1%	30.3%	69.5%	0.2%	0.0%
	U-Cl*cis* (U)	19.0%	18.3%	0.1%	33.3%	48.3%
	U-Cl*trans* (Cl)	78.9%	26.1%	73.6%	0.3%	0.0%
	U-Cl*trans* (U)	21.1%	20.9%	0.3%	43.7%	35.0%
[UOBr₅]⁻	U-Br *cis* (Br)	78.8%	25.3%	74.4%	0.3%	0.0%
	U-Br *cis* (U)	21.2%	18.3%	0.2%	33.4%	48.1%
	U-Br *trans* (F)	76.4%	21.4%	78.3%	0.3%	0.0%
	U-Br *trans* (U)	23.6%	21.4%	0.5%	43.5%	34.6%

Table 7.12. NBO data for the d-block $[MoOX_5]^-$ complexes (X = Cl, and Br), showing each species' contribution % to the bond, and of that contribution, the percentages of constituent bonding orbitals (s, p, d, and f) that make it up. The data in **figure 3.8** is obtained by multiplying the contribution percentages by the bonding orbital percentages

		Contribution to the bond / %	s-orbital	p-orbital	d-orbital	f-orbital
[MoOCl₅]⁻	Mo-Cl *cis* (Cl)	73.8%	19.1%	80.3%	0.5%	0.1%
	Mo-Cl *cis* (U)	26.2%	33.0%	0.4%	66.4%	0.1%
	Mo-Cl *trans* (Cl)	83.1%	24.9%	74.7%	0.3%	0.0%
	Mo-Cl *trans* (U)	16.9%	31.7%	0.8%	67.3%	0.2%
[MoOBr₅]⁻	Mo-Br *cis* (Br)	82.9%	13.8%	85.7%	0.4%	0.1%
	Mo-Br *cis* (U)	17.1%	14.6%	42.3%	39.1%	4.1%
	Mo-Br *trans* (Br)	82.1%	19.3%	80.4%	0.3%	0.0%
	Mo-Br *trans* (U)	17.9%	33.3%	1.4%	65.3%	0.1%

Table 7.3. Bond length data in picometers (pm) for the $[MOX_5]^-$ complexes (M = U, Mo, W, and X = F, Cl, Br) at the excited states $\sum_u$, $\sum_u*$, and $\sum_g$, of which are defined in **section 4.3**. A plot of this data is provided in the main text (**figures 4.6** and **4.13**, **section 4.2** and **4.3** respectively)

Excited state geometry		$D_{U\text{-}X}$ (*cis*) / pm	$D_{U\text{-}X}$ (*trans*) / pm	$D_{U\text{-}O}$ / pm	Influence magnitude
$\sum_u$	$[UOF_5]^-$	221.03	205.02	185.21	0.928
	$[UOCl_5]^-$	264.50	269.83	179.89	1.020
	$[UOBr_5]^-$	280.60	285.1	179.02	1.016
$\sum_u*$	$[UOF_5]^-$	224.36	220.21	187.41	0.982
	$[UOCl_5]^-$	269.77	265.55	185.30	0.984
	$[UOBr_5]^-$	281.80	283.83	187.86	1.007
$\sum_g$	$[UOF_5]^-$	218.42	223.20	184.38	1.022
	$[UOCl_5]^-$	261.97	266.5	190.05	1.017
	$[UOBr_5]^-$	277.03	282.38	192.95	1.019
	$[MoOF_5]^-$	192.78	195.38	181.64	1.013
	$[MoOCl_5]^-$	241.54	251.11	181.35	1.040
	$[MoOBr_5]^-$	257.05	269.02	185.00	1.047
	$[WOF_5]^-$	202.12	201.06	174.09	0.995
	$[WOCl_5]^-$	244.88	249.40	179.20	1.018
	$[WOBr_5]^-$	258.05	269.81	183.89	1.046